Extracellular Spaces and Cardiac Conduction

Tristan Bryan Raisch

Dissertation submitted to the faculty of the Virginia Polytechnic Institute and State University in partial fulfillment of the requirements for the degree of

Doctor of Philosophy
In
Translational Biology, Medicine and Health

Dr. Steven Poelzing
Dr. Rob Gourdie
Dr. Soufian Almahameed
Dr. James Smyth

February 1st, 2019
Roanoke, VA

Keywords: Cardiac, Perinexus, Ephaptic Coupling, Atrial Fibrillation, Cardiac Conduction

ABSTRACT

Despite decades of research and thousands of studies on cardiac electrophysiology, cardiovascular disease remains among the leading causes of death in the United States today. Despite substantially beneficial advances, we have largely shifted cardiovascular disease from an acute to a chronic issue. It is therefore clear that our current understanding of the heart's functions remain inadequate and we must search for untapped therapeutic approaches to eliminate these deadly and costly ailments once and for all. This thesis will focus on the electrophysiology of the heart, specifically the mechanisms of cell-to-cell conduction. Canonically, the understood mechanism of cardiac conduction is through gap junctions (GJ) following a cable-like conduction model. While both experimentally and mathematically, this understanding of conduction has explained cardiac electrical behavior, it is also incomplete, as evidenced by recent conflicting modeling and experimental data. The overall goal of this thesis is to explore a structure modulating an ephaptic, or electric field, cellular coupling mechanism: the GJ-adjacent perinexus, with three specific aims. First, I identified the perinexus – a recently-established structure in rodent myocardium – in human atrial tissue. I also observed a significant tendency for open-heart surgery patients with pre-operative atrial fibrillation to have wider perinexi, indicating a possibly targetable mechanism of atrial fibrillation, one of the costliest, and most poorly-understood cardiac diseases. Next, I developed a high-throughput, high-resolution method for quantifying the perinexus. Finally, I sought to reconcile a major controversy in the field: whether cardiac edema could either be beneficial or harmful to cardiac conduction. Using a Langendorff perfusion model, I added osmotic agents of various sizes to guinea pig hearts and measured electrical and structural parameters. My findings suggest that while cardiac conduction is multifaceted and influenced by several parameters, the strongest correlation is an inverse relationship between conduction velocity and the width of the perinexus. This study is the first to osmotically expand *and* narrow the perinexus and show an inverse correlation with conduction. Importantly, my conduction data cannot be explained by factors consistent with a cable-like conduction mechanism, indicating once again that the perinexus could be a therapeutic target for a myriad of cardiac conduction diseases.

GENERAL AUDIENCE ABSTRACT

The ways by which cells in the heart communicate have been studied extensively and are thought to be well-understood. However, despite decades of research, cardiovascular disease is a major problem in the developed world today and we remain unable to develop treatments to truly cure many major cardiac diseases. Because of this lack of clinical success in preventing or treating conditions such as atrial fibrillation, Brugada syndrome and sudden cardiac death, all of which are associated with disruptions in the heart's electrical communication systems, I have sought to better understand the ways by which cellular communication is achieved. Currently, we think of cardiac tissue to propagate electrical signals as if it was a series of cables, just like the electrical wires over our streets and in our homes. However, we have seen experimental evidence, along with computer simulations, that supports the idea of a second mechanism of cellular electrical conduction. This second mechanism is called ephaptic, or electric field, coupling and relies on changes in charges inside and outside the cell to trigger the action potential – the electrical signal which tells the cell to contract. In order for ephaptic coupling to occur, two main conditions must be met. First, there must be a suitably-sized cleft, or ephapse, between adjacent cells. Models have estimated this space to be between 10-100 nm wide. Second, there must be a large concentration of sodium channels, as sodium ions are primarily used to set off the action potential. The region in which I am most interested is the cardiac perinexus, which is the space immediately adjacent to plaques of connexin proteins which link adjacent cells. The perinexus is both of an appropriate size (we've measured it between 10 and 25 nm on average) and rich in sodium channels, making it an ideal candidate to be a cardiac ephapse. In recent years, our lab has shown experimentally that expanding this space can disrupt cardiac conduction and my first study showed that clinically, patients with chronic atrial fibrillation (a-fib) prior to open-heart surgery have wider perinexi than patients without chronic a-fib. No one, however, has been able to demonstrate that narrowing the perinexus would be therapeutic by making it easier for cells to communicate via this ephaptic mechanism. Knowing I would need a better method for measuring the width of huge numbers of perinexi,

I then developed a faster, more precise measurement program. Finally, I perfused several osmotic agents – substances which would theoretically draw fluid into or out of various compartments of cardiac tissue – into guinea pig hearts and observed changes to both their electrical behavior and tissue structure. Using my new perinexal measurement program, I found that changing the perinexus was the only factor that could explain the conduction changes I observed with each osmotic agent and that parameters associated with cable theory, such as gap junctional protein expression or interstitial resistance, could not explain conduction changes. Therefore, I have indicated, along with my clinical study, that the cardiac perinexus could be a therapeutic target for preventing, managing, or possibly even curing cardiac conduction diseases.

ACKNOWLEDGEMENTS

First and foremost, I would like to thank my advisor, Dr. Steven Poelzing, who convinced me this whole PhD thing was a good idea. I don't know how I could have gotten through graduate school with a bad advisor, but I am darn grateful I had an excellent one. He has a unique ability to, in every instance when I was sure nothing would work, have me leaving his office 20 minutes later brimming with confidence and new ideas. Thank you for your tireless work to always push me further and to be better than I knew I could.

I would next like to thank all of the members of my dissertation committee for their help, guidance suggestions and support. Their feedback, questions and impromptu discussions made this work far better than it could have been otherwise and made me a far better scientist in the process. Drs. Rob Gourdie, James Smyth and Soufian Almahameed have been instrumental in developing a fundable F31 and then executing a PhD-level project. I hope the following pages do them proud.

To all the past and present members of the Poelzing laboratory, I cannot thank you enough. Dr. Greg Hoeker, our postdoc, has provided an excellent example I aim to follow as I move on to my own postdoctoral work. He has always been willing to spare a moment to mentor the junior trainees, and the lab was never cleaner than after receiving a talking-to from Greg. Ryan King, Sarah Frazier and Katrina Colucci make me confident the lab is in good hands, as I both watched their growth as scientists and appreciated their insights and feedback as I progressed in my own work. Finally, a huge thank you to Drs. Sai Veeraraghavan, Sharon George, Amara Greer-Short and Michael Entz, who trained and mentored me in my first years in the lab, without whom none of the below work would have been possible.

Many thanks to Kathy Lowe, Dr. Sarah Barrett, and our lab manager, Chandra Baker, for their invaluable help with TEM tissue processing, H&E staining and Western blots, respectively. Thanks also to Dr. Chris Winkler for additional assistance with TEM imaging.

I would next like to thank all the content creators, whose videos, streams and podcasts made the hours of data analysis fly by, specifically Extra Credits, Resonance22, Scott Manley and Preach Gaming.

Next, I cannot thank enough the family and friends who have been so supportive and encouraging over the past four and a half years. My parents gave me the freedom and confidence to move across the country to pursue my undergraduate studies and have never wavered in their love or support as I've stayed 2500 miles away for the past decade. A special thank you to Dan, who always had a couch to crash on, a beer to share and a story to tell whenever I was in town. You all kept me motivated to see this thing through.

Finally, a massive thanks to my amazing wife, Caila. She has put her own dreams on hold and put up with more stress and inconvenience than I could detail so I could pursue my passion. She, and our pup, helped me see the light at the end of the tunnel and believe it wasn't a train. She is my best friend, my support and the one I'm honored to go through this crazy life with. I am the person I am today, nearly unrecognizable from who I was, because of you. Thank you, Sweetheart.

TABLE OF CONTENTS

LIST OF FIGURES

LIST OF TABLES

Table Page

LIST OF ABBREVIATIONS AND ACRONYMS

2D	2-Dimensional
3D	3-Dimensional
ACV	Alternating Current Voltage
AF	Atrial Fibrillation
APD	Action Potential Dispersion
CRMH	Carilion Roanoke Memorial Hospital
CV	Conduction Velocity
CVL	Longitudinal Conduction Velocity
CVT	Transverse Conduction Velocity
Cx43	Connexin 43
DCV	Direct Current Voltage
E_{ion}	Ionic Reversal Potential
GJ	Gap junction
GUI	Graphical User Interface
H&E	Hematoxylin and Eosin
Hz	Hertz
ID	Intercalated Disc
kDa	kilodalton
LAA	Left Atrial Appendage
LAD	Left Anterior Descending coronary artery
LV	Left Ventricle
MDa	megadalton
mMol/L	milimole per Liter
MRI	Magnetic Resonance Imaging

Nm	Nanometer
OCT	Optimal Cutting Temperature medium
Paraformaldehyde	PFA
PBS	Phosphate Buffered Saline
RAA	Right Atrial Appendage
RV	Right Ventricle
S368	Serine 368
SCN1B	Cardiac sodium channel β1 subunit
SR	Sarcoplasmic Reticulum
TEM	Transmission Electron Microscopy
V_m	Membrane Potential
$\dot{V}_{max}$	Maximal Rate of Action Potential Rise
VIS	Interstitial Volume
VTCRI	Virginia Tech Carilion Research Institute
Wp	Perinexal Width
μm	Micrometer
Ω	Ohm

CHAPTER 1: THE STRUCTURE AND FUNCTION OF THE CARDIAC PERINEXUS

OVERVIEW OF CARDIAC FUNCTION

The heart is one of the most critical organs in the body, responsible for pumping blood to distribute oxygen and nutrients to, and remove waste from, other body systems [1]. In order to pump effectively as a whole, the heart needs each of its muscle cells, called cardiomyocytes [2], to contract in a synchronized manner and relax, dozens of times per minute for decades on end [3]. This synchronized contraction of millions of cardiomyocytes is achieved using electrical signals. As each cell activates, it transmits the signal downstream to the next cell and the next and so on. The purpose of this study is to understand the intricacies of the heart's electrical system and the following chapters will explore mechanisms by which that system can be disrupted in disease and treated clinically. First, we begin with the basic structure of the cardiomyocyte and how it functions.

Like all cells in the human body, the cardiomyocyte is enveloped by a double-layered cell membrane [4]. The proteins embedded in this membrane are critical to the function of the cell, as they function as pores or gates to allow various particles to enter or exit the cell. Some of the critical ion channels involved in cardiac function are sodium, calcium and potassium channels, each named for the ion they allow across the membrane. These ion channels can open or close based on the voltage across the cell membrane, called the membrane potential, or due to the binding of specific ligands to the channel protein [5-7]. Just inside the membrane is the sarcoplasmic reticulum (SR), essentially a calcium-filled pouch, which releases calcium onto myofilament structures, causing them to contract [8-12]. The method by which each cell is signaled to facilitate calcium release from the SR and contract is the action potential: an electrical signal that, through the flow of certain ions across the membrane, causes rapid depolarization of the cell membrane and subsequently repolarizes the membrane to prepare for the next cycle [13-15]. The changes in electrical potentials inside and outside the cell are simultaneously used to propagate the signal to subsequent cells, a vital process known as cardiac conduction [16-19]. Using this method, the heart is capable of achieving synchronized contraction of its cells to produce consistent, efficient blood pumping over decades of normal life.

Problems can arise when this cycle of depolarization-contraction-repolarization is disrupted. Such disruptions to the normal rhythm of cardiac conduction are called arrhythmias [20, 21]. While many arrhythmias are harmless –a typical adult can experience them as often as once per minute [22] – if they are allowed to continuously interfere with normal function they can cause severe health issues, even leading to death . The healthy heart can "reset" itself back to a normal rhythm without much difficulty because each cell experiences a refractory period after firing an action potential after which it cannot be excited for a period of time [23-27]. When an arrhythmogenic signal, originating somewhere other than the heart's normal conduction system, encounters a region of unexcitable tissue, the arrhythmia terminates harmlessly. When conduction is either slow or disorganized, however, an arrhythmogenic substrate is created in which arrhythmias can propagate and continue [28-30]. Such a phenomenon can present itself as conduction diseases including Brugada syndrome, long-QT syndrome, atrial fibrillation or ventricular fibrillation and sudden cardiac death [6, 24, 31-42]. Sudden cardiac arrest is responsible for over 350,000 deaths in the United States each year [43] and atrial fibrillation alone is responsible for approximately 130,000 annual deaths, due mostly to stroke, and roughly $6 billion in additional medical costs [43, 44]. These immense costs indicate an area of major need within the current healthcare system. The mechanisms of cardiac conduction are of critical importance to understanding how to prevent and treat costly and deadly arrhythmic diseases. Conduction is understood to occur primarily at the lateral ends of each cardiomyocyte, in a region known as the intercalated disc (ID) [45-50]. The structure of this junctional region is the focus of this dissertation and as such, it is important to understand the ID's physical composition, protein makeup, and possible role in cell-to-cell communication.

THE CARDIAC INTERCALATED DISC

The ID is a complex coupling region mechanically and electrically coupling adjacent cardiomyocytes. This region is composed of connexin gap junction (GJ) plaques and their adjacent perinexus, both of which will be discussed in detail below, as well as desmosomes and adherens junctions [47, 51-58] (See Rhett, 2013,

Figure 2). It is at this interface that the majority of electrical and mechanical coupling is thought to occur, potentially by multiple mechanisms.

THE CONNEXIN GAP JUNCTION

The basic unit of the gap junction plaque is the connexin protein [59-63]. These proteins form hexameric hemichannel pores, called connexons, which are trafficked to the cell membrane where they dock with connexons on the opposing cell membrane, forming a gap junction and allowing small particles to pass from cell to cell [64-66]. These gap junctions are arranged in plaques along the edge of opposing cardiomyocytes, electrically and mechanically linking the cells [67]. The structure and function of GJ proteins have been extensively reviewed [68-70], and the consensus is straightforward: in health and disease, connexins play a critical role in the cardiovascular system. Exactly what role connexins play, however, is a matter of some debate, whether that be primarily as a conductive pore protein or as a structural component which facilitates localization and assembly of other conductive structures such as sodium or potassium channels [71, 72]. The structure of connexin proteins themselves is made even more complex due to the protein's numerous isoforms. Several connexin isoforms – 21 in humans [73] – have been described, each with their own functional properties and named for their theoretical molecular size [73-78]. Three particular isoforms, Cx40, Cx43, and Cx45, are expressed in cardiomyocytes, while Cx37, Cx46, and Cx50 are present in other cardiac cell types, including the conductive His-Purkinje system [79-81]. The conductivity and regional expression of each of these connexin isomers appear to be critical factors in the precise timing of cardiac function as the heart's atria and then ventricles must activate sequentially in order to efficiently pump blood to the lungs and then out to the body. Such differences in connexin parameters allow a single signal to propagate from the atria to the sinoatrial node, the His-Purkinje system, and through the ventricles, triggering the sequential contraction of each region of the heart [82] and efficient pumping of blood. For our purposes, we will focus on the most abundantly-expressed myocyte isoform, Cx43. In addition to the structure and gating of the connexin pore itself, which can be impacted by parameters such as extracellular calcium [83] or pH [84], another process which can affect connexin conductivity, and therefore potentially modulate conduction velocity (CV), is phosphorylation [85]. Cx43 can be

phosphorylated by several kinases at a minimum of 19 different serine or tyrosine sites, which can affect assembly, gating, size or disassembly properties of the connexin [86]. One serine in particular, serine 368 (S368) has been associated with phosphorylation-induced decrease of connexin conductivity, specifically with ischemic injury [87, 88]. It is this site that will be utilized in a later chapter to assess potential ischemic injury in a whole-heart study.

THE CARDIAC PERINEXUS

At the point where the gap junction plaque terminates and the membranes of adjacent cells diverge from each other is the perinexus, a recently-defined nanodomain of particular electrophysiological interest [53, 89]. The perinexus proceeds approximately 200nm from the edge of the gap junction plaque, parallel to the cell membranes into the intercalated disc, and may vary in width based on disease state or extracellular ionic concentration. Beyond the perinexus, the rest of the intercalated disc is comprised of desmosomes and adherens junctions, which also serve as mechanical junctions between cells. With this understanding of the gap junction and perinexal regions of the ID, we can begin to explore the electrical principles which theoretically drive cardiac conduction.

THEORETICAL MECHANISMS OF CARDIAC CONDUCTION – CABLE THEORY

The canonical mechanism of cardiac conduction follows cable theory, wherein an electric signal is transferred via low-resistance gap junctions from the cytosol of one cell to another [90-92], while the extracellular space acts as a return path for the electric current, closing the circuit. Through decades of research, our understanding of this mechanism has evolved to what is commonly used today: the bidomain model [93-95]. As its name suggests, this model splits cardiac tissue into two primary domains: intercellular and extracellular, where the cell membrane is modeled as a variable resistor and capacitor in parallel. Utilizing Ohm's law, the model describes current densities within the two domains and how those current densities are transmitted extracellularly, intracellularly and intercellularly (cell-to-cell). The extracellular space in this case acts as a low-resistance return pathway which closes the intra- and inter-cell circuit. By inputting appropriate parameters, namely tissue capacitance, GJ resistance and tissue geometry,

mathematical models of tissue-level cardiac conduction can be generated and used to describe conduction under a myriad of conditions and disease states. This model has been elegantly demonstrated experimentally, in particular by Dr. Cole *et al* [96], who described longitudinal propagation data which fit an accepted cable model of conduction. First, they used the GJ uncoupler octanol to increase intercellular resistance in guinea pig papillary muscle and observed decreased CV. Additionally, they noted changes to the maximal rate of rise of the action potential ($\dot{V}_{max}$), which can be considered an indirect measure of membrane sodium currents. Interestingly, a biphasic relationship with $\dot{V}_{max}$, as described in their study, is inconsistent with a continuous cable model. In the same paper, they modified the Heppner-Plonsey core-conductor model [97] to simulate effects of removing GJs from the IDs between cardiomyocytes in a strand. Their experimental data were consistent with their modeling results: removal of GJ, or GJ uncoupling, slowed conduction in a manner consistent with a discontinuous cable model. In other words, instead of the rate of conduction remaining constant as current passes from cell to cell, conduction can be thought of as making temporal stops at cellular junctions. This conduction behavior is not unlike the salutatory conduction observed in myelinated neurons [98]. It is important to note that these experiments were conducted in papillary muscle, which is cable-like in its shape and sarcolemma "sheathing" [8], which could potentially provide electrical insulation that would be responsible for producing data which so closely fit cable theory models. Still, the papillary muscle model is not alone in describing slowed conduction with removal of GJs, as Dr. Rohr *et al* [99] found similar conduction slowing in rat ventricular myocyte strands with pharmacological GJ uncoupling.

Despite its utility in describing cardiac conduction, questions remain about the model's applicability to 3-dimensional space and conflicting predictions of experimental results. A key example of the breakdown of the real-life applicability of cable theory lies in a controversy over the removal of connexin proteins. A mouse expressing only half of its connexins ($Cx43^{+/-}$), and therefore in theory half of its conduction-facilitating GJ, in whole-heart experiments has presented both slowed cardiac CV [100] and no difference from its normal-connexin littermates [101]. Dr. Beauchamp *et al* found similarly perplexing results, as they

observed conduction between complete Cx43 knockout ($Cx43^{-/-}$) cells despite a decrease of 96% in intercellular conductance [102]. Since the drastic modulation of a critical parameter of GJ coupling results in such inconsistent conduction results, there must be a secondary conduction mechanism to preserve conduction in the event of impaired GJ coupling.

INTERSTITIAL SPACE AND CONDUCTION

Additionally, there is controversy about the role of the extracellular space in cardiac conduction. This space is filled with highly-conductive fluid [103, 104] and theoretically, collapsing this micro-scale region should increase the resistance of the circuit's return pathway [105] and decrease cardiac CV. Indeed, in rabbit papillary muscle, Drs. Fleischhauer, Lehmann, and Kléber report a direct relationship between interstitial volume and conduction [106], with no appreciable change to GJ conductance. They modulated interstitial volume through changes in colloid osmotic pressure associated with different levels of dextran 70 kDa. When beginning with 40g/L of dextran and washing in the same solution with only 10g/L of dextran, they observed a substantial increase in muscle diameter correlating with a reduction in extracellular longitudinal resistance. Simultaneously, intracellular resistance remained unchanged. This change in fiber diameter and extracellular resistance reduction was associated with a significant increase in longitudinal CV. When fiber diameter was returned to baseline through the wash-in of more highly-concentrated dextran, conduction was likewise reduced as extracellular resistance increased. It is again worth noting that these experiments were performed in the highly cable-like papillary muscle and their interpretations may not account for the 3D structure and "unsheathed" electrical nature of myocardial tissue. In a later experiment, Dr. Veeraraghavan *et al*, in Langendorff-perfused guinea pig hearts demonstrated an inverse relationship between interstitial volume and CV [107], in direct contrast with the results described by Fleischhauer and Kléber. In this study, they washed in either mannitol or albumin while optically mapping each heart. From a cable-like conduction paradigm of cardiac conduction, the results were perplexing. Mannitol expanded interstitial volume (VIS) and was associated with decreased transverse CV, with no significant change in longitudinal conduction. Albumin collapsed the interstitial space, presenting significantly smaller VIS, and increased conduction, also preferentially in the transverse direction. These two studies, showing the

opposite conduction response to similar changes in tissue structure (expansion or collapse of the extracellular space), suggest that the relationship between conduction and modulation of the extracellular space may not strictly adhere to cable theory.

Experimental inconsistencies in the relationship between gap junctions and cardiac conduction, in addition to that of interstitial space and conduction, raise a compelling question: What is the cause of these seemingly contradictory results? The most likely explanation is that either uncharacterized experimental differences underlie the controversies or, as I hypothesize, there exists an alternative mechanism of cell-to-cell communication that is not well-described by cable theory.

THEORETICAL MECHANISMS OF CARDIAC CONDUCTION – EPHAPTIC THEORY

Such a potential secondary mechanism of cardiac conduction, termed ephaptic coupling, has been proposed which describes changes in inter- and extra-cellular potentials to transmit electrical signals without the direct transfer of charge from cell-to-cell [108]. Through this mechanism, cells communicate through changes in extracellular charges which lead to the activation of membrane-bound ion channels. When an upstream cell activates, it draws sodium inside its membrane, decreasing the total extracellular charge in the space between that cell and its immediate downstream neighbor. This neighboring cell's voltage-gated sodium channels recognize the change in membrane potential – the difference between inter- and extra-cellular charges – and activate, drawing sodium into the downstream cell and propagating the signal without direct charge transfer through gap junctions. In this way, electrical conduction within cardiac tissue can theoretically be preserved even in the case of disrupted GJ coupling. Our lab is by no means the first to explore the possibilities of ephaptic coupling, as previous studies have complied evidence for an ephaptic mechanism over the past 70 years. In fact, the first thoughts of ephaptic coupling were not even applied to cardiac conduction, but to the brain and other nerve tissues.

THE HISTORY OF EPHAPTIC COUPLING

First, Dr. Hodgkin was able to demonstrate that the excitation of one nerve fiber was able to activate an adjacent nerve fiber [109, 110]. This was originally thought to be due to changes in membrane resistance, which would logically lead to the idea that GJ act as low-resistance pathways between high-resistance cell membranes. Furthermore, Dr. Hodgkin and colleagues demonstrated the transfer of sodium ions into the cell with the onset of an action potential [111-113] in the giant squid axon. These experiments established how intra- and extracellular charges could be changed by the transfer of ions and how ion channel gating kinetics could be influenced by membrane potential, both critical factors to ephaptic interactions. Even more impressive is that their preliminary work for these studies was tabled, in Plymouth, UK, mere days before Hitler's invasion of Poland, and only completed after the laboratory could be repaired from wartime bombing [114].

Later experiments by Drs. Snow and Dudek, performed in rat hippocampal slices, found that epileptiform bursts in the hippocampus generate large transmembrane depolarizations [115]. Their conclusions are that these transmembrane depolarizations could synchronize neuronal activity, but these results also provide evidence for the transmission of an electric signal via extracellular electric fields without direct charge transfer from cell to cell. This study was followed by a paper from Dr. Vigmond *et al* in 1997, who demonstrated a simultaneous comparison of GJ and ephaptic coupling in nerve fibers [116]. In that study, the authors combined experiments on pyramidal neurons from rat hippocampus with a 3D morphological pyramidal cell model to explore coupling mechanisms. Of particular note was their finding that decreasing the ratio between intra- and extracellular resistance decreased the effects of the electric field on the postsynaptic cell. This idea, specifically the inverse, that the effects of an ephaptic mechanism are more pronounced with reduced GJ coupling, is one that has been extensively demonstrated and will be discussed in detail below.

A particular researcher who delved into the matter of ephaptic coupling specifically in muscle tissue was Dr. Nicholas Sperelakis. The prevalent theory at the time was that cardiac cells essentially functioned as a continuous cable with a single low-resistance pathway between cells in a strand, though his experiments in 1960 demonstrated that a junctional transmission process is involved in cardiac conduction [117]. This notion was further supported by his next experiments comparing long- and short-cell muscle strands [118]. Essentially, if conduction was continuous through gap junctions, the length and number of cells in a strand of specific length should be irrelevant. However, their experiments demonstrated otherwise, indicating a more complex electrical coupling structure than had been previously considered. Still, the notion that cardiac conduction is discontinuous does not in itself confirm the presence of ephaptic coupling, as even GJ-mediated conduction has been demonstrated to be discontinuous, as described above, necessitating further evidence of an ephaptic mechanism.

In what can be considered the first demonstration of potential ephaptic transmission of signal in muscle tissue, Drs. Prosser and Sperelakis performed a series of experiments on cat intestinal muscle tissue [119]. When they cut a circumferential slit into a ring of tissue, separating it into two rings, with a salt bath between them, electrical transmission was possible if the rings were in close contact. Furthermore, electron microscopy demonstrated that the muscle fibers had no sarcoplasmic continuity between cells, leading the authors to suggest an ephaptic mechanism could be responsible for cell-to-cell transmission. These results were confirmed some 30 years later with Dr. Suenson's findings in adjacent muscle strands [120] In that study, two papillary muscle fibers were taped together, compressed, and one fiber stimulated with a constant current. At a point, the compression of the fibers increased longitudinal resistance enough to generate a large extracellular potential. A signal was then observed in the proximal fiber, which could only have been generated ephaptically, suggesting this electric field mechanism could be relevant in cardiac electrophysiology.

Still, the question of how ephaptic coupling could be achieved in intact cardiac tissue remained an unanswered question for some time. In fact it was several decades until a candidate ephapse – a location in which ephaptic coupling could occur – could be identified, when Dr. Rhett, with Ms. Jourdan and Dr. Gourdie, described the cardiac perinexus: a region <200nm long of closely-opposed membranes of adjacent cells [51]. The perinexus has been identified as a potential cardiac ephapse for two reasons. The first is the presence of an abundance of sodium channels and the second is the relatively narrow cleft between cells. Super high-resolution imaging confirmed that necessary sodium channels cluster in this region, setting the anatomical stage for ephaptic transmission [121]. It should be noted that the above history has been organized thematically, to follow the concept of ephaptic coupling from nerve to cardiac tissue, leading to the potentially critical electrophysiological role the perinexus could play. These experimental findings help investigators interpret modeling studies, which have suggested an ephaptic mechanism could play a critical role in cardiac conduction.

MATHEMATICAL MODELS OF EPHAPTIC COUPLING

One of the most influential models of cell-to-cell conduction is the Lou-Rudy (LR) model, first developed in 1991 [122], which was based off of the Beeler-Reuter model. One can wonder whether Dr. Rudy's time at Case Western Reserve University with Dr. Sperelakis could have been inspiration for examining an electric field effect in the cleft between cells. In its earliest iteration, the LR model incorporated six transmembrane potentials, including sodium, calcium and potassium and has since been updated and extended to a dynamic model (LRd) incorporating critical factors such as pump and exchanger currents and cell compartmentalization [123, 124]. These models have been used to study unidirectional block, a condition which creates an arrhythmogenic substrate [125], early after depolarizations, and conduction during ischemia. After several iterations [126, 127], the most recent LRd model, developed in 2000 [128], reformulates calcium-induced-calcium-release and sodium-activated potassium current. Specifically, it models cell behavior under sodium overload. In a 2002 publication, Drs. Kucera, Rohr and Rudy utilized this model to determine how sarcolemmal localization of sodium channels could impact cardiac conduction, specifically under differing conditions of GJ coupling and electrical resistance of the cleft between adjacent

cells [129]. Specifically, in their noncleft model, the bridge between adjacent myocytes was a single resistor representing GJ resistance, with negligible extracellular resistance and therefore negligible extracellular potential. However, in the cleft model, they also incorporated a T-junction of two cleft resistances and a radial resistance connecting the cleft to bulk extracellular space. This change allowed the extracellular potential to be nonzero only at the cleft, providing the means by which an ephaptic mechanism could occur. They additionally utilized immunocytochemistry of neonatal rat cardiomyocytes to demonstrate that sodium channels do in fact localize with connexin gap junctions at the ID, confirming earlier observations by Dr. Maier *et al* [130], and then used the LRd model to demonstrate how this ID localization affects conduction. Their findings indicate that incorporating cleft resistance when combined with localization of sodium channels and impaired GJ coupling could modulate conduction in ways that are not predicted by cable theory. They noted that at nominal GJ coupling levels, decreasing cleft width, beginning from the non-cleft model, slowed conduction as expected, likely due to increasing resistance of the extracellular return pathway. Intriguingly, with medium-range GJ coupling (3-10% of nominal coupling), a biphasic relationship was observed, wherein decreasing cleft width could actually increase CV before slowing conduction once the cleft narrowed past approximately 40nm via a mechanism of "self-attenuation." Self-attenuation is a phenomenon wherein the driving force (the difference between membrane and ionic-reversal potentials) of sodium is substantially reduced, which lowers sodium current and delays action potential generation. The driving force of an ionic current is described in Equation 1, where E_{ion} is the reversal or Nernst potential of the particular ion and V_m is the cell's membrane potential.

$$V_{DF} = E_{ion} - V_m \qquad \text{Equation 1}$$

The cause of this reduced driving force and therefore a principle of sodium self-attenuation is that a large negative cleft potential, due to localization of sodium channels and high cleft resistance, causes depolarization of both pre- and post-junctional membrane potentials, bringing V_m of adjacent cells closer to E_{ion} and the driving force closer to zero Importantly, self-attenuation was again observed with the lowest

levels of GJ coupling, which demonstrated a similar biphasic relationship between cleft width and CV: after a substantial and abrupt increase in CV with cleft widths of 40-50nm, conduction slowed with further cleft narrowing. While this study does not explicitly mention an ephaptic mechanism, subsequent models began to attribute the relationship between intercellular clefts and conduction to ephaptic coupling and found similar results where cleft width could either enhance or slow conduction. Using this model, Drs. Copene and Keener began to specifically examine the role of ephaptic coupling in cardiac cells [131], leading to yet more modeling of this electrical phenomenon.

Drs. Mori, Fishman and Peskin developed a model which, in contrast to the LRd model's 2-dimensional single-cell strands, accounted for 3-dimensional geometry [132]. Similarly to the above Kucera study, Dr. Mori and colleagues subjected their modeled cardiac strands to reduced GJ coupling and varying levels of sodium channel ID localization. Dr. Mori's results were similar to those produced by the Kucera model: under nominal GJ coupling, narrowing cleft width slowed conduction, while the same cleft narrowing had a biphasic effect on CV when GJ coupling was impaired and sodium channels localized to the lateral ends of the cells. This biphasic relationship could be explained by enhanced ephaptic coupling followed by ephaptic self-attenuation of sodium current with progressively narrower clefts. Furthermore, Dr. Mori compared different models of electrical activity with their full 3D model, including a 3D cable model which ignored ionic concentrations and the 1D cable model utilized by Dr. Kucera *et al*, described earlier [129], which also accounted for changes in extracellular ionic concentrations. They found that the 1D model significantly overestimated CV with wide intercellular clefts and underestimated CV with narrow clefts [132]. They explained this discrepancy by an effective decrease of electrical resistance in the cleft of the 3D model. Essentially, the 1D model makes it more difficult to develop a voltage gradient along the lateral edge of the cell, but once established, this gradient takes more time to decay. At very narrow clefts (<5 nm), they also noted a discrepancy between the 3D ionic concentration tracking model and exclusively electrical models, with the electrical model producing slightly higher CV than the ionic model. This

difference is due to the 3D ionic model's rapid depletion of sodium ions within the cleft which reduces the driving force of sodium across the cell membrane, resulting in self-attenuation.

Importantly, this self-attenuation is distinct from the self-attenuation described by Dr. Kucera. Instead of causing an overshoot of V_m which drives the driving force of sodium ions to zero, the reduction of driving force is instead due to the greatly reduced sodium pool available to the distal cell, which in turn reduces the Nernst potential for sodium, or more generally E_{ion} in equation 1 above. Next, Dr. Mori varied the size of the extracellular bath, or the bulk interstitial space on the lateral edge of the myocyte. They again noted a biphasic relationship between cleft width and CV for all tested conditions of GJ coupling and extracellular bath size. Interestingly, they observed clefts <9nm could preserve conduction with zero GJ coupling, indicating that ephaptic coupling alone could theoretically achieve cell-to-cell conduction.

As Dr. Mori and colleagues noted, a chief concern with all mathematical modeling is the tradeoff between computational efficiency and physiological relevance. To this end, Drs. Lin and Keener developed a 1D strand model which aimed to more accurately capture effects of cell geometry and ephaptic coupling [133]. Drs. Lin and Keener question the utility of cable theory in the context of cardiomyocytes, in contrast with its appropriate applicability to neuronal axons and argue that the resistance of the extracellular space is a more important determinant of conduction than intracellular resistance. Thus, in their model the intracellular space of each cell is assumed to be isopotential, while spatial electric potential variations exist in the extracellular compartments. Quantitatively, intracellular conductance is approximately two orders of magnitude greater than extracellular conductance. With this model, ephaptic coupling is found to enhance conduction under conditions of reduced GJ coupling, similar to the previous models described above. Furthermore, Lin and Keener found that with sodium channels localized to the ends of the cells and narrow clefts, conduction was insensitive to GJ uncoupling, again bearing resemblance to the results of the Dr. Mori study. In a subsequent study, using the same model, they looked further into the effects of ephaptic parameters on conduction under different conditions of GJ coupling and interstitial space [134].

Importantly, they also detailed conductions in two directions: transverse and longitudinal, and ratio of anisotropy (AR), which is an important factor in arrhythmogenesis. Compared with a bidomain cable model, their ephaptic model, including 100% localization of sodium current at the ends of the cells, slowed longitudinal conduction but increased transverse conduction and reduced AR with a cleft width of $1.5x10^{-6}$ cm. With reduced GJ coupling (~6-fold reduction in GJ conductance) and the same cleft width, the ephaptic model increased longitudinal conduction and further increased transverse conduction, lowering AR to an even greater extent. Their results with reduced GJ coupling a cleft with of $1.5x10^{-5}$ cm, an order of magnitude narrower than before, are particularly interesting. It is under these conditions that a relationship is established between interstitial space and conduction. Transverse conduction is increased relative to the cable model, as before. Transverse conduction, however, is faster in the ephaptic model with small extracellular volume fractions than in the cable model. The conduction values then sharply decrease as extracellular space expands and conduction approaches cable-model values. These results suggest ephaptic coupling could compensate for impaired GJ coupling and increased interstitial resistance, but this effect diminishes as bulk interstitial resistance, and therefore overall cleft resistance and current, decreases.

While these studies have focused on the depolarization phase of the action potential and how sodium current can be enhanced or attenuated to affect the depolarization of a second cell, it is important to note that the same concepts can affect the repolarization phase as well, as demonstrated by a modeling and experimental study performed by Drs. Greer-Short, Poelzing, and Weinberg [135]. Utilizing a similar model to the Kucera model detailed above [129] along with guinea pig whole-heart Langendorff preparations, the authors speculated whether the same self-attenuation principle described earlier could mask Long-QT type 3 (LQT3) syndrome. In principle, a narrower cleft would counteract the gain-of-function mutations in voltage-gated sodium channels, preventing early afterdepolarizations which are a hallmark of LQT3. The computer model indicated that indeed cleft width could drastically impact action potential duration (APD) along with CV in simulated myocyte strands containing either wild-type cells or a sodium channel mutant. Essentially, a narrow cleft width would facilitate ionic sodium depletion in the cleft with an enhanced late

sodium current, and this would reduce the driving force, and thereby the late current. In effect, sodium channels could be conductive late in repolarization, but due to reduced driving force, the current would be insufficient to prolong the action potential. This concealed sodium channel gain of function occurred up to a cleft with of approximately 20m, after which the mutant cell strand began to exhibit prolonged APD. In a whole-heart guinea pig preparation, they then utilized a late-sodium current agonist, ATXII, which had no significant effect on perinexal width but prolonged APD, and mannitol, which on its own had no effect on APD but expanded the perinexus, to present an "unmasked" LQT3 model. The combination of ATXII and mannitol resulted in significantly prolonged APDs, presumably due to early afterdepolarizations which had been absent from hearts perfused with only one of the substances. With this data, the authors suggest that the self-attenuation which had previously been shown to slow or disrupt conduction could actually be potentially beneficial in the context of a gain-of-function arrhythmogenic disease.

The above models continue to raise questions about the relationship between cable and ephaptic mechanisms of conduction, along with situational conduction disruptions and benefits of self-attenuation. To further explore these issues and identify translational aspects of these mechanisms, finding evidence of an ephaptic mechanism became a renewed experimental focus.

EXPERIMENTAL EPHAPTIC EVIDENCE

It is of particular interest that the cleft width for effective ephaptic coupling described in the above modeling studies is within a range of approximately 10-100nm. Experiments performed by Drs. Rhett, Veeraraghavan and George [52, 121, 136] as well as our recent clinical work [137] have identified perinexal spacing in electron micrographs of mouse, guinea pig and human cardiomyocytes, to fall precisely within a 10-30nm range, though it is unknown if these are truly representative of *in-vivo* physiology. Furthermore, Dr. Veeraraghavan *et al* [121] observed perinexal expansion with the addition of mannitol, causing acute interstitial edema, correlating with decreased CV. Importantly, they also observed clustering of sodium channels at the ID within 200nm of GJ plaques, consistent with the location of the perinexus. In the same

study, they utilized the same Lin-Keener model as described above to demonstrate a relationship between conduction and structural changes, including perinexal width and GJ uncoupling, could be mathematically predicted when sodium channels were clustered at the ID, supporting their experimental findings.

Drs. Hichri, Abriel and Kucera added further support to the electrophysiological importance of sodium channel clustering and cleft width in their recent experimental and modeling study [138]. In this study, they considered two mathematical scenarios: first, the behavior of a cell separated by a cleft from a non-conducting obstacle and second, the case of two opposed excitable membranes, as would be found in the ID between cardiomyocytes. In the first condition, when a voltage was applied (-25 mV) far above the activation potential of sodium channels, they observed self-attenuation, as peak sodium current was reduced with narrower clefts due to an increasingly negative cleft potential. At a voltage step closer (-50 mV) to the activation threshold of sodium channels, they observed intriguing electrical behavior. The modelers described a biphasic relationship between cleft width and sodium current, with strongly attenuated current associated with clefts between 10-80 nm. The difference was due to inhomogeneity within the cross-sectional surface of the disc. A highly negative voltage built up within the center of the disc, accelerating the activation and then inactivation of the sodium channels near the center, while at the periphery, the change in cleft potential occurred more slowly, leading to a later but more intense sodium current. Within narrow clefts, the same self-attenuation as described above was observed, as the global potential changed rapidly in the small cleft. However, in larger clefts, the self-activating feedback mechanism was able to occur and drive overall sodium current without self-attenuation. With wider clefts, even though peak sodium current was greater, cleft potential became abruptly negative, quickly decreasing driving force and producing a lower current over the time course of activation. This model gives further insight into the mechanics of self-attenuation and the cleft conditions for optimal ephaptic interaction. The authors also, however, aimed to examine the second critical factor governing ephaptic coupling, the clustering of sodium channels. They modeled sodium channel clusters as a fraction of the whole cleft cross-sectional area, from 1 (evenly dispersed) to 0.125 (a pinhole in the center of the cleft). They again performed a series of

simulations for voltage steps far above (-25 mV) and close to (-50 mV) the sodium channel activation threshold and noted at which cleft width the greatest peak current occurred. With the greater voltage step, greatest peak current was achieved and maintained for all cleft widths above ~160 nm for all cluster sizes at nominal sodium channel conductivity, indicating self-attenuation at narrower clefts. With the smaller voltage step, they again observed a biphasic relationship between cleft width and peak current. Interestingly, this peak occurred at different cleft widths for different cluster sizes, and did not occur at all for the uniform distribution condition. The current of less highly-concentrated conditions peaked at narrower clefts and then sharply dropped off, while at lower concentrations, the peak was higher and occurred with a wider cleft. This biphasic relationship can be attributed to the above-described self-activating feedback loop peaking and then was overshadowed by the negative change of a greater cleft, with more highly-concentrated sodium clusters more quickly driving cleft potential negative and therefore inactivating sodium channels. The authors simultaneously performed patch clamp experiments in isolated human embryonic kidney cells and approached them towards a glass obstacle before pulling them away, to decrease and then increase the cleft width, mimicking the above simulations. They found a similar self-attenuation to self-activation pattern as described above, as at a very high voltage step, decreasing the extracellular space attenuated sodium current as predicted by the model. With the smaller voltage step, however, the authors noted an increase in peak sodium current with the smaller cleft and attributed this change to the self-activation of sodium channels they observed in the simulations.

Of final note to our discussion, the authors considered the simulated conditions of varying sodium channel cluster sizes and positions in opposed cell membranes. Each opposed cleft contained one cluster of sodium channels and the centers of these clusters were progressively moved away from each other. They observed the previously-described self-activation only when the cluster centers were close to each other (<5.5 μm apart) and that cluster size and location determined the cleft widths at which activation of the second membrane could be achieved ephaptically. For large distances between clusters and/or wide clefts, sodium current could not be activated in the second membrane, due to the inability of the first cell's sodium channels to sufficiently change local extracellular cleft potential to activate the distal cell's sodium

channels. This study as a whole provides extensive insight into how self-activation of sodium current can be achieved and the ephaptic interactions between cells that can either self-attenuate or enhance sodium currents. This study elegantly demonstrated a more refined model of the previously-described interactions between ID structure and conduction and provides further evidence that ephaptic coupling could play a critical role in cardiac conduction under specific conditions.

Though the modeling and experimental evidence for the role of ephaptic coupling has been encouraging, the question remains how it could be translated to clinical application and whether the perinexus could indeed present a therapeutic target for arrhythmic conditions. In a later chapter, I will describe how study of perinexi in open-heart surgery patients both confirms the perinexus is not a rodent-specific structure and that the perinexus could play a role in atrial fibrillation [137]. This finding, in conjunction with previous modeling and experimental evidence, has fueled optimism that the perinexus could be utilized as a therapeutic target for arrhythmogenic disease [139]. Recently, Dr. Veeraraghavan *et al* noted that the β1 subunit of the cardiac sodium channel could regulate membrane adhesion at the perinexus, potentially identifying such a target [140]. They developed a peptide, βadp1, which acts as a selective inhibitor of β1 adhesion. Both the application of this peptide and the genetic knockout of β1 resulted in expanded perinexi, though unchanged non-junctional ID widths, along with slowed CV. Targeted expansion of the perinexus correlating with slowed conduction further supports an ephaptic mechanism of conduction in mammalian cardiac tissue, and is consistent with the above mathematical models and experimental data.

CONCLUSIONS

Throughout the past century, scientists have performed elegant experiments and simulations to identify conduction mechanisms and isolate structures which could be therapeutic targets. Questions still remain, however, as to the dominant mechanism of cardiac conduction – gap junctional or ephaptic – and whether conduction can be improved by perinexal narrowing alone. Throughout this dissertation I will argue that

the cardiac perinexus is a critically important structure that could potentially be utilized as a therapeutic target to better treat arrhythmogenic diseases due to its status as a cardiac ephapse.

REFERENCES

1. Venes, D., *Taber's Cyclopedic Medical Dictionary*. 2009.
2. Kuehnel, W., *Color Atlas of Cytology, Histology and Microscopic Anatomy: 4th Edition*. 2004, Thieme Medical Publishers, Incorporated.
3. van Weerd, J.H. and V.M. Christoffels, *The formation and function of the cardiac conduction system.* Development, 2016. **143**(2): p. 197-210.
4. Womble, J.G.B.D.H.K.K.A.Y.P.D.B.P.O.K.J.A.W.E.J.J.E.J.M., *Anatomy and Physiology by OpenStax*. 2013, XanEdu Publishing Inc.
5. Hodgkin, A.L. and P. Horowicz, *Movements of Na and K in single muscle fibres.* J Physiol, 1959. **145**(2): p. 405-32.
6. Amin, A.S., H.L. Tan, and A.A. Wilde, *Cardiac ion channels in health and disease.* Heart Rhythm, 2010. **7**(1): p. 117-26.
7. Priest, B.T. and J.S. McDermott, *Cardiac ion channels.* Channels (Austin), 2015. **9**(6): p. 352-9.
8. Fawcett, D.W. and N.S. McNutt, *The ultrastructure of the cat myocardium. I. Ventricular papillary muscle.* J Cell Biol, 1969. **42**(1): p. 1-45.
9. McNutt, N.S. and D.W. Fawcett, *The ultrastructure of the cat myocardium. II. Atrial muscle.* J Cell Biol, 1969. **42**(1): p. 46-67.
10. Hayashi, T., et al., *Three-dimensional electron microscopy reveals new details of membrane systems for Ca2+ signaling in the heart.* J Cell Sci, 2009. **122**(Pt 7): p. 1005-13.
11. Pinali, C., et al., *Three-dimensional reconstruction of cardiac sarcoplasmic reticulum reveals a continuous network linking transverse-tubules: this organization is perturbed in heart failure.* Circ Res, 2013. **113**(11): p. 1219-30.
12. Risi, C., et al., *Ca(2+)-induced movement of tropomyosin on native cardiac thin filaments revealed by cryoelectron microscopy.* Proceedings of the National Academy of Sciences U S A, 2017. **114**(26): p. 6782-6787.
13. Fisch, C., et al., *Potassium and the monophasic action potential, electrocardiogram, conduction and arrhythmias.* Prog Cardiovasc Dis, 1966. **8**(5): p. 387-418.
14. Pertsov, A., R.D. Walton, and O. Bernus, *Optical Imaging of Cardiac Action Potential.* Adv Exp Med Biol, 2015. **859**: p. 299-311.
15. Trenor, B., et al., *Cardiac action potential repolarization revisited: early repolarization shows all-or-none behaviour.* J Physiol, 2017. **595**(21): p. 6599-6612.
16. Barr, L., M.M. Dewey, and W. Berger, *Propagation of Action Potentials and the Structure of the Nexus in Cardiac Muscle.* J Gen Physiol, 1965. **48**: p. 797-823.
17. Hodgkin, A.L. and A.F. Huxley, *Propagation of electrical signals along giant nerve fibers.* Proc R Soc Lond B Biol Sci, 1952. **140**(899): p. 177-83.
18. Rudy, Y., *The ionic mechanisms of conduction in cardiac tissue.* J Electrocardiol, 2001. **34 Suppl**: p. 65-8.
19. Shaw, R.M. and Y. Rudy, *Ionic mechanisms of propagation in cardiac tissue. Roles of the sodium and L-type calcium currents during reduced excitability and decreased gap junction coupling.* Circ Res, 1997. **81**(5): p. 727-41.
20. Garratt, C.J., *Mechanisms and Management of Cardiac Arrhythmias*. 2001, BMJ Books.
21. Barman, P.P., Venebles, Paul, Tomlinson, David R., *Supraventricular and ventricular arrhythmias: medical management.* Medicine, 2018. **46**(10): p. 632-639.
22. Stanfield, C.L., *Principles of Human Physiology, 6th Edition*. 2007, Pearson.
23. Goodman, D.J., et al., *The effect of cycle length on cardiac refractory periods in the denervated human heart.* Am Heart J, 1976. **91**(3): p. 332-8.
24. Kumagai, K., et al., *Electrophysiological properties in chronic lone atrial fibrillation.* Circulation, 1991. **84**(4): p. 1662-8.
25. Misier, A.R., et al., *Increased dispersion of "refractoriness" in patients with idiopathic paroxysmal atrial fibrillation.* J Am Coll Cardiol, 1992. **19**(7): p. 1531-5.

26. Mohri, S., et al., *Cardiac contractility modulation by electric currents applied during the refractory period.* Am J Physiol Heart Circ Physiol, 2002. **282**(5): p. H1642-7.
27. Mohri, S., et al., *Electric currents applied during refractory period enhance contractility and systolic calcium in the ferret heart.* Am J Physiol Heart Circ Physiol, 2003. **284**(4): p. H1119-23.
28. Nakahara, S., et al., *Characterization of the arrhythmogenic substrate in ischemic and nonischemic cardiomyopathy implications for catheter ablation of hemodynamically unstable ventricular tachycardia.* J Am Coll Cardiol, 2010. **55**(21): p. 2355-65.
29. McDowell, K.S., et al., *Susceptibility to arrhythmia in the infarcted heart depends on myofibroblast density.* Biophys J, 2011. **101**(6): p. 1307-15.
30. de Diego, C., et al., *Electrophysiological consequences of acute regional ischemia/reperfusion in neonatal rat ventricular myocyte monolayers.* Circulation, 2008. **118**(23): p. 2330-7.
31. Agullo-Pascual, E., M. Cerrone, and M. Delmar, *Arrhythmogenic cardiomyopathy and Brugada syndrome: diseases of the connexome.* FEBS Lett, 2014. **588**(8): p. 1322-30.
32. Amin, A.S., A. Asghari-Roodsari, and H.L. Tan, *Cardiac sodium channelopathies.* Pflugers Arch, 2010. **460**(2): p. 223-37.
33. Amin, A.S., et al., *Fever-triggered ventricular arrhythmias in Brugada syndrome and type 2 long-QT syndrome.* Neth Heart J, 2010. **18**(3): p. 165-9.
34. Antzelevitch, C. and E. Nof, *Brugada syndrome: recent advances and controversies.* Curr Cardiol Rep, 2008. **10**(5): p. 376-83.
35. Antzelevitch, C. and G.X. Yan, *J-wave syndromes: Brugada and early repolarization syndromes.* Heart Rhythm, 2015.
36. Akoum, N., et al., *Atrial fibrosis helps select the appropriate patient and strategy in catheter ablation of atrial fibrillation: a DE-MRI guided approach.* J Cardiovasc Electrophysiol, 2011. **22**(1): p. 16-22.
37. Akoum, N., et al., *Atrial fibrosis quantified using late gadolinium enhancement MRI is associated with sinus node dysfunction requiring pacemaker implant.* J Cardiovasc Electrophysiol, 2012. **23**(1): p. 44-50.
38. Barman, M., *Proarrhythmic Effects Of Antiarrhythmic Drugs: Case Study Of Flecainide Induced Ventricular Arrhythmias During Treatment Of Atrial Fibrillation.* J Atr Fibrillation, 2015. **8**(4): p. 1091.
39. Benjamin, E.J., et al., *Impact of atrial fibrillation on the risk of death: the Framingham Heart Study.* Circulation, 1998. **98**(10): p. 946-52.
40. Borzak, S., et al., *Atrial fibrillation after bypass surgery: does the arrhythmia or the characteristics of the patients prolong hospital stay?* Chest, 1998. **113**(6): p. 1489-91.
41. Levy, S., *Factors predisposing to the development of atrial fibrillation.* Pacing Clin Electrophysiol, 1997. **20**(10 Pt 2): p. 2670-4.
42. Chakko, S. and K.M. Kessler, *Recognition and management of cardiac arrhythmias.* Curr Probl Cardiol, 1995. **20**(2): p. 53-117.
43. Benjamin, E.J., et al., *Heart Disease and Stroke Statistics-2017 Update: A Report From the American Heart Association.* Circulation, 2017. **135**(10): p. e146-e603.
44. January, C.T., et al., *2014 AHA/ACC/HRS guideline for the management of patients with atrial fibrillation: a report of the American College of Cardiology/American Heart Association Task Force on Practice Guidelines and the Heart Rhythm Society.* J Am Coll Cardiol, 2014. **64**(21): p. e1-76.
45. Saffitz, J.E., K.G. Green, and R.B. Schuessler, *Structural determinants of slow conduction in the canine sinus node.* J Cardiovasc Electrophysiol, 1997. **8**(7): p. 738-44.
46. Pieperhoff, S., et al., *The area composita of adhering junctions connecting heart muscle cells of vertebrates. VII. The different types of lateral junctions between the special cardiomyocytes of the conduction system of ovine and bovine hearts.* Eur J Cell Biol, 2010. **89**(5): p. 365-78.
47. Mezzano, V., J. Pellman, and F. Sheikh, *Cell junctions in the specialized conduction system of the heart.* Cell Commun Adhes, 2014. **21**(3): p. 149-59.

48. Liao, W.C., et al., *HSPB7 prevents cardiac conduction system defect through maintaining intercalated disc integrity.* PLoS Genet, 2017. **13**(8): p. e1006984.
49. Radwanski, P.B., et al., *Cardiac Arrhythmias as Manifestations of Nanopathies: An Emerging View.* Front Physiol, 2018. **9**: p. 1228.
50. Veeraraghavan, R., S. Poelzing, and R.G. Gourdie, *Intercellular electrical communication in the heart: a new, active role for the intercalated disk.* Cell Commun Adhes, 2014. **21**(3): p. 161-7.
51. Rhett, J.M. and R.G. Gourdie, *The perinexus: a new feature of Cx43 gap junction organization.* Heart Rhythm, 2012. **9**(4): p. 619-23.
52. Rhett, J.M., et al., *Cx43 associates with Na(v)1.5 in the cardiomyocyte perinexus.* Journal of Membrane Biology, 2012. **245**(7): p. 411-22.
53. Rhett, J.M., et al., *The perinexus: Sign-post on the path to a new model of cardiac conduction?* Trends in Cardiovascular Medicine, 2013.
54. Nielsen, M.S., Axelse, L.N., Sorgen, P.L., Verma, V., Delmar, M. Holstein-Rathlou, N., *Gap Junctions.* Compr Physiol, 2013.
55. Brooke, M.A., D. Nitoiu, and D.P. Kelsell, *Cell-cell connectivity: desmosomes and disease.* J Pathol, 2012. **226**(2): p. 158-71.
56. Wallis, S., et al., *The alpha isoform of protein kinase C is involved in signaling the response of desmosomes to wounding in cultured epithelial cells.* Mol Biol Cell, 2000. **11**(3): p. 1077-92.
57. Bouvier, D., et al., *Characterization of the structure and intermolecular interactions between the connexin40 and connexin43 carboxyl-terminal and cytoplasmic loop domains.* J Biol Chem, 2009. **284**(49): p. 34257-71.
58. Spagnol, G., et al., *Secondary structural analysis of the carboxyl-terminal domain from different connexin isoforms.* Biopolymers, 2016. **105**(3): p. 143-62.
59. Beauchamp, P., et al., *Electrical coupling and propagation in engineered ventricular myocardium with heterogeneous expression of connexin43.* Circ Res, 2012. **110**(11): p. 1445-53.
60. Caspar, D.L., et al., *Gap junction structures. I. Correlated electron microscopy and x-ray diffraction.* J Cell Biol, 1977. **74**(2): p. 605-28.
61. Rohr, S., *Role of gap junctions in the propagation of the cardiac action potential.* Cardiovasc Res, 2004. **62**(2): p. 309-22.
62. Rudisuli, A. and R. Weingart, *Electrical properties of gap junction channels in guinea-pig ventricular cell pairs revealed by exposure to heptanol.* Pflugers Arch, 1989. **415**(1): p. 12-21.
63. Severs, N.J., et al., *Remodelling of gap junctions and connexin expression in diseased myocardium.* Cardiovasc Res, 2008. **80**(1): p. 9-19.
64. Smyth, J.W., et al., *Limited forward trafficking of connexin 43 reduces cell-cell coupling in stressed human and mouse myocardium.* J Clin Invest, 2010. **120**(1): p. 266-79.
65. Segretain, D. and M.M. Falk, *Regulation of connexin biosynthesis, assembly, gap junction formation, and removal.* Biochim Biophys Acta, 2004. **1662**(1-2): p. 3-21.
66. Simpson, I., B. Rose, and W.R. Loewenstein, *Size limit of molecules permeating the junctional membrane channels.* Science, 1977. **195**(4275): p. 294-6.
67. Goodenough, D.A. and D.L. Paul, *Gap junctions.* Cold Spring Harb Perspect Biol, 2009. **1**(1): p. a002576.
68. Esseltine, J.L. and D.W. Laird, *Next-Generation Connexin and Pannexin Cell Biology.* Trends Cell Biol, 2016. **26**(12): p. 944-955.
69. Delmar, M. and N. Makita, *Cardiac connexins, mutations and arrhythmias.* Curr Opin Cardiol, 2012. **27**(3): p. 236-41.
70. Leybaert, L., et al., *Connexins in Cardiovascular and Neurovascular Health and Disease: Pharmacological Implications.* Pharmacol Rev, 2017. **69**(4): p. 396-478.
71. Leo-Macias, A., E. Agullo-Pascual, and M. Delmar, *The cardiac connexome: Non-canonical functions of connexin43 and their role in cardiac arrhythmias.* Semin Cell Dev Biol, 2016. **50**: p. 13-21.

72. Gourdie, R.G., *The Cardiac Gap Junction has Discrete Functions in Electrotonic and Ephaptic Coupling.* Anat Rec (Hoboken), 2019. **302**(1): p. 93-100.
73. Sohl, G. and K. Willecke, *Gap junctions and the connexin protein family.* Cardiovasc Res, 2004. **62**(2): p. 228-32.
74. Bruzzone, R., T.W. White, and D.L. Paul, *Connections with connexins: the molecular basis of direct intercellular signaling.* Eur J Biochem, 1996. **238**(1): p. 1-27.
75. Beyer, E.C., D.L. Paul, and D.A. Goodenough, *Connexin family of gap junction proteins.* J Membr Biol, 1990. **116**(3): p. 187-94.
76. Haefliger, J.A., et al., *Four novel members of the connexin family of gap junction proteins. Molecular cloning, expression, and chromosome mapping.* J Biol Chem, 1992. **267**(3): p. 2057-64.
77. Bevans, C.G., et al., *Isoform composition of connexin channels determines selectivity among second messengers and uncharged molecules.* J Biol Chem, 1998. **273**(5): p. 2808-16.
78. Sohl, G. and K. Willecke, *An update on connexin genes and their nomenclature in mouse and man.* Cell Commun Adhes, 2003. **10**(4-6): p. 173-80.
79. Davis, L.M., et al., *Gap junction protein phenotypes of the human heart and conduction system.* J Cardiovasc Electrophysiol, 1995. **6**(10 Pt 1): p. 813-22.
80. Salameh, A. and S. Dhein, *Adrenergic control of cardiac gap junction function and expression.* Naunyn Schmiedebergs Arch Pharmacol, 2011. **383**(4): p. 331-46.
81. Jansen, J.A., et al., *Cardiac connexins and impulse propagation.* J Mol Cell Cardiol, 2010. **48**(1): p. 76-82.
82. Lo, C.W., *Role of gap junctions in cardiac conduction and development: insights from the connexin knockout mice.* Circ Res, 2000. **87**(5): p. 346-8.
83. De Mello, W.C., *Modulation of junctional permeability.* Fed Proc, 1984. **43**(12): p. 2692-6.
84. Francis, D., et al., *Connexin diversity and gap junction regulation by pHi.* Dev Genet, 1999. **24**(1-2): p. 123-36.
85. Lowenstein, W.R., *Regulation of cell-to-cell communication by phosphorylation.* Biochem Soc Symp, 1985. **50**: p. 43-58.
86. Solan, J.L. and P.D. Lampe, *Specific Cx43 phosphorylation events regulate gap junction turnover in vivo.* FEBS Lett, 2014. **588**(8): p. 1423-9.
87. Ek-Vitorin, J.F., et al., *Selectivity of connexin 43 channels is regulated through protein kinase C-dependent phosphorylation.* Circ Res, 2006. **98**(12): p. 1498-505.
88. Hund, T.J., et al., *Protein kinase Cepsilon mediates salutary effects on electrical coupling induced by ischemic preconditioning.* Heart Rhythm, 2007. **4**(9): p. 1183-93.
89. Rhett, J.M., J. Jourdan, and R.G. Gourdie, *Connexin 43 connexon to gap junction transition is regulated by zonula occludens-1.* Mol Biol Cell, 2011. **22**(9): p. 1516-28.
90. Nadim, F. and J. Golowasch, *Signal transmission between gap-junctionally coupled passive cables is most effective at an optimal diameter.* J Neurophysiol, 2006. **95**(6): p. 3831-43.
91. Keener, J.P., *The effects of gap junctions on propagation in myocardium: a modified cable theory.* Ann N Y Acad Sci, 1990. **591**: p. 257-77.
92. Joyner, R.W., et al., *Propagation through electrically coupled cells. Effects of a resistive barrier.* Biophys J, 1984. **45**(5): p. 1017-25.
93. Henriquez, C.S., *Simulating the electrical behavior of cardiac tissue using the bidomain model.* Crit Rev Biomed Eng, 1993. **21**(1): p. 1-77.
94. Johnston, B.M., *Six Conductivity Values to Use in the Bidomain Model of Cardiac Tissue.* IEEE Trans Biomed Eng, 2016. **63**(7): p. 1525-31.
95. Johnston, B.M., et al., *Quantifying the effect of uncertainty in input parameters in a simplified bidomain model of partial thickness ischaemia.* Med Biol Eng Comput, 2018. **56**(5): p. 761-780.
96. Cole, W.C., J.B. Picone, and N. Sperelakis, *Gap junction uncoupling and discontinuous propagation in the heart. A comparison of experimental data with computer simulations.* Biophys J, 1988. **53**(5): p. 809-18.

97. Heppner, D.B. and R. Plonsey, *Simulation of electrical interaction of cardiac cells.* Biophys J, 1970. **10**(11): p. 1057-75.
98. Kiernan, M.C., *Some do not like it hot.* J Physiol, 2017. **595**(11): p. 3251-3252.
99. Rohr, S., J.P. Kucera, and A.G. Kleber, *Slow conduction in cardiac tissue, I: effects of a reduction of excitability versus a reduction of electrical coupling on microconduction.* Circ Res, 1998. **83**(8): p. 781-94.
100. Eloff, B.C., et al., *High resolution optical mapping reveals conduction slowing in connexin43 deficient mice.* Cardiovasc Res, 2001. **51**(4): p. 681-90.
101. Morley, G.E., D. Vaidya, and J. Jalife, *Characterization of conduction in the ventricles of normal and heterozygous Cx43 knockout mice using optical mapping.* J Cardiovasc Electrophysiol, 2000. **11**(3): p. 375-7.
102. Beauchamp, P., et al., *Electrical propagation in synthetic ventricular myocyte strands from germline connexin43 knockout mice.* Circ Res, 2004. **95**(2): p. 170-8.
103. Weidmann, S., *The electrical constants of Purkinje fibres.* J Physiol, 1952. **118**(3): p. 348-60.
104. Gleixner, R. and P. Fromherz, *The extracellular electrical resistivity in cell adhesion.* Biophys J, 2006. **90**(7): p. 2600-11.
105. Kleber, A.G. and C.B. Riegger, *Electrical constants of arterially perfused rabbit papillary muscle.* J Physiol, 1987. **385**: p. 307-24.
106. Fleischhauer, J., L. Lehmann, and A.G. Kleber, *Electrical resistances of interstitial and microvascular space as determinants of the extracellular electrical field and velocity of propagation in ventricular myocardium.* Circulation, 1995. **92**(3): p. 587-94.
107. Veeraraghavan, R., M.E. Salama, and S. Poelzing, *Interstitial volume modulates the conduction velocity-gap junction relationship.* Am J Physiol Heart Circ Physiol, 2012. **302**(1): p. H278-86.
108. Sperelakis, N., *An electric field mechanism for transmission of excitation between myocardial cells.* Circ Res, 2002. **91**(11): p. 985-7.
109. Hodgkin, A.L., *Evidence for electrical transmission in nerve: Part I.* J Physiol, 1937. **90**(2): p. 183-210.
110. Hodgkin, A.L., *Evidence for electrical transmission in nerve: Part II.* J Physiol, 1937. **90**(2): p. 211-32.
111. Hodgkin, A.L. and A.F. Huxley, *Currents carried by sodium and potassium ions through the membrane of the giant axon of Loligo.* J Physiol, 1952. **116**(4): p. 449-72.
112. Hodgkin, A.L. and A.F. Huxley, *The components of membrane conductance in the giant axon of Loligo.* J Physiol, 1952. **116**(4): p. 473-96.
113. Hodgkin, A.L. and A.F. Huxley, *The dual effect of membrane potential on sodium conductance in the giant axon of Loligo.* J Physiol, 1952. **116**(4): p. 497-506.
114. Huxley, A.F., *Hodgkin and the action potential 1935-1952.* J Physiol, 2002. **538**(Pt 1): p. 2.
115. Snow, R.W. and F.E. Dudek, *Electrical fields directly contribute to action potential synchronization during convulsant-induced epileptiform bursts.* Brain Res, 1984. **323**(1): p. 114-8.
116. Vigmond, E.J., et al., *Mechanisms of electrical coupling between pyramidal cells.* J Neurophysiol, 1997. **78**(6): p. 3107-16.
117. Sperelakis, N., et al., *Intracellular and external recording from frog ventricular fibers during hypertonic perfusion.* Am J Physiol, 1960. **198**: p. 135-40.
118. Hoshiko, T., N. Sperelakis, and R.M. Berne, *Evidence for nonsyncytial nature of cardiac muscle from impedance measurements.* Proc Soc Exp Biol Med, 1959. **101**: p. 602-4.
119. Prosser, C.L. and N. Sperelakis, *Transmission in ganglion-free circular muscle from the cat intestine.* Am J Physiol, 1956. **187**(3): p. 536-45.
120. Suenson, M., *Ephaptic impulse transmission between ventricular myocardial cells in vitro.* Acta Physiol Scand, 1984. **120**(3): p. 445-55.
121. Veeraraghavan, R., et al., *Sodium channels in the Cx43 gap junction perinexus may constitute a cardiac ephapse: an experimental and modeling study.* Pflugers Archiv: European Journal of Physiology, 2015.

122. Luo, C.H. and Y. Rudy, *A model of the ventricular cardiac action potential. Depolarization, repolarization, and their interaction.* Circ Res, 1991. **68**(6): p. 1501-26.
123. Luo, C.H. and Y. Rudy, *A dynamic model of the cardiac ventricular action potential. I. Simulations of ionic currents and concentration changes.* Circ Res, 1994. **74**(6): p. 1071-96.
124. Luo, C.H. and Y. Rudy, *A dynamic model of the cardiac ventricular action potential. II. Afterdepolarizations, triggered activity, and potentiation.* Circ Res, 1994. **74**(6): p. 1097-113.
125. Shaw, R.M. and Y. Rudy, *The vulnerable window for unidirectional block in cardiac tissue: characterization and dependence on membrane excitability and intercellular coupling.* J Cardiovasc Electrophysiol, 1995. **6**(2): p. 115-31.
126. Zeng, J., et al., *Two components of the delayed rectifier K+ current in ventricular myocytes of the guinea pig type. Theoretical formulation and their role in repolarization.* Circ Res, 1995. **77**(1): p. 140-52.
127. Viswanathan, P.C., R.M. Shaw, and Y. Rudy, *Effects of IKr and IKs heterogeneity on action potential duration and its rate dependence: a simulation study.* Circulation, 1999. **99**(18): p. 2466-74.
128. Faber, G.M. and Y. Rudy, *Action potential and contractility changes in [Na(+)](i) overloaded cardiac myocytes: a simulation study.* Biophys J, 2000. **78**(5): p. 2392-404.
129. Kucera, J.P., S. Rohr, and Y. Rudy, *Localization of sodium channels in intercalated disks modulates cardiac conduction.* Circ Res, 2002. **91**(12): p. 1176-82.
130. Maier, S.K., et al., *An unexpected role for brain-type sodium channels in coupling of cell surface depolarization to contraction in the heart.* Proc Natl Acad Sci U S A, 2002. **99**(6): p. 4073-8.
131. Copene, E.D. and J.P. Keener, *Ephaptic coupling of cardiac cells through the junctional electric potential.* J Math Biol, 2008. **57**(2): p. 265-84.
132. Mori, Y., G.I. Fishman, and C.S. Peskin, *Ephaptic conduction in a cardiac strand model with 3D electrodiffusion.* Proc Natl Acad Sci U S A, 2008. **105**(17): p. 6463-8.
133. Lin, J. and J.P. Keener, *Modeling electrical activity of myocardial cells incorporating the effects of ephaptic coupling.* Proc Natl Acad Sci U S A, 2010. **107**(49): p. 20935-40.
134. Lin, J. and J.P. Keener, *Microdomain effects on transverse cardiac propagation.* Biophys J, 2014. **106**(4): p. 925-31.
135. Greer-Short, A., et al., *Revealing the Concealed Nature of Long-QT Type 3 Syndrome.* Circ Arrhythm Electrophysiol, 2017. **10**(2): p. e004400.
136. George, S.A., et al., *Extracellular Sodium Dependence of the Conduction Velocity-Calcium Relationship: Evidence of Ephaptic Self-Attenuation.* Am J Physiol Heart Circ Physiol, 2016: p. ajpheart 00857 2015.
137. Raisch, T.B., et al., *Intercalated Disc Extracellular Nanodomain Expansion in Patients with Atrial Fibrillation.* Frontiers in Physiology, 2018.
138. Hichri, E., H. Abriel, and J.P. Kucera, *Distribution of cardiac sodium channels in clusters potentiates ephaptic interactions in the intercalated disc.* J Physiol, 2018. **596**(4): p. 563-589.
139. Hoagland, D.T., et al., *The role of the gap junction perinexus in cardiac conduction: Potential as a novel anti-arrhythmic drug target.* Prog Biophys Mol Biol, 2018.
140. Veeraraghavan, R., et al., *The adhesion function of the sodium channel beta subunit (beta1) contributes to cardiac action potential propagation.* Elife, 2018. **7**.

CHAPTER 2: INTERCALATED DISC EXTRACELLULAR NANODOMAIN EXPANSION IN PATIENTS WITH ATRIAL FIBRILLATION

FOREWORD

The main goal of this dissertation is to examine the mechanisms of cardiac conduction and identify potential targetable structures which could be utilized in the treatment of arrhythmogenic diseases. I had the opportunity early in my graduate career to execute a clinical study on open-heart surgery patients to A) confirm if the perinexus, which had thus far only been observed in rodents, was conserved in humans and B) identify any association between the structure of the perinexus and human disease. This chapter both accomplishes those goals and identifies an opportunity to improve our quantification techniques, which will be discussed in future chapters.

INTRODUCTION

Atrial fibrillation (AF) is the most common cardiac arrhythmia affecting an estimated 5.2 million Americans [1]. Coordinated cardiac contraction is dependent upon organized cell-to-cell communication via the propagation of an electric signal. AF can occur secondary to disruptions in organized myocyte depolarization leading to conduction slowing and failure [2, 3].

Importantly, targetable mechanisms underlying epidemic AF are sparse. For example, a number of studies in animal models and humans have demonstrated that gap junction remodeling is associated with abnormal atrial conduction and AF [4-7]. Targeting gap junction remodeling remains challenging, and there is a critical need to expand knowledge and develop new therapeutic approaches by thinking outside the box. Recent studies suggest that gap junctions are not the only mechanism for electrical communication between cardiac myocytes. Our research suggests that ephaptic coupling, via the generation of electric fields and ion accumulation/depletion transients within restricted intercalated disc domains, can well describe a number of conduction abnormalities associated with gap junction, sodium channel, and ionic modulation [8-14].

A candidate cardiac ephapse has been identified for mediating ephaptic coupling in guinea pig and murine ventricular myocardium. This nanodomain, termed the "perinexus", is an extracellular space in the intercalated disc directly adjacent to gap junction (GJ) plaques that is narrow (on the scale of 5-30nm), can be dynamically altered, and contains a high density of the cardiac isoform of the voltage gated sodium channel[8, 9, 15, 16]. Furthermore, we have demonstrated in animal models [8, 11, 12, 17] that altering perinexal width is associated with altered cardiac conduction consistent with the theories of ephaptic coupling [18-21]. While evidence has grown suggesting the importance of non-gap junctional coupling mediating conduction velocity in animal models, it is unknown whether the perinexus can be found in human myocardium, and more specifically the atria. The purpose of this study was to identify the perinexus in human atrial tissue and provide a robust workflow for quantifying the structure. We then investigated whether perinexal morphology differed between patients with and without known pre-existing AF.

METHODS

The study was approved by the Carilion Clinic Institutional Review Board and all subjects gave informed consent prior to participating in research. Procedures followed were in accordance with institutional guidelines.

Inclusion criteria for patients enrolled in the study were: Ages 18-80, undergoing elective cardiac surgery with and without MAZE procedure at Carilion Roanoke Memorial Hospital (CRMH). Exclusion criteria were: emergent surgery, recent history of endocarditis, history of infiltrative cardiac disease, history of connective tissue disease, active steroid or immunosuppressive therapy, or repeat cardiac surgical procedure.

TISSUE COLLECTION

The day prior to the procedure, 2.5% glutaraldehyde in phosphate buffered saline (PBS) at 4^{o}C was prepared and transferred to the cardiac surgical floor in an insulated container. During surgery, the surgeon placed tissue in the fixative immediately after resection. Since all patients undergoing a MAZE procedure had pre-operative AF, surgeons were not blinded for this study. Tissue samples were collected from the right or left atrial appendage depending on the surgeon's method of cannulation for cardiac bypass. Sample were then brought to Virginia Tech Carilion Research Institute (VTCRI), cut into 1mm^3 samples, placed in newly prepared 2.5% glutaraldehyde in PBS fixative, and stored at 4^{o}C. Samples were chosen from the periphery of the specimen to ensure fixative diffusion would be adequate to minimize ex vivo changes in the tissue secondary to ischemic contraction. Tissue was washed the following day, placed in PBS, and stored at 4^{o}C prior to transport to the Virginia-Maryland College of Veterinary Medicine for transmission electron microscopy (TEM) slide preparation and imaging. 46 patients were enrolled in the study, tissue was retrieved from 39 patients, 7 patient samples were not collected as cannulation occurred outside of the atria. A total of 41 samples were collected as two patients provided samples from both the left and right atria. Three additional samples were obtained from patients without a history of AF for the purpose of immunohistochemistry.

IMMUNOFLUORESCENCE

Human right atrial tissue samples were fixed in paraformaldehyde (PFA), cryosectioned and immunolabeled following previously described collection procedures [8]. Tissue samples were fixed in PFA (2%) at room temperature for 3 hours, rinsed in phosphate buffered saline (PBS), and equilibrated sequentially in 15 and 20% solutions of sucrose at 4°C. Samples were placed into cryomolds with optimal cutting temperature (OCT) medium and frozen over liquid nitrogen. Thin sections (5 μm thickness) obtained via cryosectioning were labeled with a mouse monoclonal antibody against Cx43 (Millipore MAB3067, 1:250) and a rabbit polyclonal antibody against the voltage gated sodium channel α-subunit Nav1.5 followed by goat anti-mouse AlexaFluor 568 (1:4000) and goat anti-rabbit AlexaFluor 647 (1:4000) secondary antibodies. A separate set of thin sections were labeled with the same mouse monoclonal antibody against Cx43 and a rabbit polyclonal antibody produced by Thermo-Fisher against the β1 subunit of the Nav1.5 channel, followed by the same goat anti-mouse and goat anti-rabbit (AlexaFluor 568 and 647, respectively) secondary antibodies. Confocal imaging was performed using a TCS SP8 laser scanning confocal microscope equipped with a Plan Apochromat 63x/1.4 numerical aperture oil immersion objective and a Leica HyD hybrid detector (Leica, Buffalo Grove, IL).

TRANSMISSION ELECTRON MICROSCOPY

Samples were washed in PBS and processed for TEM as previously described [8]. Particular care was taken to quickly fix the samples in cooled glutaraldehyde and expose samples to identical fixation conditions in order to minimize heterogeneity in tissue fixation. The sample was sectioned onto copper grids and the sections were imaged using a JEOL JEM 1400 transmission electron microscope. The gap junction was identified by locating an in-plane pentalaminar structure [22, 23] with a continuously in-plane cell separation region extending at least approximately 150nm from the end of the GJ that we termed the perinexus. We collected and analyzed seven images at 150,000x magnification for each of the 39 samples included in the study. Perinexal images were then analyzed by two blinded observers using ImageJ to determine perinexal width (Wp). Importantly, the Wp measurements in this study refer to the

intermembrane separation adjacent to the GJ plaque as we previously reported in mice and guinea pigs [8, 17]. In short, a perpendicular line is drawn approximately 5nm from the edge of the gap junction and beginning of the perinexus to measure inter-membrane separation, i.e. Wp. The process is repeated at 10, and 15nm from the gap junction edge, where after Wp is quantified every 15nm.

STATISTICAL ANALYSIS

Statistical analysis of the data was performed using a Chi-squared test to assess differences between expected and observed frequencies of Wp measurements. The average of all 7 replicate measurements per sample was calculated and average Wp per independent sample was used to measure the Wp difference between disease-state groups, consistent with analyzing only sample averages, not replicates [24]. Differences between groups were quantified by a two-tailed Student's t-test with $p<0.05$ considered statistically significant. Additionally, a 2x2 Fisher's exact test was used to analyze differences in the number of points between adjacent measurements in order to identify the terminus of the perinexal plateau. Spearman's rank correlation was used to determine correlation between age and perinexal width. Left atrial dilation was assessed by a board certified cardiologist, and statistical difference determined by Chi-Squared analysis. All values are reported as mean ± standard deviation.

RESULTS

PATIENT DEMOGRAPHICS

A total of 39 patients undergoing cardiac surgery were included for quantifying perinexal separation (Table 1). Mean age was 67 years, 25 (64%) were male. There were 24 coronary artery bypass procedures, 22 valve procedures, 1 aortic root repair, and 10 MAZE procedures. Several patients underwent more than one procedure. Past medical history was significant for hypertension in 34 (87%) patients, diabetes mellitus in 8 (21%), chronic kidney disease (glomerular filtration rate ≤ 60 mL/min/1.73m2) in 13 (33%), and left ventricular systolic dysfunction (ejection fraction < 50%) in 5 (13%). Prior to surgery 26 (67%) patients were taking beta blockers, 22 (56%) were taking angiotensin converting enzyme inhibitors or angiotensin

receptor blockers, 30 (77%) were taking statins, 2 (5%) were taking amiodarone, 6 (15%) were taking calcium channel blockers, and 5 (13%) were regularly taking nonsteroidal anti-inflammatory medications.

All patients with a history of atrial fibrillation (AF) prior to surgery underwent a modified MAZE procedure (n=10: 3 persistent AF and 7 paroxysmal AF). Ten patients (25%) developed new AF in the immediate post-operative period (prior to hospital discharge). Nineteen patients (50%) did not demonstrate AF prior to or after surgery.

LEFT ATRIAL SIZE AND DISEASE STATE

It is well known that left atrial enlargement associates with AF recurrence and increased AF burden [25, 26]. In our study, left atrial enlargement was quantified as normal, mild, moderate and severe based on pre-surgical echocardiographic assessment for every patient. A chi-squared analysis revealed a statistically significant relationship between disease state and degree of left atrial expansion. Specifically, LA enlargement was more severe in patients with pre-existing history of AF ($p< 0.05$, Table 2).

INTERCALATED DISC SODIUM CHANNELS

Previous studies suggest that dense sodium channel expression in the intercalated disc adjacent to the gap junction is necessary for a non-gap junction mediated form of electrical communication called ephaptic coupling. More recently, we provided evidence that the gap junction-adjacent separations of membranes in the intercalated disc called the perinexus is a candidate structure for ephaptic transmission [8]. Representative confocal images from human atrial tissue in Figure 1A demonstrate dense immunosignals corresponding to the cardiac sodium channel α-subunit Nav1.5 (red) and connexin43 Cx43 (green) at sites consistent with the intercalated disc [8, 16], consistent with Nav1.5 enrichment within the perinexus surrounding Cx43 gap junctions. Importantly, this gap junction-adjacent Nav1.5 enrichment was consistent between samples from 3 different patients (data not shown). Additionally, Figure 1B demonstrates a similar enrichment of the β1 auxiliary Nav1.5 subunit (red) adjacent to Cx43 (green).

QUANTIFYING PERINEXAL WIDTH

Anatomical separations adjacent to gap junctions were quantified. Representative TEM images in Figure 2 at 6,000 and 60,000X magnification demonstrate that tissue fixation was sufficient to minimize tissue handling artifacts, particularly at the black, ribbon-like structures in the images, which are the intercalated discs. The image of a single perinexus from an atrial appendage of a human patient is shown in Figure 3A at 150,000x magnification, demonstrating separation of cell membranes immediately adjacent to the gap junction plaque. Linearizing perinexal width as a function of distance in Figure 3B, we find that both observers report Wp increases as a function of distance from the gap junction edge.

Comparing paired measurement from the first 20 samples between observers 1 and 2 reveals that measurements are well-correlated between observers (R^2=0.60, Figure 3C). Importantly, the slope (1.03± 0.02) is not significantly different from the line of identity, demonstrating that observers measure similar changes in perinexal width. However, the y-intercept is significantly different from 0 (4.90±0.36) demonstrating that one observer consistently measures a perinexal width on average 4.90 nm greater than the other. Further, mean Wp at each spatial extent and standard error for two observers are plotted in Figure 3D. Wp at one distance was compared to the value at the preceding distance. For example, both observers report that Wp at 10nm is statistically greater than the measurement at 5nm (*). After 30nm from the gap junction edge, there were no significant differences between Wp measurements. Thus, the beginning of the perinexal plateau was defined at 30nm from the start of the perinexus.

In order to reduce the statistical confounder of including an unequal spatial extent for different images, we sought to define a robust end to the perinexus plateau using a 2x2 Fisher's exact test for the number of measurements between adjacent spatial extents. For example, each observer measured equal numbers of points at 15nm and 30nm, as shown in Figure 3E. Importantly, statistical differences between the number of measurements at adjacent distances occurred beyond 105nm from the gap junction for both observers. Therefore 105nm was considered the farthest spatial extent for reliably estimating the perinexal plateau as denoted by the red vertical line. As a result, we defined mean Wp for each image using measurements between 30 and 105nm from the edge of the gap junction plaque.

PERINEXAL WIDTH AND SURGICAL PROCEDURE

Samples were collected from only the right atrial appendage (RAA) in patients without a history of AF, but a combination of left atrial appendages (LAA) and/or RAA were collected from patients with a history of AF. Representative TEM images are provided in Figure 4A (top panel) of gap junctions and perinexal regions from the same patient with a history of AF. Mean Wp for each patient was calculated from every Wp measured between 30 and 105nm for 7 images per patient, yielding a single mean Wp per patient shown in Figure 4A (bottom panel) and Table 3. Summary data from observers 1 and 2 demonstrates that Wp is wider in LAA relative to RAA in patients with a history of AF.

Next, we tested if mean Wp is greater in patients with pre-existing AF relative to those patients without a documented case of pre-existing AF. Representative TEM images are provided in Figure 4A (top panel) of gap junctions and perinexal regions from an RAA of a patient with a history of AF and a patient without a history of AF undergoing a cardiac procedure. To reduce the confounder of the four AF patients with both RAA and LAA samples, the LAA samples were excluded from analysis. Importantly, summary data from 39 patients (7 images per patient) in Figure 4B (bottom panel) and Table 3 demonstrates that both observers found patients with preoperative AF had significantly wider perinexi than non-AF patients undergoing cardiac surgery. Supplemental figures S.2.1 and S.2.2 show additional TEM images for non-AF and AF patients, respectively.

PERINEXAL WIDTH, POST-OPERATIVE AF, P-WAVE DURATION, AND AGE

In contrast to the relationship between pre-existing AF and Wp, we did not find a significant relationship between Wp and whether a patient *without* pre-existing AF developed post-operative AF (n=10 patients) prior to discharge (Table 3). Furthermore, there was no significant relationship between p-wave duration and Wp. However, this is expected as p-wave duration and AF are not tightly correlated due to factors such as the diverse etiologies leading to AF.

Interestingly, a relationship between Wp and age was observed in a post hoc analysis. Representative images from 49 and 79 year old patients without a history of AF can be seen in Figure 5A. Spearman's rank correlation was used to test the relationship between age and Wp in all 39 patients. Mean Wp was 19.7 nm (range 16-27 nm), mean age was 67 years (range 47-80 years). Importantly, Wp positively correlated with age, (Figure 5B), both in patients with and without AF.

DISCUSSION

This is the first study to identify and assess the anatomic features of the perinexus in human cardiac tissue. The study suggests that this sodium channel-rich separation of apposed membranes immediately adjacent to gap junctions is a conserved nanodomain in atrial and ventricular tissue that is species-independent: murine [17], guinea pig [8], or human. Further, this study is the first to demonstrate that mean perinexal width is a correlate of a human disease and age.

$Na_V1.5$ AND β1 ENRICHED AROUND CX43

We previously demonstrated that Nav1.5 is enriched immediately adjacent to Cx43 in confocal images of guinea pig, murine ventricles, as well as neonatal rat ventricular myocytes, indicating the gap junction perinexus could function as a cardiac ephapse [8, 16, 17, 27]. Here, we demonstrate a similar enrichment in human atrial tissue where immunosignals corresponding to Nav1.5 and its auxiliary subunit, β1 (SCN1B), were enriched immediately proximal to punctae of dense Cx43 immunosignal consistent with GJ plaques. In light of our previous results, these data are consistent with perinexal enrichment of Nav1.5 and β1 in human atria, indicating the presence of functional sodium channels at these perinexal sites [28, 29].

SUBJECTIVE MEASURE OF Wp

This is the first study to assess perinexal width in human hearts, and systematically measure variability of measurement between multiple observers in any tissue. Previously, we reported that perinexal separation in guinea pig ventricular myocardium is approximately 12nm [8]. We later found with different observers

that perinexal separation can vary between 10 and 25nm depending on the *ex vivo* perfusate used to sustain the heart through studies [11, 12, 14, 17, 30].

Interestingly, previous studies quantified mean Wp at distances greater than 30nm from the edge of the gap junction, and this is consistent with the 30nm found here. Further, the mean Wp measured in human atrial tissue in patients without pre-operative AF was consistent with results from murine and guinea pig ventricles under control conditions, suggesting that the anatomical structure is conserved across species. Altogether, the present and previous studies suggest that some differences between Wp measurements between studies may be observer-dependent. Importantly, we demonstrate here that statistically significant, disease state-dependent differences in Wp were observer independent, despite absolute differences found between observers. These results suggest that Wp could serve as a useful biomarker for cardiac disease. However, caution should be exercised when comparing absolute perinexal values between different studies and different observers.

EXTRACELLULAR EXPANSION AND AF

While this is the first study to correlate extracellular nanodomain expansion with AF, our findings are consistent with a recent study that found an increase in cardiac extracellular volume determined by magnetic resonance imaging (MRI) is a strong, independent predictor of recurrent AF following pulmonary vein isolation [31]. While these data reveal intriguing correlations, the approximate three orders of magnitude difference in scale between the domains quantified by MRI and TEM make it unlikely that perinexal expansion significantly contributes to the MRI signal. Additionally, a causal relationship remains to be established since both extracellular and perinexal volumes can be modulated by multiple factors which also produce other effects not considered here. For example, increased extracellular volume can be attributed to increased vascular permeability triggered by inflammatory cytokines. These inflammatory cytokines can alter cardiac electrophysiology by modulating functional protein expression in myocytes [32-37]. Furthermore, we have demonstrated that perinexal width can be modulated by extracellular free calcium concentrations and osmotic stress, both of which could also alter cardiac electrophysiology via second

messenger pathways and stretch-activated channels [38]. While the relative changes to perinexal width are small, they are similar to what has been previously reported experimentally and what has been suggested mathematically as being electrophysiologically relevant [19]. Further investigation will be required to determine whether perinexal expansion is a causal factor for AF, or a sequela of AF.

EXTRACELLULAR EXPANSION AND ARRHYTHMIA MECHANISMS

Atrial fibrillation incidence increases dramatically with age [39], and this study demonstrates that Wp also increases with age in patients with and without atrial fibrillation. Our recent studies suggest that patients with wide perinexi may be at higher risk for arrhythmogenic conduction slowing [8]. Perinexal expansion likely slows conduction by modulating ephaptic cell-to-cell coupling [8, 16, 17]. Theoretical studies of ephaptic coupling identify at least two structural requirements for ephaptic coupling: Cellular separation must be relatively narrow, with intercellular cleft widths on the order of 5-30 nanometers [18], and abutting membranes should densely express highly conductive ion channels. This is the first study to demonstrate that atrial myocardium meets both of these criteria. Further, increased perinexal separation in AF patients, and as we have reported in animal experiments, likely reduces this form of electrical communication even if gap junction functional expression is nominal. Lastly, gap junction remodeling, which has been extensively reported in persistent or paroxysmal AF, is also expected to modulate ephaptic-mediated conduction disturbances as we previously suggested but this requires additional investigation.

Another critical extracellular factor to consider is fibrosis, which has been strongly associated with AF [40-45]. However, we still do not understand the exact mechanism by which fibrosis can lead to AF and whether fibrosis *per se* and not other associated derangement, is the critical culprit for generation of AF. Our study, while not proving a causal relationship between Wp and AF, similarly shows an association between extracellular spaces and disrupted conduction. Our data suggests the perinexus could be yet another extracellular factor contributing to an arrhythmogenic substrate.

LIMITATIONS

Perinexal separations were obtained from 2-dimensional electron micrographs, which cannot account for the 3-dimensional structure of the perinexus. As a result, bias can be introduced into perinexal quantification. For example, images may be selected based on non-formalized criteria such as the quality of contrast, or the extent of visible membranes from the edge of a gap junction. These limitations may be accounted for by increasing both the number of perinexi measured per heart as well as by increasing the total number of hearts sampled. Additionally, the absolute values of perinexal width should be interpreted cautiously, not just because an observer may segment an image differently, but also because data obtained from an *ex vivo* glutaraldehyde-fixed preparation may not accurately reflect the *in vivo* anatomy. Taken together, measurements of the perinexus are not an exact estimate of perinexal separation *in vivo.* Additional consideration should be given to the fact that an atrial appendage will not represent biological heterogeneity expected in whole atria. Finally, only a few LAA samples were studied, and the results may not be generalized to other patient population and all findings are hypothesis generating and mandate further validation using larger cohort.

CONCLUSIONS

An extracellular nanodomain adjacent to TEM-identified gap junction plaques in humans, the perinexus, has dense sodium channel expression and anatomical features consistent with the perinexus in guinea pig and murine hearts. This nanodomain is wider in patients with history of AF undergoing cardiac surgery with and without MAZE procedure compared to those without a history of AF. Therefore, future studies may consider extracellular nanodomain remodeling as an important correlate of cardiac arrhythmias, and therapies designed to return these spaces to a more normal geometry may prevent arrhythmias.

REFERENCES:

1. Colilla, S., et al., *Estimates of current and future incidence and prevalence of atrial fibrillation in the U.S. adult population.* Am J Cardiol, 2013. **112**(8): p. 1142-7.

2. Grubb, N.R. and S. Furniss, *Science, medicine, and the future: Radiofrequency ablation for atrial fibrillation.* BMJ, 2001. **322**(7289): p. 777-80.
3. Andrade, J., et al., *The clinical profile and pathophysiology of atrial fibrillation: relationships among clinical features, epidemiology, and mechanisms.* Circ Res, 2014. **114**(9): p. 1453-68.
4. Lubkemeier, I., et al., *The Connexin40A96S mutation from a patient with atrial fibrillation causes decreased atrial conduction velocities and sustained episodes of induced atrial fibrillation in mice.* J Mol Cell Cardiol, 2013. **65**: p. 19-32.
5. Yan, J., et al., *c-Jun N-terminal kinase activation contributes to reduced connexin43 and development of atrial arrhythmias.* Cardiovasc Res, 2013. **97**(3): p. 589-97.
6. Dhillon, P.S., et al., *Relationship between connexin expression and gap-junction resistivity in human atrial myocardium.* Circ Arrhythm Electrophysiol, 2014. **7**(2): p. 321-9.
7. Rothe, S., et al., *Body mass index affects connexin43 remodeling in patients with atrial fibrillation.* Thorac Cardiovasc Surg, 2014. **62**(7): p. 547-53.
8. Veeraraghavan, R., et al., *Sodium channels in the Cx43 gap junction perinexus may constitute a cardiac ephapse: an experimental and modeling study.* Pflugers Archiv: European Journal of Physiology, 2015.
9. Veeraraghavan, R., et al., *Potassium channels in the Cx43 gap junction perinexus modulate ephaptic coupling: an experimental and modeling study.* Pflugers Archiv: European Journal of Physiology, 2016.
10. Veeraraghavan, R., M.E. Salama, and S. Poelzing, *Interstitial volume modulates the conduction velocity-gap junction relationship.* Am J Physiol Heart Circ Physiol, 2012. **302**(1): p. H278-86.
11. George, S.A., et al., *Extracellular Sodium Dependence of the Conduction Velocity-Calcium Relationship: Evidence of Ephaptic Self-Attenuation.* Am J Physiol Heart Circ Physiol, 2016: p. ajpheart 00857 2015.
12. George, S.A., et al., *TNFalpha Modulates Cardiac Conduction by Altering Electrical Coupling between Myocytes.* Front Physiol, 2017. **8**: p. 334.
13. George, S.A. and S. Poelzing, *Cardiac conduction in isolated hearts of genetically modified mice - Connexin43 and salts.* Prog Biophys Mol Biol, 2015.
14. Entz, M., 2nd, et al., *Heart Rate and Extracellular Sodium and Potassium Modulation of Gap Junction Mediated Conduction in Guinea Pigs.* Frontiers in Physiology, 2016. **7**: p. 16.
15. Rhett, J.M., et al., *Cx43 associates with Na(v)1.5 in the cardiomyocyte perinexus.* Journal of Membrane Biology, 2012. **245**(7): p. 411-22.
16. Veeraraghavan, R. and R. Gourdie, *Stochastic Optical Reconstruction Microscopy-based Relative Localization Analysis (STORM-RLA) for Quantitative Nanoscale Assessment of Spatial Protein Organization.* Mol Biol Cell, 2016.
17. George, S.A., et al., *Extracellular sodium and potassium levels modulate cardiac conduction in mice heterozygous null for the Connexin43 gene.* Pflugers Archiv: European Journal of Physiology, 2015.
18. Kucera, J.P., S. Rohr, and Y. Rudy, *Localization of sodium channels in intercalated disks modulates cardiac conduction.* Circ Res, 2002. **91**(12): p. 1176-82.
19. Mori, Y., G.I. Fishman, and C.S. Peskin, *Ephaptic conduction in a cardiac strand model with 3D electrodiffusion.* Proc Natl Acad Sci U S A, 2008. **105**(17): p. 6463-8.
20. Lin, J. and J.P. Keener, *Modeling electrical activity of myocardial cells incorporating the effects of ephaptic coupling.* Proc Natl Acad Sci U S A, 2010. **107**(49): p. 20935-40.
21. Hichri, E., H. Abriel, and J.P. Kucera, *Distribution of cardiac sodium channels in clusters potentiates ephaptic interactions in the intercalated disc.* J Physiol, 2018. **596**(4): p. 563-589.
22. Revel, J.P. and M.J. Karnovsky, *Hexagonal array of subunits in intercellular junctions of the mouse heart and liver.* Journal of Cell Biology, 1967. **33**(3): p. C7-C12.
23. Huttner, I., M. Boutet, and R.H. More, *Gap junctions in arterial endothelium.* Journal of Cell Biology, 1973. **57**(1): p. 247-52.

24. Cumming, G., F. Fidler, and D.L. Vaux, *Error bars in experimental biology.* J Cell Biol, 2007. **177**(1): p. 7-11.
25. Olshansky, B., et al., *Are transthoracic echocardiographic parameters associated with atrial fibrillation recurrence or stroke? Results from the Atrial Fibrillation Follow-Up Investigation of Rhythm Management (AFFIRM) study.* J Am Coll Cardiol, 2005. **45**(12): p. 2026-33.
26. Gupta, D.K., et al., *Left atrial structure and function in atrial fibrillation: ENGAGE AF-TIMI 48.* Eur Heart J, 2014. **35**(22): p. 1457-65.
27. Rhett, J.M., J. Jourdan, and R.G. Gourdie, *Connexin 43 connexon to gap junction transition is regulated by zonula occludens-1.* Mol Biol Cell, 2011. **22**(9): p. 1516-28.
28. Calhoun, J.D. and L.L. Isom, *The role of non-pore-forming beta subunits in physiology and pathophysiology of voltage-gated sodium channels.* Handb Exp Pharmacol, 2014. **221**: p. 51-89.
29. Namadurai, S., et al., *A new look at sodium channel beta subunits.* Open Biol, 2015. **5**(1): p. 140192.
30. Greer-Short, A., et al., *Revealing the Concealed Nature of Long-QT Type 3 Syndrome.* Circ Arrhythm Electrophysiol, 2017. **10**(2): p. e004400.
31. Neilan, T.G., et al., *Myocardial extracellular volume expansion and the risk of recurrent atrial fibrillation after pulmonary vein isolation.* JACC Cardiovasc Imaging, 2014. **7**(1): p. 1-11.
32. Hansen, P.R., et al., *Tumor necrosis factor-alpha increases myocardial microvascular transport in vivo.* Am J Physiol, 1994. **266**(1 Pt 2): p. H60-7.
33. Fernandez-Cobo, M., et al., *Downregulation of connexin 43 gene expression in rat heart during inflammation. The role of tumour necrosis factor.* Cytokine, 1999. **11**(3): p. 216-24.
34. Fernandez-Velasco, M., et al., *TNF-alpha downregulates transient outward potassium current in rat ventricular myocytes through iNOS overexpression and oxidant species generation.* Am J Physiol Heart Circ Physiol, 2007. **293**(1): p. H238-45.
35. Chappell, D., et al., *TNF-alpha induced shedding of the endothelial glycocalyx is prevented by hydrocortisone and antithrombin.* Basic Res Cardiol, 2009. **104**(1): p. 78-89.
36. Grandy, S.A. and C. Fiset, *Ventricular K+ currents are reduced in mice with elevated levels of serum TNFalpha.* J Mol Cell Cardiol, 2009. **47**(2): p. 238-46.
37. Guillouet, M., et al., *Tumor necrosis factor-alpha downregulates sodium current in skeletal muscle by protein kinase C activation: involvement in critical illness polyneuromyopathy.* Am J Physiol Cell Physiol, 2011. **301**(5): p. C1057-63.
38. Aguettaz, E., et al., *Stretch-activated TRPV2 channels: Role in mediating cardiopathies.* Prog Biophys Mol Biol, 2017.
39. Feinberg, W.M., et al., *Prevalence, age distribution, and gender of patients with atrial fibrillation. Analysis and implications.* Arch Intern Med, 1995. **155**(5): p. 469-73.
40. Levy, S., *Factors predisposing to the development of atrial fibrillation.* Pacing Clin Electrophysiol, 1997. **20**(10 Pt 2): p. 2670-4.
41. Kostin, S., et al., *Structural correlate of atrial fibrillation in human patients.* Cardiovasc Res, 2002. **54**(2): p. 361-79.
42. Boldt, A., et al., *Fibrosis in left atrial tissue of patients with atrial fibrillation with and without underlying mitral valve disease.* Heart, 2004. **90**(4): p. 400-5.
43. Xu, J., et al., *Atrial extracellular matrix remodeling and the maintenance of atrial fibrillation.* Circulation, 2004. **109**(3): p. 363-8.
44. Chimenti, C., et al., *Histological substrate of human atrial fibrillation.* Biomed Pharmacother, 2010. **64**(3): p. 177-83.
45. Csepe, T.A., B.J. Hansen, and V.V. Fedorov, *Atrial fibrillation driver mechanisms: Insight from the isolated human heart.* Trends Cardiovasc Med, 2017. **27**(1): p. 1-11.

FIGURES

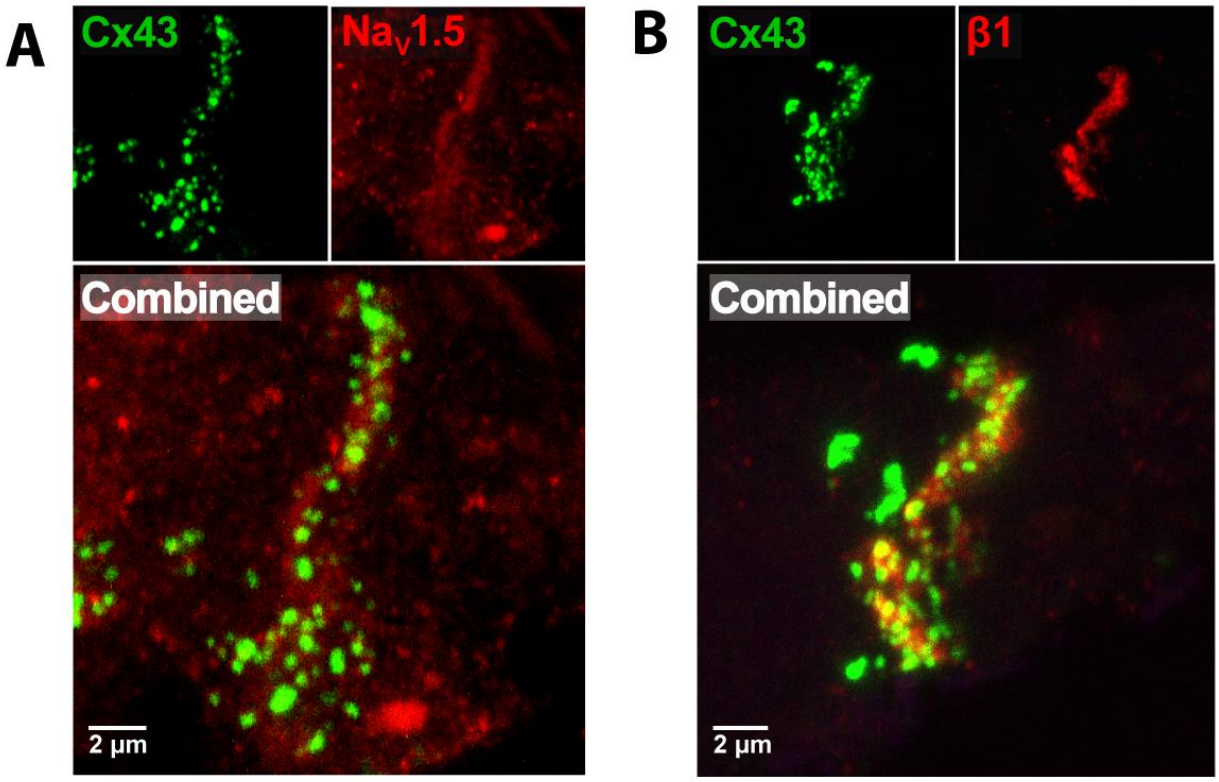

Figure 2.1 Nav1.5 and β1 enriched adjacent to connexin43 in human atria. (A) Representative immunofluorescent confocal image of a 5µm-thick section of human RAA labeled for Cx43 (green) and Nav1.5 (red), with both channels combined below. (B) Representative immunofluorescent confocal

image of a similar section of human RAA labeled for Cx43 (green) and the β1 auxiliary subunit of the cardiac sodium channel (red), with both channels combined below.

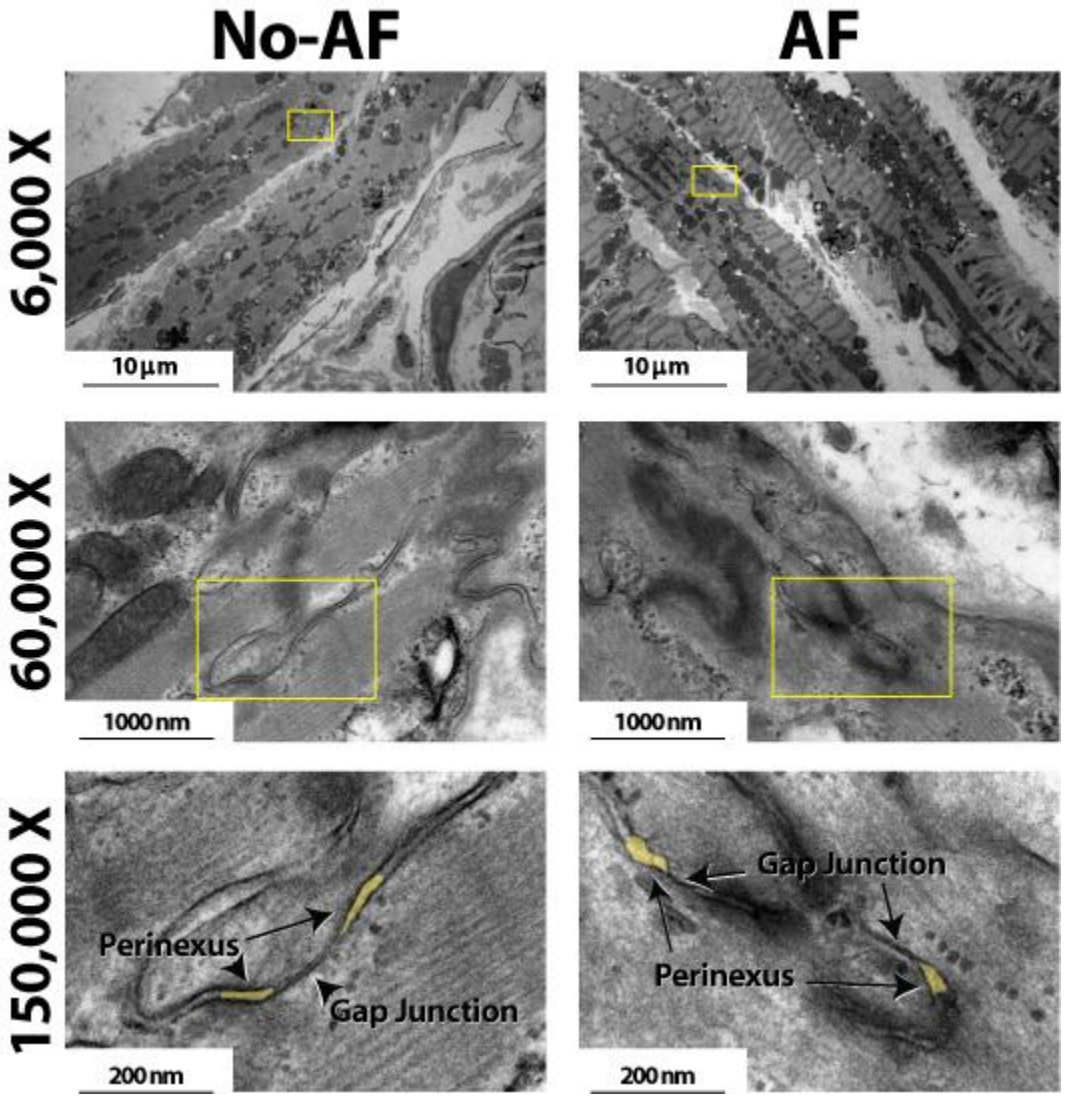

Figure 2.2. Effects of tissue fixation on tissue architecture.

Transmission electron microscopy images of human atrial myocardium at 6,000, 60,000, and 150,000 X magnification. Intercalated disc is the black ribbon-like structure in images. Perinexi highlighted in yellow.

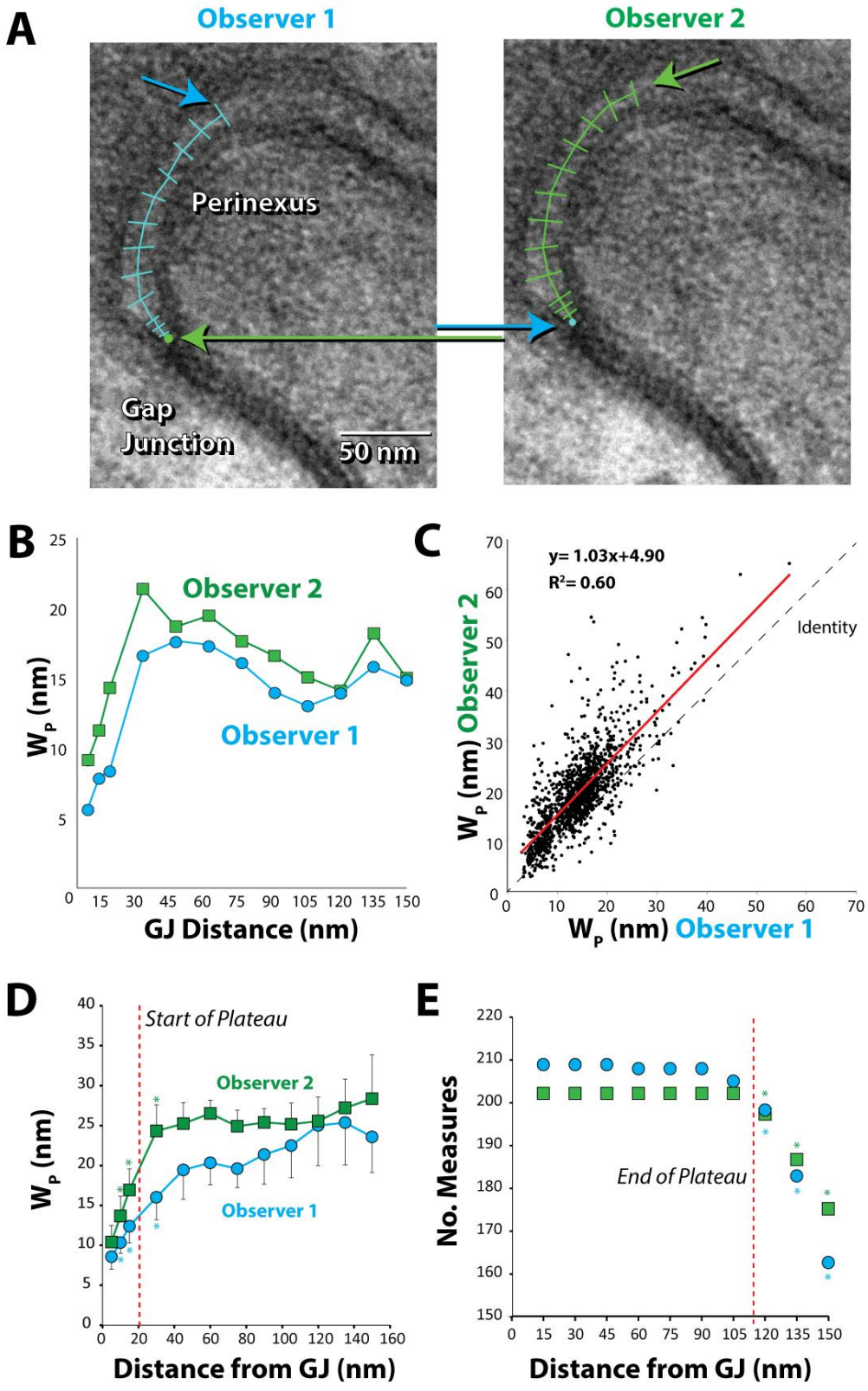

Figure 2.3. Relative, but not absolute, perinexal widths differ between observers.

(A) Representative TEM image from human left atrial appendage measured by two different observers. Arrows indicate different starting and ending points between observers. **(B)** Perinexal width (Wp) from panel A are different between observer 1 and 2. **(C)** Wp correlates between observers using data from the first 20 patients (149 images) but the y-intercept is different. **(D)** Wp changes from the gap junction edge up to 30nm (*,$p<0.05$). **(E)** Observers collect similar numbers of Wp measurements up to 105nm from gap junction edge. (*,$p<0.05$ relative to numbers at previous distance).

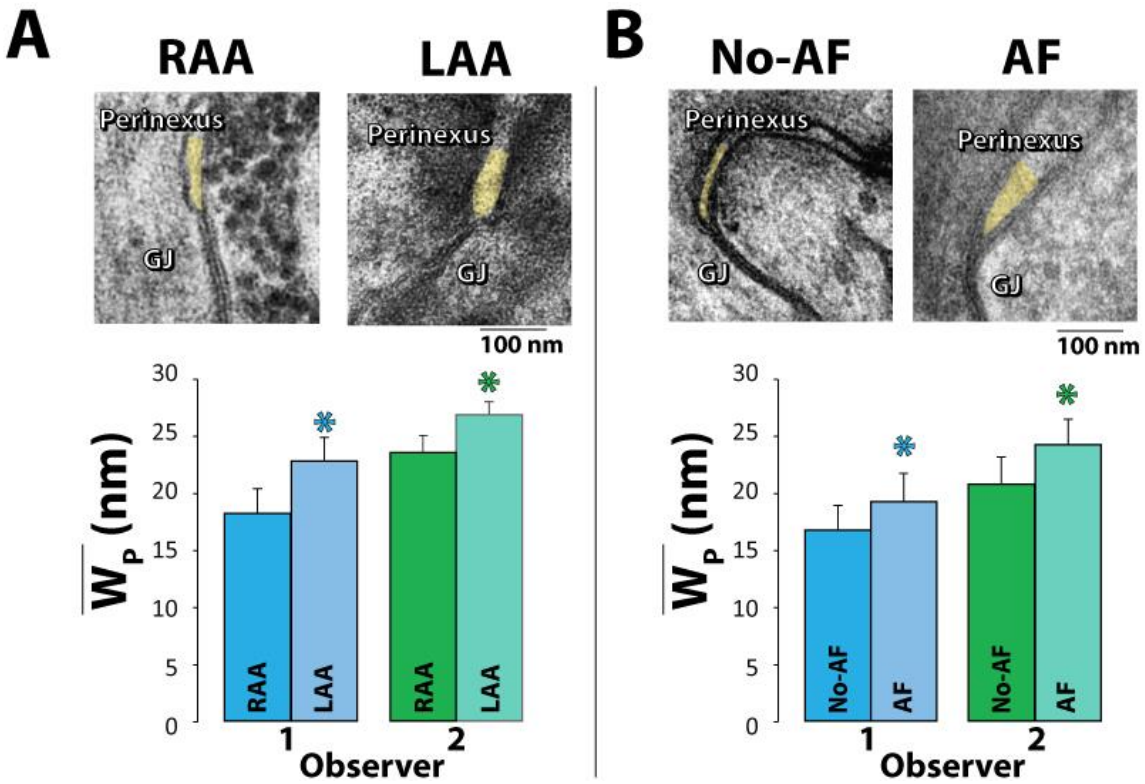

Figure 2.4. Perinexal width correlates with pre-existing atrial fibrillation.

(A) Representative TEM image from the Right (RAA, n=8) and Left (LAA, n=4) atrial appendages from the same patient (top). Wp is wider in LAA relative to RAA independent of observer (bottom). **(B)** Representative TEM images from the RAA of a patient with a history of AF (MAZE procedure, n=10) and without a history of AF (n=29) (top). All blinded observers found in 39 patients that mean Wp between 30 and 105nm is significantly larger in patients with pre-existing AF relative to those without (*,$p<0.05$, bottom).

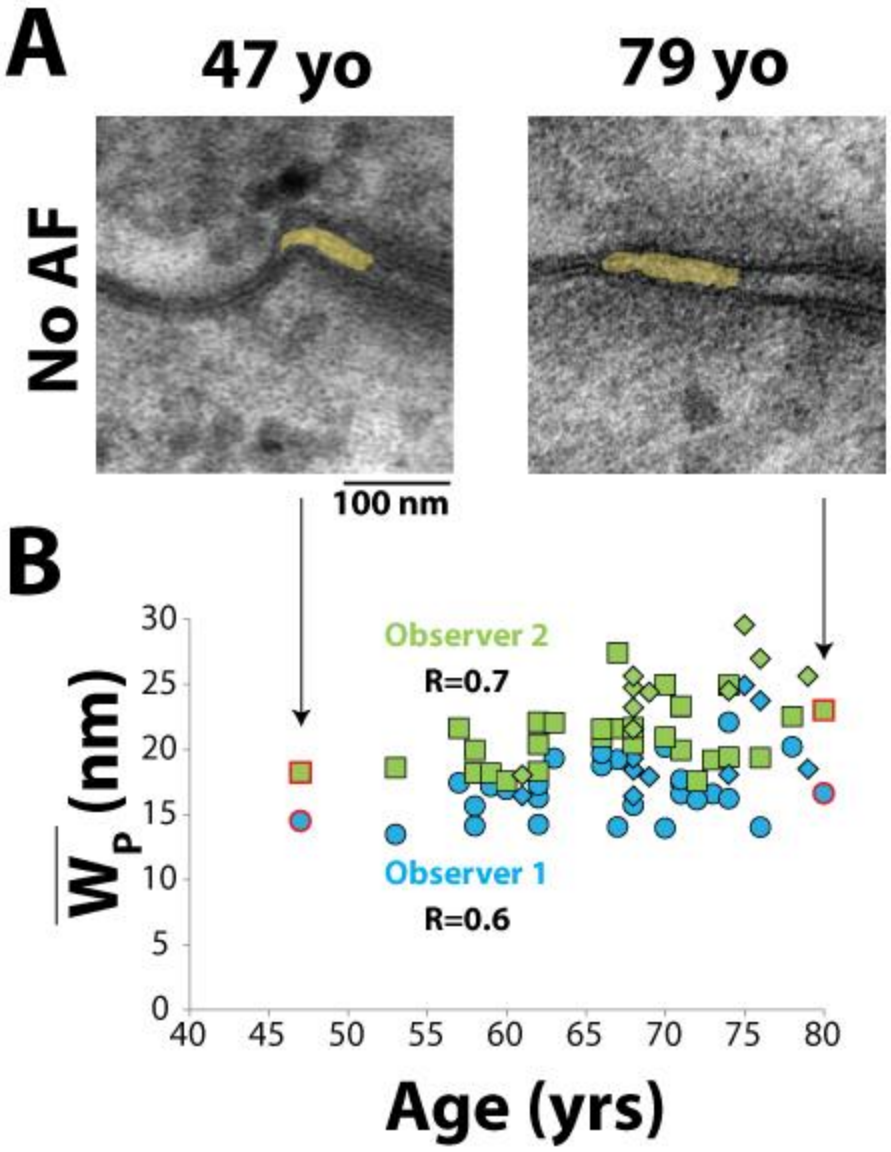

Figure 2.5. Perinexal width correlates with age

(A) Representative TEM image from two patients without a history of atrial fibrillation, ages 47 and 79 years old (yo). **(B)** All blinded observers found a correlation by Spearman's Rank correlation for all patient samples analyzed. Blue circles and green squares represent non-AF Wp values obtained by Observers 1 and 2. Blue and green diamonds represent AF Wp values obtained by Observers 1 and 2, respectively.

TABLES

	No AF (n=19)	Prior AF (n=10)	New AF (n=10)
Patient Characteristics:			

Mean Age (years)	65	70	69
Hypertension	16 (84%)	9 (90%)	9 (90%)
Diabetes mellitus	5 (26%)	1 (10%)	2 (20%)
Peripheral vascular disease	4 (21%)	0	1 (10%)
LVEF ≤ 45%	3 (16%)	2 (20%)	0
Chronic kidney disease (GFR < 60*)	4 (21%)	4 (40%)	5 (50%)
Current Medications:			
Beta blocker	13 (68%)	6 (60%)	7 (70%)
ACEi/ARB	10 (53%)	6 (60%)	6 (60%)
Statin	16 (84%)	4 (40%)	10 (100%)
Surgical Procedure:			
Coronary artery bypass	15 (79%)	2 (20%)	7 (70%)
Valve procedure	7 (37%)	9 (90%)	6 (60%)
MAZE procedure	0	10 (100%)	0

Table 2.1 Patient and procedure characteristics

ACEi = angiotensin converting enzyme inhibitor; **AF**= atrial fibrillation; **ARB** = angiotensin receptor blocker; **GFR**= glomerular filtration rate; **LVEF** = left ventricular ejection fraction

*mL/min/1.73m^2

Procedure	Normal	Mild	Moderate	Severe	***Row Totals***
AF	1	1	4	4	10*
No AF	18	7	3	1	29
Column Totals	19	8	7	5	**39**

Table 2.2 Left atrial size and history of AF

Left atrial dilatation is greater in patient with history of AF relative to patients with no history of AF. * $p<0.05$ by chi-squared analysis.

	Perinexal Width, Wp (nm)					
	RAA-AF (n=8)	LAA-AF (n=4)	No-AF (n=29)	AF (n=12)	No POAF (n=19)	POAF (n=10)
Observer						
1	18.0 ± 1.2	22.6 ± 2.1*	16.9 ± 2.1	19.5 ± 2.5*	16.5 ± 2.2	17.4 ± 2.3
2	23.3 ± 1.5	26.7 ± 2.1*	20.7 ± 2.4	24.4 ± 2.2*	20.8 ± 2.5	20.7 ± 2.4

Table 2.3 Summary data of perinexal width

Left Atrial Appendages (LAA), Right Atrial Appendages (RAA), Postoperative Atrial Fibrillation (POAF), Pre-existing AF (AF). Statistical significance * for $p<0.05$ for individual observers determined by Student's t-test.

APPENDIX: SUPPLEMENTAL DATA

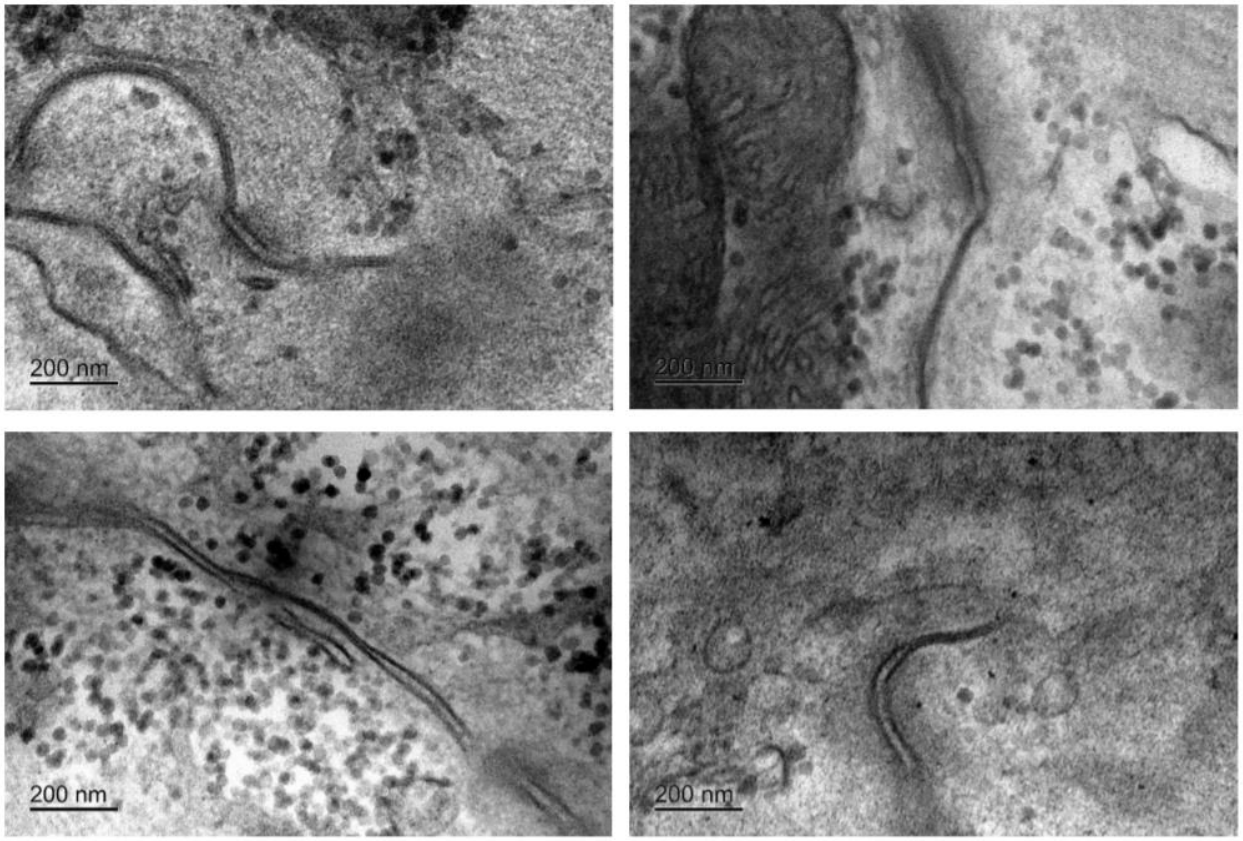

Figure 2.S.1 Representative TEM images of gap junctions and perinexi from 4 non-AF patients.

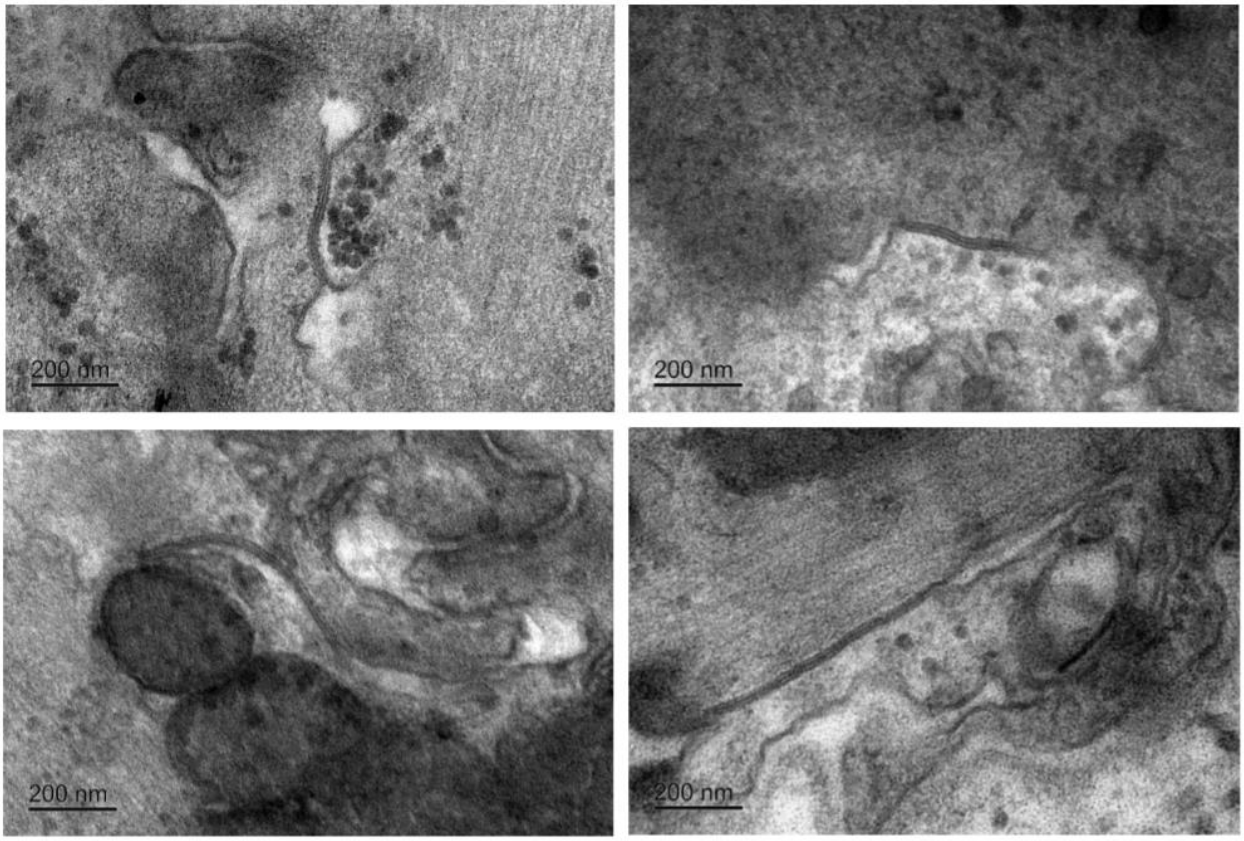

Figure 2.S.2 Representative TEM images of gap junctions and perinexi from 4 AF patients.

CHAPTER 3: QUANTIFYING INTERMEMBERANE DISTANCES WITH SERIAL IMAGE DILATIONS

FOREWORD

Over the course of the study described in Chapter 2, it became evident that our current manual segmentation technique for measuring the perinexus, while entirely valid, had some key limitations. First, it was slow, requiring approximately 5-10 minutes per image. Second, with only 12 total measurements over a 150nm span, this method is prone to under-sampling, as the perinexus is a dynamic and complex region. Before beginning the undertaking that is analyzing 600 perinexal images, I first needed to be confident that I could accomplish that task as efficiently as possible with the highest possible confidence in my data. The manuscript for the resulting program was published in the Journal of Visualized Experiments, with an accompanying video interview. As such, the next chapter will read as much like a how-to as a validation of the method. The reader is encouraged to watch the video interview on the JoVE website for a better understanding of the perinexus, the measurement technique, and why I have made little headway in becoming an internet video sensation.

INTRODUCTION

The following algorithm was developed to measure the intermembrane distance between two structurally coupled cardiomyocytes at the point they separate from each other at the edge of a gap junction plaque in a nanodomain called the perinexus,[1] which has been implicated in ephaptic coupling [2-5]. In the process of analyzing hundreds of transmission electron microscopy (TEM) images of perinexi using a manual segmentation method in a previous study [6],the need was identified for a higher-throughput method that sampled perinexal width in higher spatial resolution while preserving the accuracy of the previous manual segmentation process During manual segmentation, lines are drawn at 15 nm intervals, approximately orthogonal to the centerline, in order to measure perinexal width. The new algorithm takes a one pixel thick binary outline of two parallel lines and uses serial image dilations to count the number of pixels between the two membranes. While image dilations have commonly been used in a myriad of image processing applications, including contour or edge detection [7, 8], this algorithm uses dilations as a counting mechanism. The centerline is then isolated using a pathfinding algorithm [9] and perinexal width is then measured at a resolution along the length of perinexus equal to the resolution of the image. The difference in resolution in this case is 1 measurement per 15 nm for manual segmentation and 1 measurement per 0.34 nm with the new algorithm, a 44-fold increase in spatial sampling frequency. Furthermore, this increased sampling frequency is accomplished in approximately $1/5^{th}$ the time needed for manual segmentation.

This algorithm will be used in its current form to measure perinexal width at the conventional 0-150 nm from the edge of a gap junction plaque [5] (GJ) as well as within a specified region of interest, where the perinexus plateaus between 30 and 105 nm [2, 3, 10]. The increased sampling frequency reduces the variability in individual perinexus measurements compared to manual segmentation and significantly shortens analysis time, allowing for efficient processing of large data sets. However, this program is not limited to nanoscale TEM images of cardiac intercalated discs. The same approach could be used to quantify vascular diameter, ventricular ejection fraction, or even non-biological phenomena such as river

erosion or flooding. This algorithm is appropriate for quantifying the distance between any two quasi-parallel edges.

PROTOCOL

Note: Software required are ImageJ (or similar image-modifying software) and Matlab R2015. The user may encounter compatibility issues with other versions of Matlab.

1. Pre-Processing Images

1.1. For any grayscale image, ensure the maximum intensity value of any given pixel is <255.

Note: This is typically done by subtracting a value of 1 from the image in the custom Matlab program ImageSub.m, included in supplemental file S1.

2. Outline the perinexus in ImageJ or other image-processing software.

Note: The outline should be one pixel thick and set to the highest intensity value in an image (255 in a grayscale image from 0 to 255). The GJ can be identified by its pentalaminar structure [11, 12] and the beginning of the perinexus is defined as the point at which the two opposing cell membrane bilayers diverge, as shown in Figure 1A. Begin ~200 nm from the edge of the GJ, tracing along the inner membrane of the first cell and back along the inner membrane of the second cell. In ImageJ, releasing the pen will automatically close the outline. This artificial closing will be cropped out later.

Note: It is crucial to outline the perinexus with great care at as high a magnification as possible, as even small mis-applications of the outline can result in several nanometers of error in the final measurement.

3. Setup Algorithm and Select Perinexus of Interest

Note: The pathfinding algorithm requires the AutoGraph, Edge, Graph, Node , and Pathfinding functions [9] to be in the same directory as the MembraneSepDist m-file. All files can be found in supplemental file S1.

3.1. Select save locations for data and figures. These are currently hard-coded into the m-file.

Note: The first line of the program is a function to clear all variables, close all windows and clear the command window. Save any desired variables or figures before running the m-file.

Note: Software screenshots are included in supplemental file S2 for all hard-coded values.

3.2. Run the program MembraneSepDist.m

3.3. Set Parameters.

Note: A GUI will pop up with default parameters for the gradient threshold, scale, region of interest, and manual start. The default values can be changed in the m-file, or they can be changed for each individual image.

3.3.1. Set spatial derivative gradient threshold.

Note: Higher values result in more points selected in centerline isolation. Values that are too high or too low (outside of a range of approximately 3.0-7.9) may result in computational inefficiency or an imprecise selection of centerline points yielding imprecise centerline isolation (See Figure 2A-C).

3.3.2. Set scale in pixels/scale units.

3.3.3. Set the spatial lower and upper limits for the region of interest.

Note: By our laboratory's convention, the defined region of interest is between 30 and 105 nm from the edge of the GJ [2, 3, 10].

3.3.4. Set automatic/manual start. In the majority of cases, the algorithm accurately detects the starting point where the gap junction ends and perinexus begins. However, in some cases of irregularly-shaped perinexi, the user must identify the start point manually. Set this value to 0 for automatic, 1 for manual.

3.4. Select desired image.

Note: The file select folder can be changed in the m-file.

3.5. Crop the image to select the perinexus of interest. When the image comes up, the cursor will

automatically change to a crosshair. Crop the image by dragging a box around the perinexus of interest (See figure 3). The crop box can be adjusted by using the squares on the corners and sides to make it larger or smaller. When cropping, ensure the "open" end of the perinexus (furthest from the GJ, see Figure 3) is cropped so that the two membrane outlines reach the edge of the cropped image.

Note: It is recommended the user make the image full-screen to more easily see the perinexus of interest and crop appropriately.

3.6. Select the final crop by double-clicking with the curser in between the opposing edges to be measured.

Note: It is critical that the double-click be performed inside the perinexus. If the program fails to identify a centerline, restart the program and make sure the click occurs within the perinexus.

3.7. The final centerline after all dilations and erosions will pop up for a final user evaluation of the program's efficacy.

Note: A dialog box will appear on the screen while the program is running to inform the user that Matlab will be unable to process any additional commands until the program has finished. How long this process takes depends on array (image) size and computer processing power.

3.8. If manual start point is enabled, an image of the centerline will pop up over the original anatomical image, along with a cross-hair cursor (see Figure 2E). Select a point *outside* of the perinexus near the desired start point.

Note: The program will find the centerline point closest to the selected pixel and use that as the start point.

3.9. Record Data.

Note: Once the program has finished, the program will return a mapped centerline, plot of perinexal width as a function of distance from the edge of the GJ. Additionally, the program will return the average perinexal width up to 150 nm from the edge of the GJ as well as the average from within the defined region of interest at the Matlab command line. W_p *values and distances from the GJ are stored in the variable "WpList" or the user can manually record them separately.*

4. Algorithm Troubleshooting

4.1. If the centerline is not properly identified (Figure 2A), open the figure "Gmag" and use the Index to identify an appropriate gradient threshold (Figure 2C).

4.2. If the start point is not properly identified, set the start point manually (See Protocol 3.8).

REPRESENTATIVE RESULTS

STATISTICAL METHODS

Comparisons were made between experimental groups using Student's t-tests. A p-value < 0.05 is considered significant and all values are represented as mean ± standard deviation.

MANUAL SEGMENTATION

The quantification of the GJ-adjacent perinexus nanodomain width (W_p) is typically accomplished by manual segmentation. This manual segmentation process is demonstrated in Figure 1A and described previously [6]. The observer identifies the edge of the GJ (Figure 1, red dot), measures 5nm along the center of the perinexus, and measures the distance between the membranes at that point. The process is then repeated at 10, 15, 30, and every 15 nm up to 150 nm. This technique, while effective, has limitations of time and spatial under-sampling along the length of the perinexus.

Mean W_p measurements from previous studies can vary from approximately 10 to 20nm [2, 3, 10], and 3nm appears to be the mean difference needed to detect statistical significance, which is well above the spatial Nyquist frequency of 0.7 nm per measurement based an interpixel resolution of 0.34 nm. Therefore, while manual segmentation is time consuming, the method is sufficient to measure differences in W_p associated with an intervention or disease state.

SERIAL IMAGE DILATIONS

In order to measure the perinexus in a faster, reproducible manner with appropriate spatial resolution, we developed a program based on serial image dilations to count the pixels between two manually-traced membranes, which can be seen in Figure 1B.

The serial dilation process is illustrated in Figure 4. As the binary image is dilated (Figure 4, A-D), that dilation is then inverted and added to a working image – the non-binary form of the original outline (Figure 4, E-H). The process is repeated until the outline is entirely filled in (Figure 4D). At this point, the final working image (Figure 4H) is a count of the number of times a particular pixel has remained un-dilated. As such, the values near the outline of the cell membranes are very low, while the values at the center are highest. By counting the number of dilations to fill the area at each point, the distance between the membrane edges can be calculated. The next challenge is to identify and isolate the centerline in order to quantify perinexal width as a function of distance from the GJ, which is done by first applying a spatial derivative to the final working image (Figure 2-last image, and Figure 5A). A second example of a more irregularly-shaped perinexus can be found in supplemental file S.3.3.

CENTERLINE IDENTIFICATION

The gradient of the final working image can be quantified by a spatial derivative, as dilation count values from edge to edge change from high to low to high again (Figure 5A left to right). Considering only the magnitude of the spatial derivative (Figure 5B), the outline and centerline, highlighted with white arrows, are immediately identifiable as areas of discontinuity. At these locations, the gradient direction changes from increasing to decreasing or vice versa. Applying a threshold (Figure 5C) produces a binary image of the centerline and outline, and subtracting the original outline yields the isolated centerline (Figure 5D). While this method of isolating the centerline is computationally efficient, the threshold applied to the spatial derivative creates gaps in the resulting centerline. These gaps (Figure 5D, insert) must be filled to provide an accurate measurement of the distance from the GJ and to ensure the perinexus is measured in its entirety. First, the centerline is dilated to fill in any gaps (Figure 5E), followed by an erosion (Figure 5F) and a

"bwmorph" function (operation = 'skel', n = inf) to eliminate as many points as possible while leaving a continuous centerline, thereby increasing the computational efficiency of a subsequent pathfinding algorithm developed by Wasit Limprasert and available on MATLAB Central [9]. This dilation-erosion function produces the completed centerline, which is combined with the final working image (Figure 5G). However, this centerline is often more than one pixel thick and therefore is not a precise isolation of the centerline.

The Wasit Limprasert pathfinding algorithm is used to determine the perinexus centerline. The pathfinding algorithm is able to track the highest values – in this case the values closest to the center which remained un-dilated through the most iterations along the centerline (Figure 5G, insert). The result is an automatic trace of the centerline, as shown in Figure 6. By isolating the centerline, perinexal width can be presented as a function of distance from the end of the GJ, as shown in Figure 6B (top), or as the average width of a specified region of interest.

KERNEL ANALYSIS

It is important to note that digitized images are based on square arrays and dilation kernels are likewise based on square matrices. This means that dilation distance across a diagonal is greater than orthogonal. Therefore, we next sought to determine whether the kernel affected the results of the algorithm. In order to quantify kernel-specific variability, five different kernel shapes were analyzed: "*Plus*" (the shape used in the above analyses), "*X*", "*Box*", and "*Line*", as described in Figure 7A. The kernel is applied at each non-zero point of a binary image. The star in each kernel of Figure 7A represents the center, where white is a value of 1, and black is a value of 0 for the dilation kernel.

Each kernel's influence on the mean W_p measurement of a single approximately horizontal perinexal image (Figure 7B, top), quantified by an experienced user, was determined by rotating the image with Matlab's "imrotate" command and computing W_p in steps of 10°. The W_p measurement values (Figure 7B, bottom)

fluctuate with image orientation in a rectified sinusoidal fashion with a *Plus* shaped kernel. The lowest values occur when a relatively straight perinexus is oriented vertically or horizontally. Neither the *X*, *Box*, nor *Line* kernels provided any advantage over the plus-shaped kernel. The *X* and *Box* kernels produced identical results, but the values of mean W_p were out of phase with the *Plus* kernel by 45°. The *Line* kernel failed to fully dilate the image at certain angles as can be seen by the absence of data in the green trace for images rotated less than 30 or more than 145°. Thus, the orthogonal *Plus* dilation kernel overestimated membrane separation when dilating a perinexus with an axis oriented diagonally for example at approximately 45°, and the *X* and *Box* kernels underestimated mean W_p when the long axis of the perinexus was also at 45°. Based on this analysis, we developed a correction factor applied to the values generated from dilating with the plus-shaped kernel. To account for the overestimation of membrane separation associated with image orientation, this correction factor multiplied by the measured width value depending on the orientation of the image (Equation 1).

If $\theta < 45°$

$$W_{p\ corrected} = cosd(\theta) * W_{p\ measured}$$

If $\theta \geq 45°$

$$W_{p\ corrected} = cosd(\theta) * W_{p\ measured} \qquad \text{(Equation 1)}$$

In this equation, W_p measured is the original W_p value generated by the above algorithm and θ is the calculated angle from horizontal, in degrees. θ is calculated by taking the inverse tangent of the total change in the horizontal direction divided by the total change in the vertical direction of the perinexal centerline. The above correction approximates the average angle, relative to horizontal, of the perinexus (Figure 8A, left-top) and results in a measurement as if obtained from a horizontal perinexus (Figure 8A, left-bottom). The rationale behind this equation comes from the fact that the plus-shaped kernel (Figure 7A) is essentially two line-shaped kernels arranged orthogonally to each other. As such, below 45° (closer to horizontal), the dilations occur vertically and therefore multiplying by the cosine of the angle gives the correct

measurement. Conversely, for angles above 45° (closer to vertical), dilations occur horizontally and the sine is used to determine the correct measurement. At precisely 45°, the sine and cosine are equal. Supplemental file S.3.4 provides a depiction of this concept. Note that this correction is based on the average angle and caution should be used when analyzing substantially non-linear shapes. This process was repeated on 20 randomly-selected perinexi and the corrected measurements correlated strongly with measurements obtained by manually rotating and re-analyzing the images (Figure 8A, right). To confirm the accurate correction for image orientation, two sets of phantom edges were generated (Figure 8B, left) and rotated 180°. With the trigonometric correction, the algorithm accurately returned the correct value at each orientation, regardless of spatial resolution or image size (Figure 8B, right).

ANALYTICAL APPLICATION AND REPRODUCABILITY WITH ORIENTATION CORRECTION

Recalling that previous studies using manual segmentation report statistically significant mean W_p differences greater than or equal to 3 nm, it was important to determine whether to the algorithm could be used to recapitulate previous findings using a complete dataset. Using the new algorithm, two observers – one experienced and one unexperienced with perinexal analysis (Obs. 1 and Obs.2, respectively) – analyzed the same images from a previous study [6] that included 12 patients who were diagnosed with atrial fibrillation (AF) prior to tissue collection and 29 patients that did not have pre-existing AF (No-AF). The experienced user found that W_p was significantly wider in patients with AF than without AF (21.9±2.5 and 18.4±2.0 nm, respectively, Figure 9A). These values with the correction factor applied are similar to those reported previously (24.4±2.2 nm and 20.7±2.4 nm, respectively) [6]. Importantly, the inexperienced user found the same significant difference (22.1±2.8 nm and 20.1±2.6 nm, respectively) between disease states with the automated program. Additionally, the standard deviation of the W_p values did not change with the correction factor, indicating the standard deviation of 2-3nm is not an artifact of the algorithm but of the structure itself and tissue processing. These results demonstrate that the proposed automated method is capable of recapitulating the results of previous studies.

Importantly, the perinexus is a recently-defined structure and no consensus has been reached on the range of absolute values of membrane separation adjacent to the GJ [2, 3]. Since outer-membrane-to-outer-membrane GJ width has been previously estimated at 20nm [13], we sought to determine the algorithms efficacy by also measuring GJ width. Both observers found no significant difference between gap junction widths (GJW) of patients with or without pre-existing AF (Figure 9B). Absolute GJW values for AF and non-AF patients were 20.5 ± 2.5 nm and 20.3 ± 1.9 nm respectively for the experienced observer and 21.0 ± 3.1 nm and 20.0 ± 2.2 nm for the inexperienced observer, similar to what has been reported previously.

To determine whether the automated algorithm required less time to analyze data than manual segmentation, both the experienced and inexperienced user recorded the time needed to quantify a 10-image training set (Supplemental File S5). Table 1 demonstrates that the experienced and inexperienced user decreased analysis time by 4.7- and 8.3-fold respectively using the automated algorithm relative to the manual segmentation approach, with an approximately 43-fold increase in spatial resolution along the perinexus.

ALGORITHM TROUBLESHOOTING

The most common error when running the algorithm occurs when the final centerline does not end at the edge of the image. In such cases, not enough points were selected from the spatial derivative map, causing the program to fail and produce an error message advising the user to select a larger crop area or increase the spatial derivative threshold. Drawing a larger crop box will improve the reliability of the program in some cases as the spatial derivative changes drastically near the edges of the figure, which can disrupt the pathfinding or edge detection algorithms.

It is also possible for the pathfinding algorithm to fail to properly identify the centerline, even if the centerline reaches the edge of the image, particularly if the gradient threshold is too low (Figure 2A). If the gradient threshold is set too high, there will be more unnecessary points incorporated into the pathfinding algorithm (Figure 2B), decreasing computational efficiency. If the user is unable to determine

an appropriate threshold, the image array "*GMag"* (Figure 2C), which is generated by the program and can be found in the Workspace, can help the user determine the threshold. Find points along the centerline and set the threshold slightly above their Index value to ensure these points are selected. In the given example, an appropriate threshold would be above ~5.1 (Figure 2C, insert).

The start point may also fail to reach the beginning of the perinexus (Figure 2D). In this case, re-run the program and set the *Manual Start* value to 1. After the centerline has been isolated, the user selects a point outside the perinexus and the centerline point closest to the selected pixel (Figure 2E, red square) will be set as the start point. The result is the full centerline (Figure 2F).

DISCUSSION

The algorithm uses serial image dilations to count the number of pixels between two opposing 2D edges in a binary image, which in this case is the inter-membrane separation of the perinexus [2, 3, 14]. A spatial derivative and a pathfinding algorithm are then used to isolate the centerline, followed by a secondary dilation and erosion sequence to fill gaps in the centerline, similar to what has been done before [15]. The centerline is then combined with the final dilation-count image to represent perinexal width as a function of distance from the beginning of edge separation, in this case the end of the GJ and the beginning of the perinexus [16].

Four primary parameters are user-defined in a GUI at the start of the program:

1. Gradient threshold
2. Scale
3. Region of interest range
4. Start point selection method (automatic or manual)

The most common mechanism of failure for the algorithm is the failure of the centerline to reach the edge of the image, which is how the endpoint is determined for the pathfinding algorithm. In order to fix such an issue, the user can increase the gradient threshold described in step 3.3.1, which will cause the program to select more points out of the spatial derivative image, which will increase the computation time required by the pathfinding algorithm. Therefore, this algorithm requires a compromise between computation speed and centerline integrity. It is important to note that so long as all the points of the centerline are identified from the spatial derivative, along with an appropriate start point, the spatial derivative threshold will have no effect on the edge separation measurement.

Image orientation appears to affect dilation values, because the kernel dilates in 90 degree steps, which can introduce an error if the majority of the region of interest is at an angle 45° to the axes of dilation matrices. Therefore, the dilation count may not always be an accurate representation of the space between the edges. This limitation has been addressed by a trigonometric correction factor, but could potentially be ignored if all images in a dataset are aligned at the same orientation. Furthermore, caution should be used in interpreting results as it is possible that section planes are not perfectly perpendicular to the two membranes. In Figure 9B, we use GJW to suggest that our perinexus images were in-plane. Still, it is imperative that sample sizes be sufficiently large to account for any sectioning variations between images. Additionally, our perinexal width measurements should not be interpreted to reflect in-vivo spaces, but this approach is used to measure mean differences in perinexal width relative to some intervention or disease state.

The current algorithm also requires a manually-traced outline of the edges as an input. It is important to note that so long as the scale is set correctly, spatial resolution has no effect on the algorithm's measurements as demonstrated by the varying resolutions of images in Figure 6 and an additional low-resolution image in supplemental file S.3.6. The next step in improving the algorithm is removing human intervention from outline generation along with a tool that can select the area of interest. These features would likely enhance the precision of the measurement and reduce user bias.

This computationally efficient algorithm provides a faster method, requiring approximately one fifth the man-hours, of quantifying the perinexus with no detectable penalty to reproducibility when compared to the manual segmentation process. Additionally, the manual segmentation process utilizes one measurement every 15 nanometers to quantify perinexal width, which can lead to under sampling as the membrane separation of the perinexus can change substantially within that 15nm range. In contrast, the automated program has a spatial resolution equal to that of the imaging modality, in this case 2.9 pixels per nanometer along the length of the perinexus, therefore delivering a more finely resolved average of perinexal width.

While the applications in the field of cardiac structural biology are promising and exciting, this algorithm's uses are not confined to TEM images. Any field requiring a precise, high-resolution measurement of two quasi-parallel 2D edges can make use of this algorithm. The algorithm could be used to track anything from riverbank erosion and flood patterns from satellite images to vascular development with brightfield or fluorescent microscopy. One of the most promising potential applications is in the field of cardiology and measuring ventricular ejection fraction (EF) with point-of-care cardiac echocardiography. Currently, the standard technique is the biplane method of disks [17], though a newer algorithm, AutoEF, is currently the cutting edge EF-quantifying method [18, 19]. For biplane method of disks, the chamber in question is manually traced and quantified using a modified Simpson's method, whereby overall volume is automatically calculated by the summation of stacked elliptical disks. The main limitation with this method is that it can only return the total cross-sectional area of the desired chamber, with no resolution to identify specific regions of interest, and also requires substantial human input and expertise. The newer method, AutoEF, identifies and outlines the edge of the ventricle using a 2D speckling algorithm and then computes the ventricular cross-sectional area. This process, while precise and efficient for measuring gross ventricular area, also has a similar inherent limitation of only measuring total cross-sectional area. This primary drawback limits clinicians' diagnostic and treatment abilities. In contrast, the algorithm presented in this manuscript can identify a midline and has a resolution equal to the resolution of the imaging modality

to pinpoint specific regions of interest. This is important because ultrasound scanners with micrometer spatial resolution are commercially available [20, 21], implying that this algorithm could detect localized wall motion abnormalities at the resolution of micrometers instead of centimeters. While this application needs to be experimentally validated, it is one of the most immediately promising applications of this algorithm. In fact, it could easily be combined with the speckle tracking capabilities of AutoEF or the manual traces utilized in manual planimetry to provide higher-resolution information in parallel with conventional EF data.

As versatile and applicable as the current algorithm is, it was developed for 2D images. However, as imaging technologies continue to improve, there is an increasing demand for 3 and 4D quantification technologies. Therefore, the next iteration of the algorithm is to adapt the same approach, serially dilating a binary image, to a 3-dimensional object, where automatically defining a centerline is currently beyond the capabilities of current imaging programs. Such an algorithm would have wide applications both clinically and experimentally in the cardiac field alone, including 3D cardiac echocardiograms [22, 23], 3D electron microscopy [24-26], and 3D magnetic resonance imaging [27-29].

REFERENCES

1. Rhett, J.M. and R.G. Gourdie, *The perinexus: a new feature of Cx43 gap junction organization.* Heart Rhythm, 2012. **9**(4): p. 619-23.
2. Veeraraghavan, R., et al., *Sodium channels in the Cx43 gap junction perinexus may constitute a cardiac ephapse: an experimental and modeling study.* Pflugers Archiv: European Journal of Physiology, 2015.
3. George, S.A., et al., *Extracellular sodium dependence of the conduction velocity-calcium relationship: evidence of ephaptic self-attenuation.* American Journal of Physiology - Heart and Circulatory Physiology, 2016. **310**(9): p. H1129-39.
4. Veeraraghavan, R., et al., *Potassium channels in the Cx43 gap junction perinexus modulate ephaptic coupling: an experimental and modeling study.* Pflugers Archiv: European Journal of Physiology, 2016.
5. Rhett, J.M., et al., *Cx43 associates with Na(v)1.5 in the cardiomyocyte perinexus.* Journal of Membrane Biology, 2012. **245**(7): p. 411-22.
6. Raisch, T.B., et al., *Intercalated Disc Extracellular Nanodomain Expansion in Patients with Atrial Fibrillation.* Frontiers in Physiology, 2018.

7. Yan, J., et al., *Novel methods of automated quantification of gap junction distribution and interstitial collagen quantity from animal and human atrial tissue sections.* PLoS One, 2014. **9**(8): p. e104357.
8. Papari, G. and N. Petkov, *Adaptive pseudo dilation for gestalt edge grouping and contour detection.* IEEE Transactions on Image Processing, 2008. **17**(10): p. 1950-62.
9. Limprasert, W. *PathFinding.* 2012; Available from: https://www.mathworks.com/matlabcentral/fileexchange/34966-pathfinding.
10. George, S.A., et al., *Extracellular sodium and potassium levels modulate cardiac conduction in mice heterozygous null for the Connexin43 gene.* Pflugers Archiv: European Journal of Physiology, 2015.
11. Revel, J.P. and M.J. Karnovsky, *Hexagonal array of subunits in intercellular junctions of the mouse heart and liver.* Journal of Cell Biology, 1967. **33**(3): p. C7-C12.
12. Huttner, I., M. Boutet, and R.H. More, *Gap junctions in arterial endothelium.* Journal of Cell Biology, 1973. **57**(1): p. 247-52.
13. Makowski, L., et al., *Gap junction structures. II. Analysis of the x-ray diffraction data.* Journal of Cell Biology, 1977. **74**(2): p. 629-45.
14. Entz, M., 2nd, et al., *Heart Rate and Extracellular Sodium and Potassium Modulation of Gap Junction Mediated Conduction in Guinea Pigs.* Frontiers in Physiology, 2016. **7**: p. 16.
15. Sild, M., R.P. Chatelain, and E.S. Ruthazer, *Improved method for the quantification of motility in glia and other morphologically complex cells.* Neural Plasticity, 2013. **2013**: p. 853727.
16. Rhett, J.M., et al., *The perinexus: Sign-post on the path to a new model of cardiac conduction?* Trends in Cardiovascular Medicine, 2013.
17. Lang, R.M., et al., *Recommendations for cardiac chamber quantification by echocardiography in adults: an update from the American Society of Echocardiography and the European Association of Cardiovascular Imaging.* Journal of the American Society of Echocardiography, 2015. **28**(1): p. 1-39 e14.
18. Kawai, J., et al., *[Left ventricular volume and ejection fraction by the axius auto ejection fraction method: comparison with manual trace method and visual assessment of ejection fraction]*. Journal of Cardiology, 2007. **49**(3): p. 125-34.
19. Frederiksen, C.A., et al., *Clinical utility of semi-automated estimation of ejection fraction at the point-of-care.* Heart, Lung and Vessels, 2015. **7**(3): p. 208-16.
20. Foster, F.S., et al., *A new ultrasound instrument for in vivo microimaging of mice.* Ultrasound in Medicine and Biology, 2002. **28**(9): p. 1165-72.
21. Moran, C.M., et al., *A comparison of the imaging performance of high resolution ultrasound scanners for preclinical imaging.* Ultrasound in Medicine and Biology, 2011. **37**(3): p. 493-501.
22. Papademetris, X., et al., *Estimation of 3D left ventricular deformation from echocardiography.* Medical Image Analysis, 2001. **5**(1): p. 17-28.
23. Hosny, A., et al., *Unlocking vendor-specific tags: Three-dimensional printing of echocardiographic data sets.* Journal of Thoracic Cardiovascular Surgery, 2018. **155**(1): p. 143-145 e1.
24. Cretoiu, D., et al., *Human cardiac telocytes: 3D imaging by FIB-SEM tomography.* Journal of Cellular and Molecular Medicine, 2014. **18**(11): p. 2157-64.
25. Risi, C., et al., *Ca(2+)-induced movement of tropomyosin on native cardiac thin filaments revealed by cryoelectron microscopy.* Proceedings of the National Academy of Sciences U S A, 2017. **114**(26): p. 6782-6787.
26. Dhindwal, S., et al., *A cryo-EM-based model of phosphorylation- and FKBP12.6-mediated allosterism of the cardiac ryanodine receptor.* Science Signaling, 2017. **10**(480).
27. Reddy, V.Y., et al., *Integration of cardiac magnetic resonance imaging with three-dimensional electroanatomic mapping to guide left ventricular catheter manipulation: feasibility in a porcine model of healed myocardial infarction.* Journal of the American College of Cardiology, 2004. **44**(11): p. 2202-13.

28. van Heeswijk, R.B., et al., *Three-Dimensional Self-Navigated T2 Mapping for the Detection of Acute Cellular Rejection After Orthotopic Heart Transplantation.* Transplant Direct, 2017. **3**(4): p. e149.
29. Valinoti, M., et al., *3D patient-specific models for left atrium characterization to support ablation in atrial fibrillation patients.* Magnetic Resonance Imaging, 2018. **45**: p. 51-57.

FIGURES

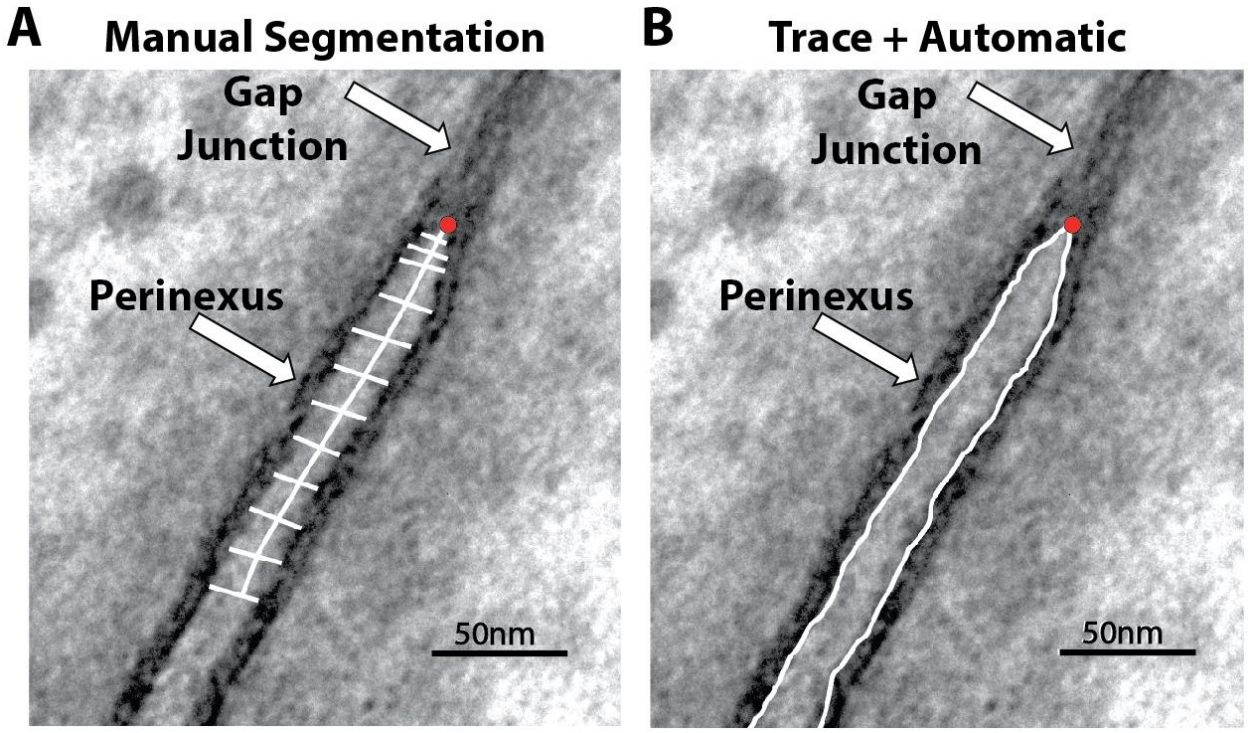

Figure 3.1 TEM images with quantification processes. The manual segmentation process (A) requires the user to perform 12 individual intermembrane measurements while estimating the centerline. The automatic process (B) requires a manual, continuous trace of the outline of the perinexus. The red dot in each image represents the user-identified end of the GJ and the beginning of the perinexus.

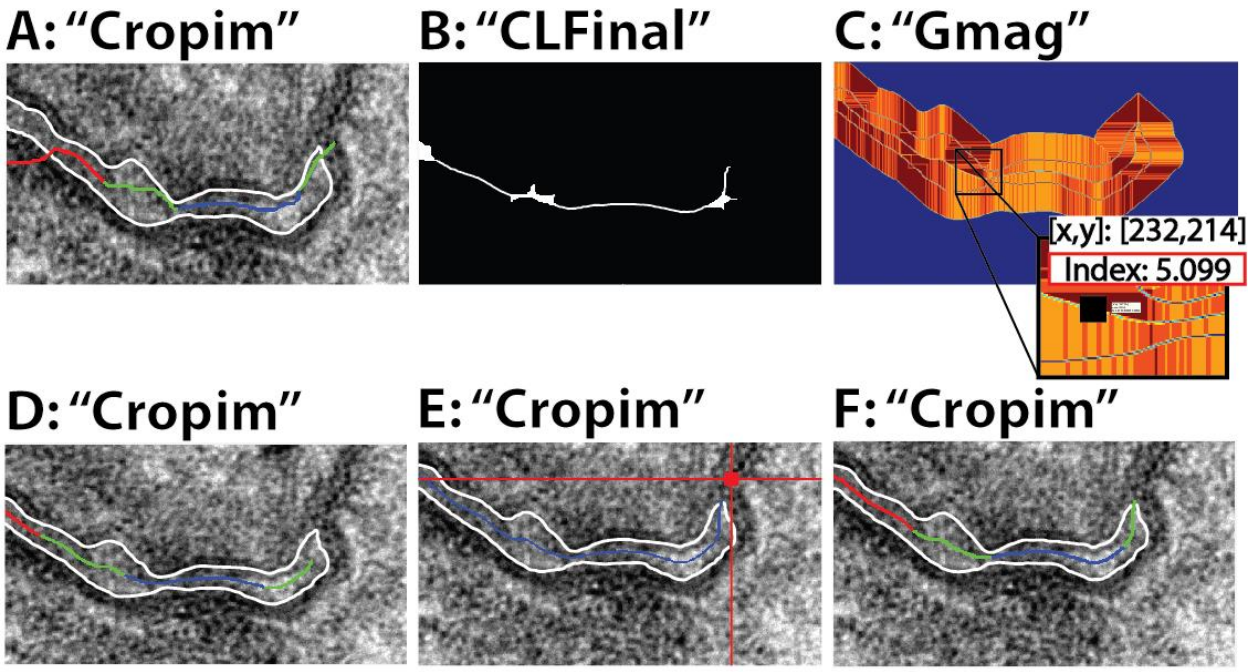

Figure 3.2 Centerline troubleshooting. Two primary modes of failure for the centerline identification and their solutions: Each image is labelled with the array name in Matlab. If the gradient threshold is too low (A, threshold 0.2) the centerline algorithm can fail. Setting the threshold too high (B, threshold 70) can reduce the computational efficiency of the pathfinding algorithm. An appropriate gradient threshold can be determined from the GMag array (C, insert). If the centerline fails to reach the beginning edge of the perinexus (D), the user can opt to manually select the start point. After the "Start Point" option is set to 1 in the opening GUI, the user then selects a point *outside* the perinexus of interest (E). The end result should be a centerline that accurately depicts the entirety of the perinexus, (F). All labels in quotations (A-F) correspond to the variable names in Matlab.

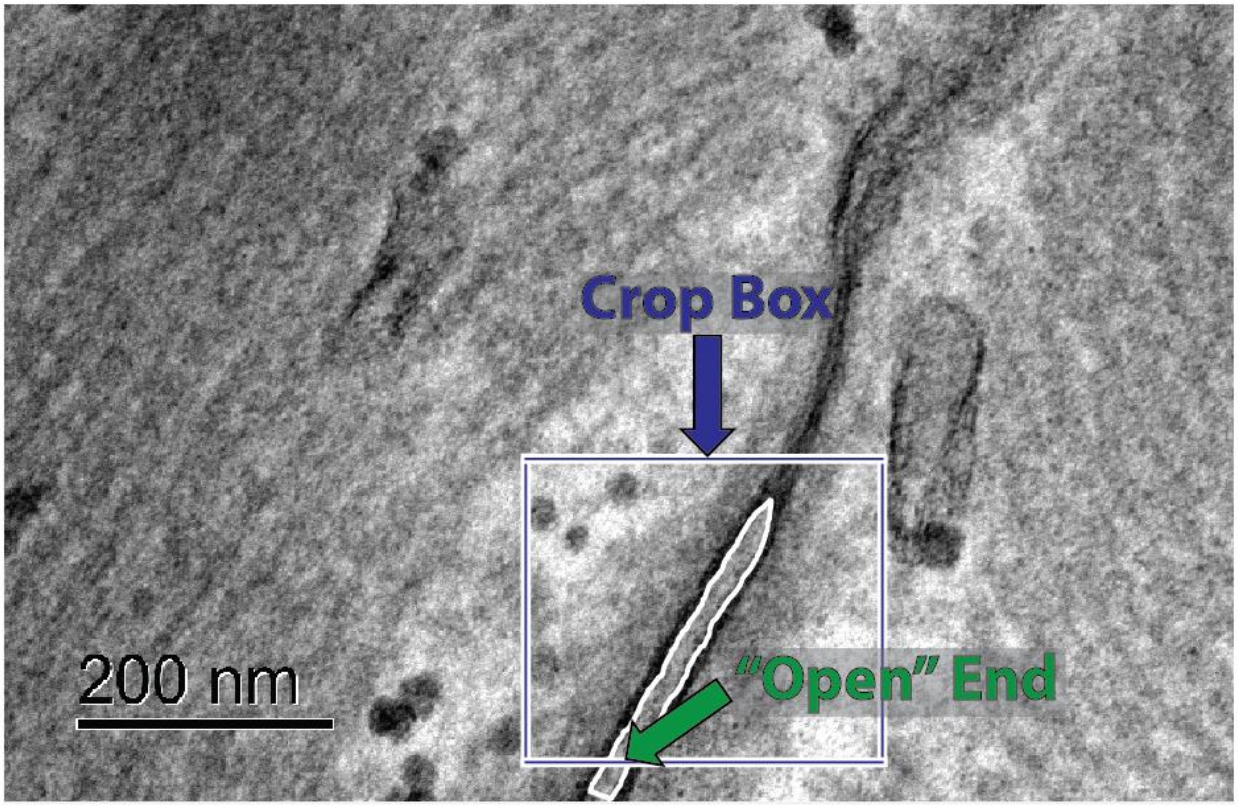

Figure 3.3 Perinexus Selection. To crop the perinexus, click-and-hold to drag a box around it (the crop tool is selected automatically) as shown by the blue arrow. This box can be adjusted by using the squares on the sides and corners to make it larger or smaller. The green arrow represents the end of the perinexus, which the user should ensure remains "open."

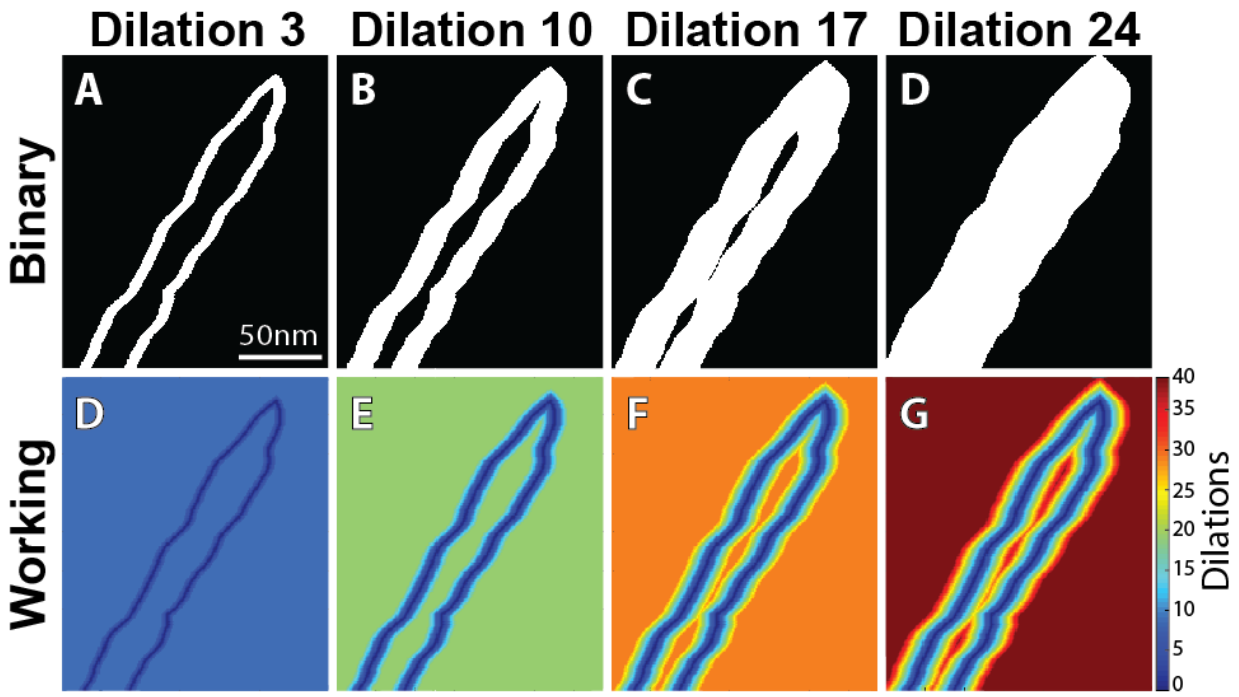

Figure 3.4 Serial image dilations. The binary outline is repeatedly dilated in one-pixel increments (A-D) and added to the working image (the non-binary form of the image, E-H) after each dilation.

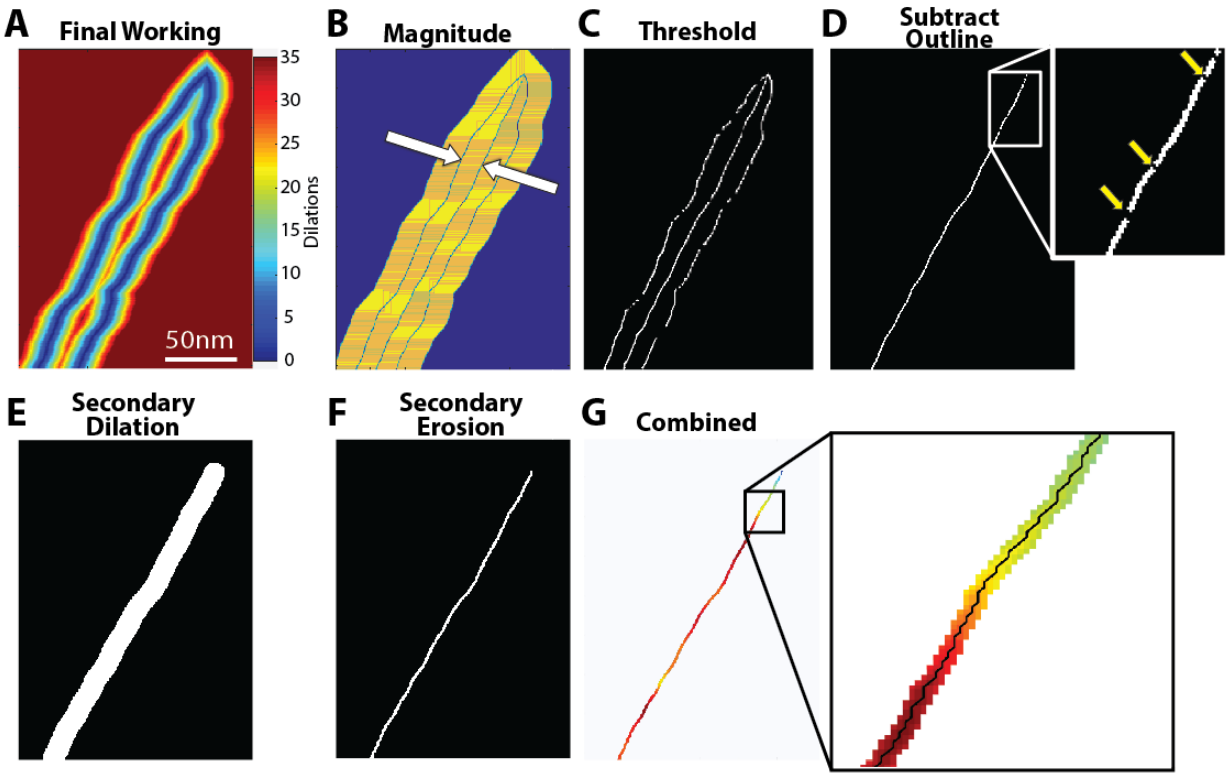

Figure 3.5 Centerline isolation and pathfinding. A spatial derivative is calculated from the final working image (A) and the magnitude of that spatial derivative (B) is used to isolate the outline and centerline (white arrows). A user-defined threshold identifies the outline and centerline and subtracting the original outline yields the centerline (D). However, gaps appear in the centerline as a result of the threshold (D – insert). In order to produce a continuous centerline, a secondary dilation is performed on the isolated centerline (E), followed by a secondary erosion to increase the computational efficiency of a subsequent pathfinding algorithm. This eroded image (F) is then combined with the final working image, allowing for the identification of a continuous, one-pixel-thick centerline (G – insert).

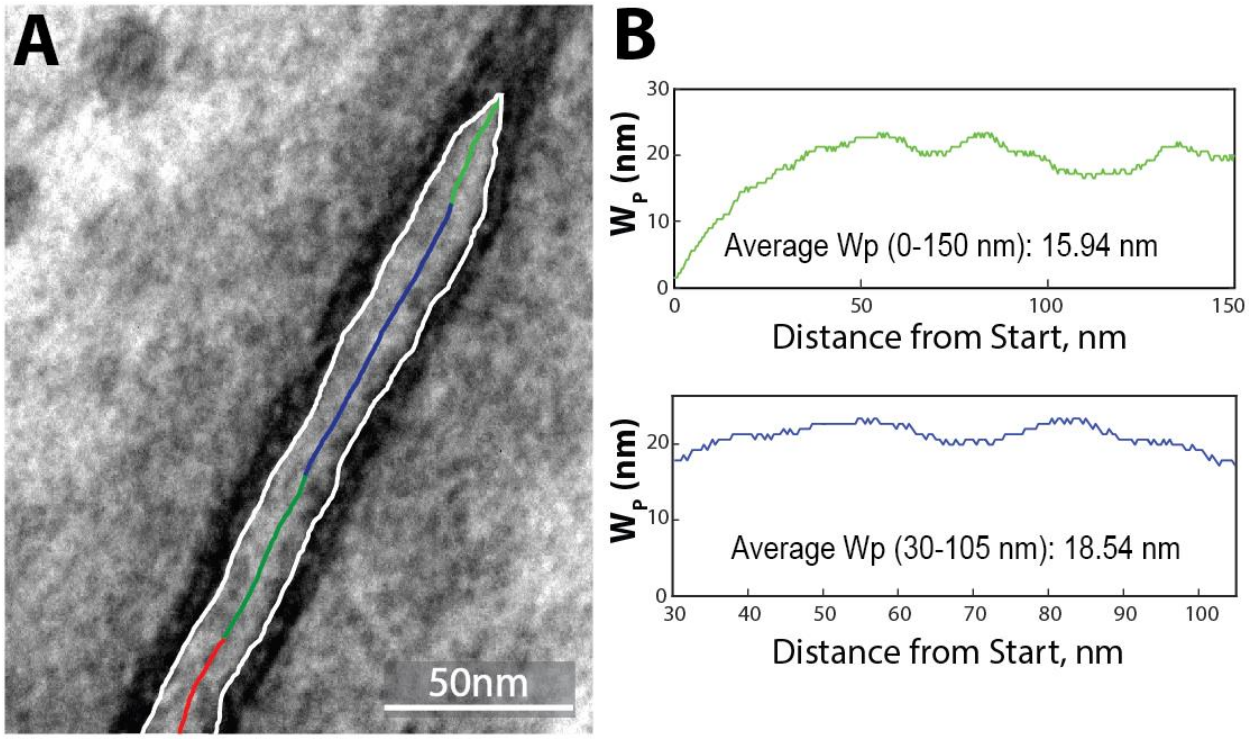

Figure 3.6 Final data presentation. The program outputs the final outline on top of the original TEM image (A). The line is color-coded green for 0-150 nm, blue for the user-defined region of interest and red for the area beyond 150 nm. Additionally, the program outputs a similarly color-coded chart representing W_p as a function of distance from the start of the perinexus and for the region of interest (B), as well as the average W_p (inset in respective graph).

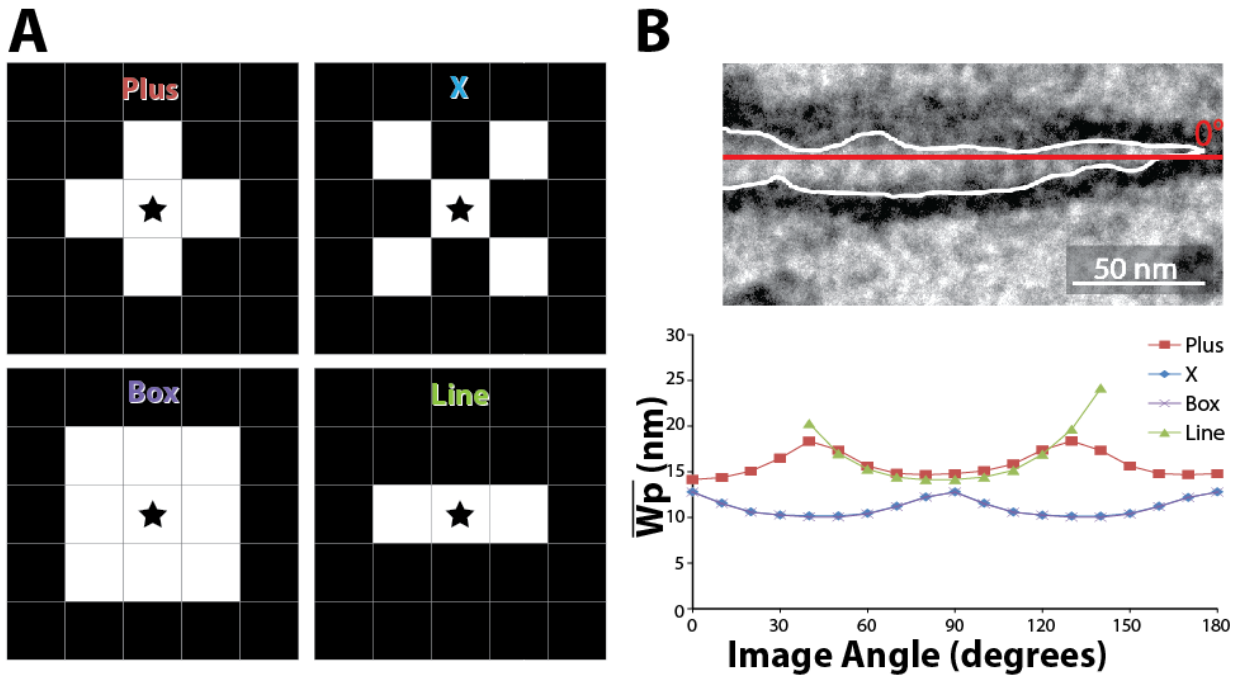

Figure 3.7 Dilation kernel shape analysis. Shapes for dilation kernels (A): the star in the middle represents the dilated pixels. White boxes are pixels affected by the dilation, in the shape of a plus, X, box or line. An approximately horizontal perinexus (B, top, with a red line indicating 0°) was rotated clockwise from 0 to 180° in steps of 10° and repeatedly dilated using the different kernel shapes (B, bottom). Plus- and line-shaped kernels produce similar results, although the line kernel fails at certain orientations, while the box- and X-shaped kernels are out of phase by 45°.

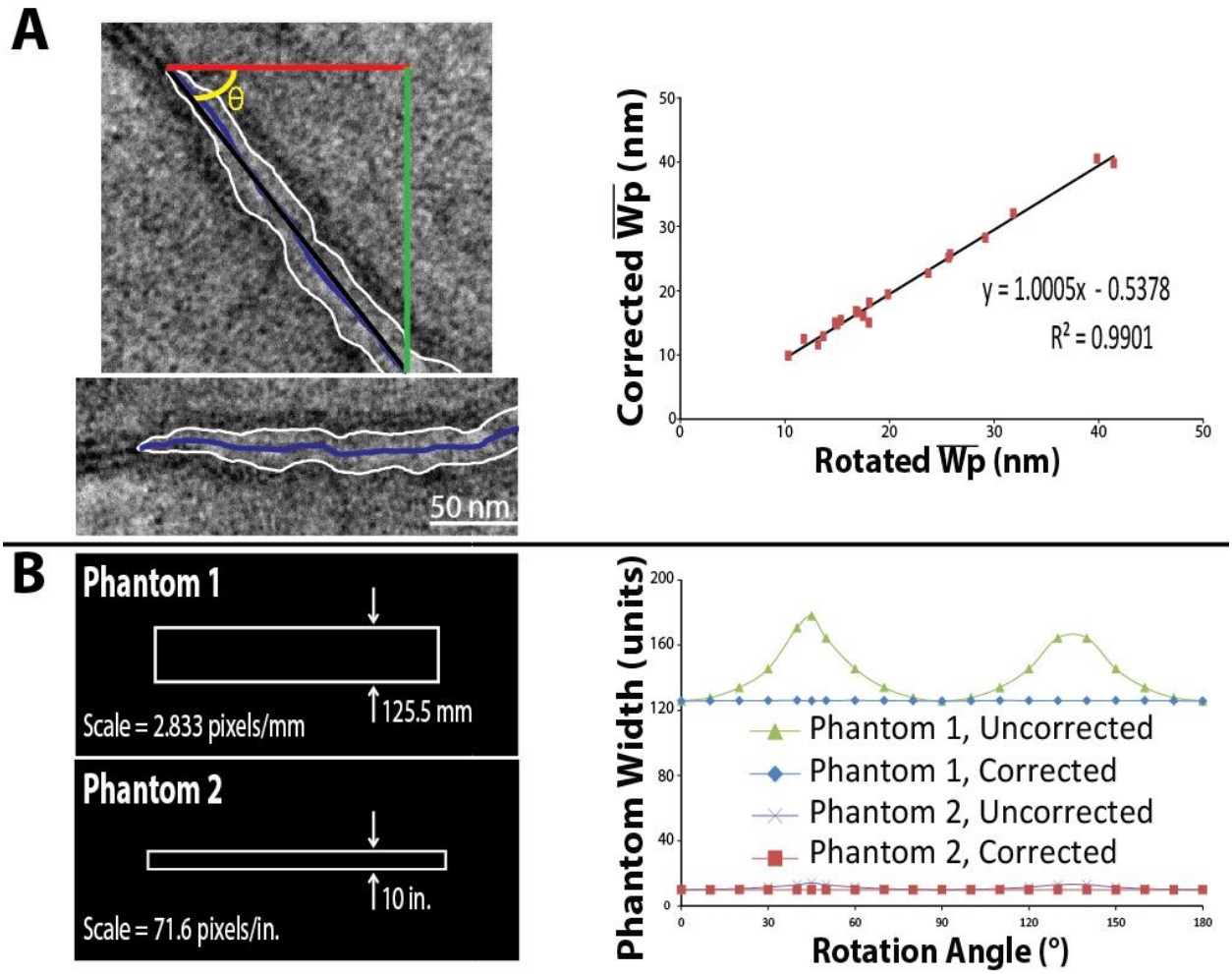

Figure 3.8 Image Orientation Correction. To correct for the orientation of the image, the average angle of the perinexus is calculated from the positions of the start- and end-points (A, left, beginning and end of black line). The inverse tangent of the change in the y-direction (A, left, green line) divided by the change in the x-direction (A, left, red line) yields the correction angle, θ (A, left, yellow). The goal is to then correct the average W_p value to give the minimum distance between the edges, as if the perinexus had been imaged approximately horizontally (A, left below). The application of the correction factor described by Equation 1 was compared to manually rotating each of 15 randomly-selected images by the calculated θ before analysis. The corrected values strongly correlated with the rotated-image values (R^2 = 0.991, A, Right), indicating Equation 1 is a valid correction factor for image orientation. To confirm the correction factor is appropriate, two phantoms were generated of perfectly-parallel edges with a known distance

between them (B, Left). Phantom 1 and Phantom 2 have spatial resolutions of 2.833 pixels/mm. and 71.6 pixels/in., respectively. As shown by the blue diamonds and red squares in B, Right, the algorithm accurately calculates their widths across 180 degrees of image rotation.

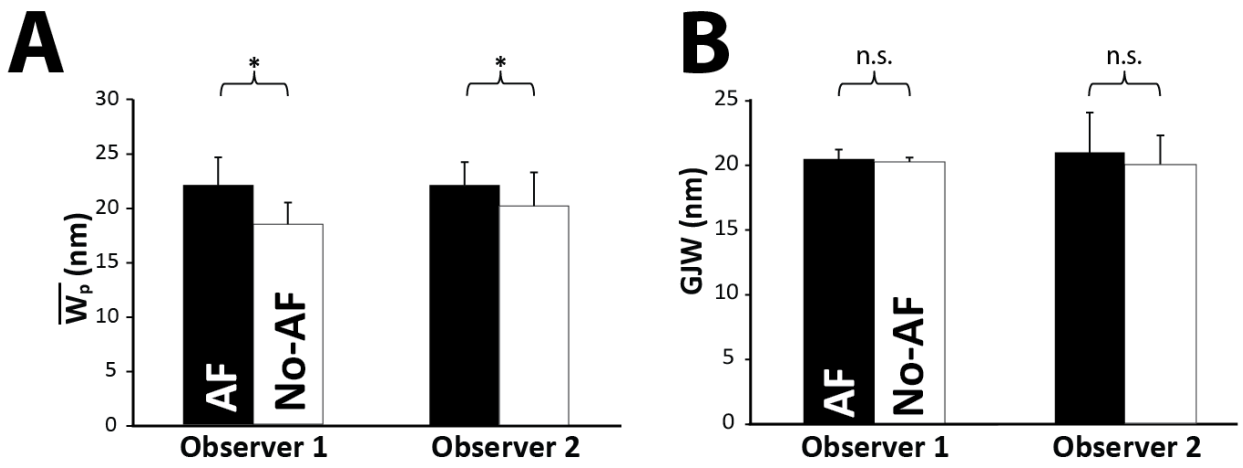

Figure 3.9 Algorithm reproducibility. Using the automatic process with image orientation correction, both an experienced and inexperienced observer found significant differences between AF and No-AF groups (A), consistent with a previous study, detecting a minimum difference of 2.6 nm. Additionally, neither observer found a significant difference in GJW (B).

	Manual	**Automatic**
Time - Obs. 1 (s)	205±11	44±14
Time - Obs. 2 (s)	248±18	30±5
Spatial Resolution (measurements/nm)	0.08	3.45

Table 3.1 Comparison of manual and automatic processes. Both observers required less time per image to trace the outline than to perform the manual segmentation process for a 10-image training set (supplemental file S5). Additionally, the automatic process has a higher sampling frequency, recording 3.45 measurements per nm, compared to an average of 1 measurement every 12.5 nm for the manual process. The training set images can be found in Supplemental File S5, along with outlines and measurements as performed by an experienced user.

APPENDIX: SUPPLEMENTAL DATA

```
3.1
39      %% Save Data Files
40      %If you want to save the data in a mat file, copy and past the following
41      %line into the command window and save it.  Then uncomment the next load
42      %line (line 38).
43      %WpData = [cellstr(filename ), cellstr( Ave150 ), cellstr( AveROI ), cellstr( Total Elapsed Time ), cellstr( User Input Time)];
44      % load WpData  %Load data file for storing Wp and time data
45
46      % Set the directory to save the list of Wp by distance from GJ edge
47 -    savefile = ['',file_name,'.mat'];
48
49      %% Figure Save Locations
50 -    savestringDC = ['',file_name]; %Directory for final working image figure:
51 -    file_name1 = [file_name,'A'];
52 -    savestringOCL = ['',file_name1]; %Directory for original image w/ centerline overlay:
53 -    savestringWPMP = ['',file_name]; %Directory for Wp/distance-from-GJ plot:
416     % save(savefile,'WpList')
417     %
418     %
419     % % If you are using the WpData file from the top of the code, uncomment the
420     % %following lines to save relevant data and figures.
421     %
422     % %Save data - [File name, 0-150nm Wp, ROIWp, total time, user input time]
423     % % WpData = [WpData;cellstr(file_name), num2cell(Ave150), num2cell(aveROI), num2cell(eltime), num2cell(userinputtime)];
424     % % save ('WpData','WpData');
425     % % %Save final working image figure
426     % % savestringDC = ['',file_name]; %Insert save location
427     % saveas(figure(6),savestringDC)
428     % % %Save original image w/ centerline overlay
429     % % savestringOCL = ['',file_name]; %Insert save location
430     % saveas(figure(7),savestringOCL)
431     % % %Save Wp/distance from GJ plot
432     % % savestringWPMP = ['',file_name]; %Insert save location
433     % saveas(figure(9),savestringWPMP)
3.3
8       %% Set Parameters
9       % The following are the default parameters.  The user will adjust if
10      % desired in the input box (Line 19)
11 -    GthreshDef = 4.5;  %Default threshold to isolate outline and centerline.  Typically between 5 and 8.  Higher threshold leads to m
12 -    scaleDef = 2.912; %Default scale in pixels/nm (200nm scale bar, VetMed scope)
13 -    ROIminDef = 30; %Identify Region of Interest (30-105nm is standard for perinexus, 10-90 standard for gap junction width)
14 -    ROImaxDef = 105;
3.4
6       %% Set File Select Location
7 -    selected_file = ('');
```

Figure 3.S.2 Program screenshot depicting algorithm setup.

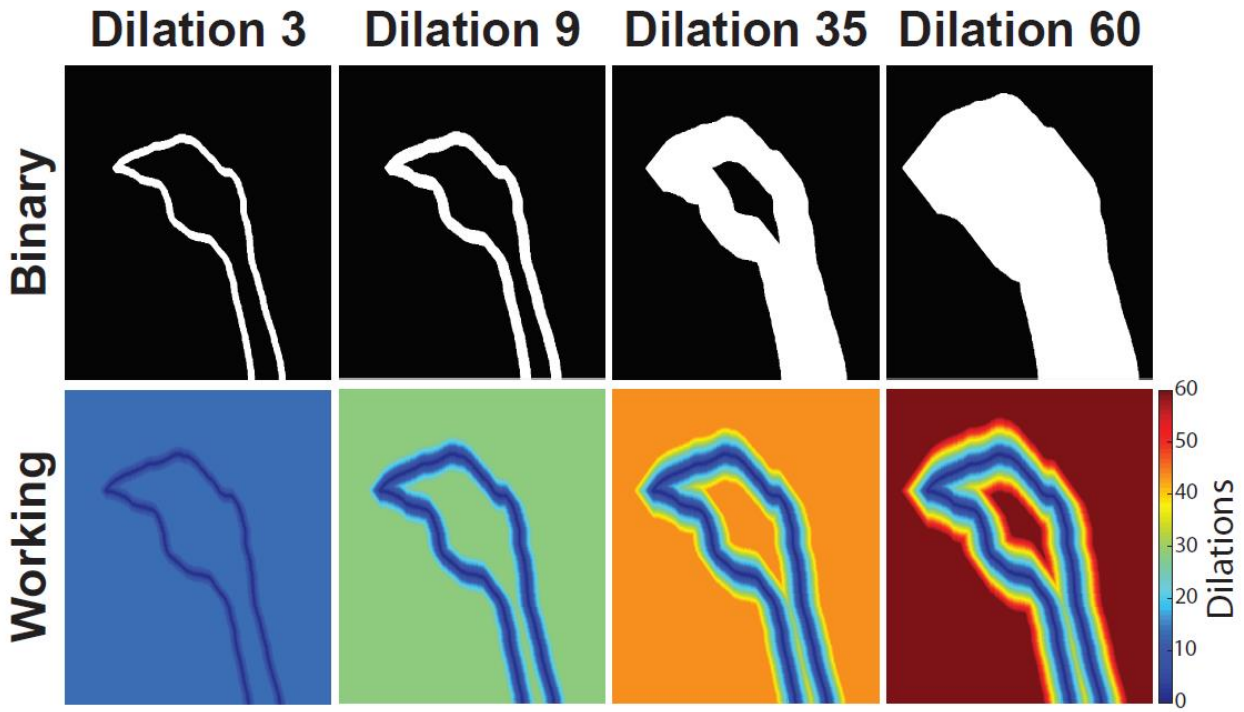

Figure 3.S.3 Serial image dilations of a wider perinexus.

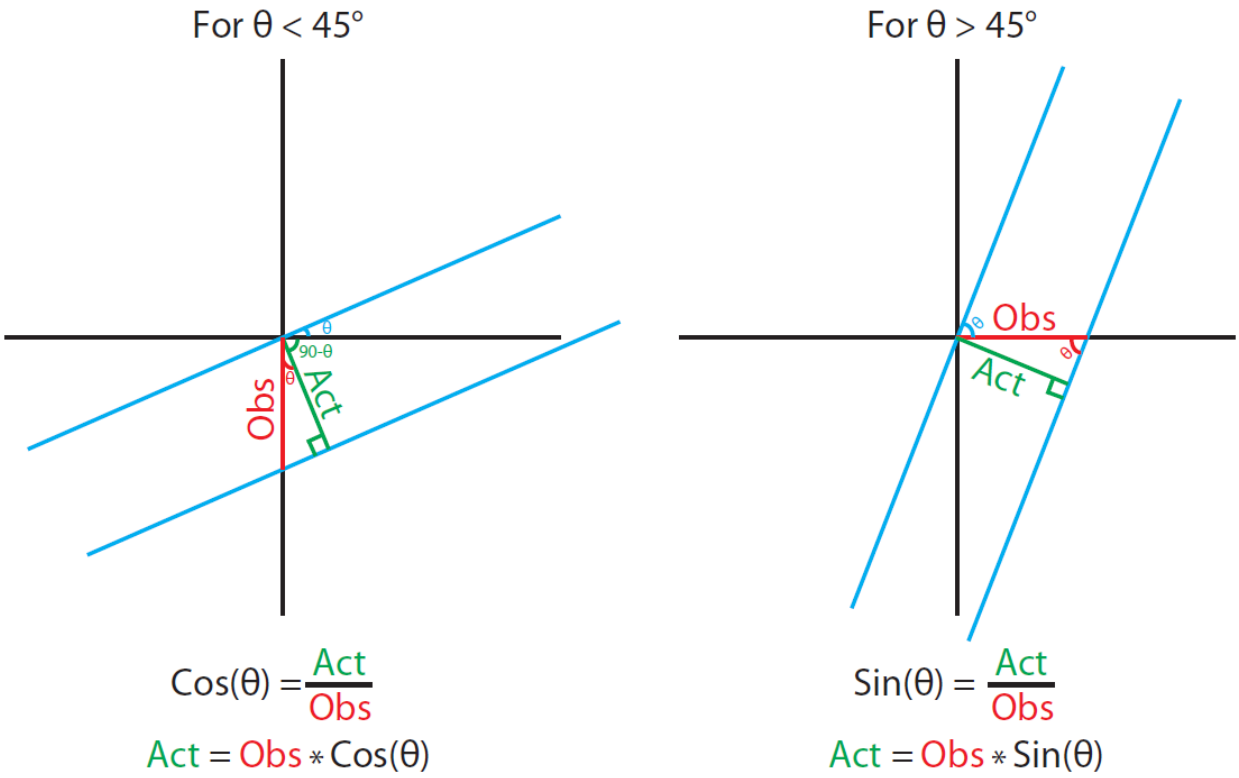

Figure 3.S.4 Trigonometric theory for orientation correction. Cases shown of images oriented at less than (left) or greater than (right) 45°. Blue line represent edges (in the case of this paper, cell membranes), red line ("Obs") is the observed distance, green ("Act") is the actual, orthogonal, distance between edges. At orientations of precisely 45°, the two cases are equal and default to the "sine" condition.

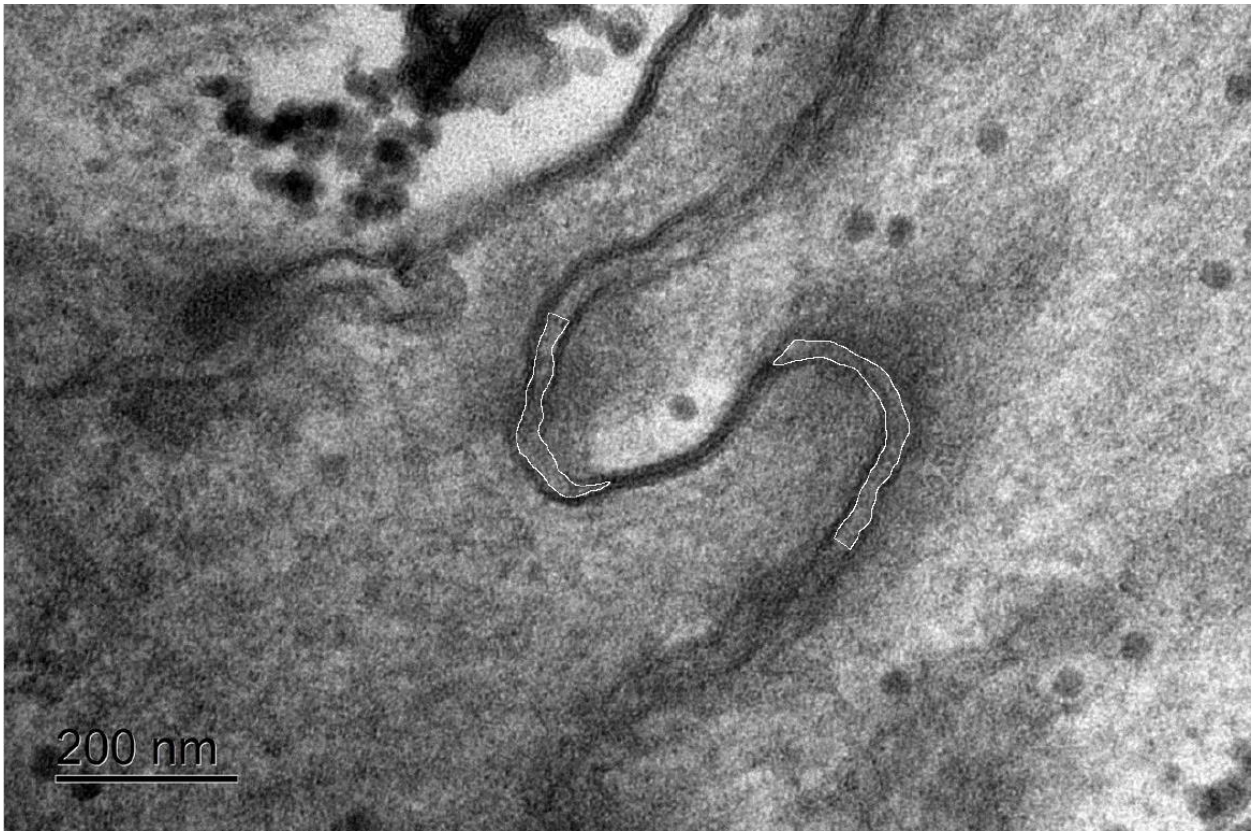

Figure 3.S.6 Low resolution perinexus image. The scale of this image is 0.928 pixels/nm, roughly 3 times lower-resolution than the other TEM images analyzed in this study. The calculated widths for the two perinexi shown are 21.84 nm and 14.23 nm. Both values are similar to manual measurements of the same perinexi and to measurements of other perinexi from the same tissue sample.

CHAPTER 4: OSMOTIC REGULATION OF THE CARDIAC PERINEXUS MODULATES CARDIAC CONDUCTION

FOREWORD

With the identification of the perinexus as a potential target for treating human disease and a high-throughput, high-resolution method for quantifying perinexal width developed and validated, the next step was to determine whether narrowing the perinexus could improve conduction, as mathematical models have suggested. Furthermore, a major goal of the study detailed in the following chapter is to resolve a controversy in the field: that of the role of the extracellular space in conduction. Canonical cable theory indicates that increasing the amount of fluid in bulk interstitium should lower the resistance of the return pathway between adjacent cardiomyocytes and therefore increase conduction velocity (CV), as detailed by the Fleischhauer and Kléber study from 1995. However, our lab has since shown the opposite: expanding interstitium can slow conduction, and collapsing the same microdomain can increase CV. The following study aims to demonstrate that while both of the above studies are scientifically valid, their conclusions may be incomplete: the answer may instead lie in the perinexus. The osmotic agents chosen for this demonstration are the Dextran 70kDa from the Fleischhauer study and the mannitol and albumin from the Veeraraghavan study. Additionally, a 2MDa Dextran will serve as an intriguing link between the two: it has been demonstrated to primarily localize within vasculature, much in the same way that albumin is thought to do so, presumably due to its large size and/or high viscosity when dissolved. It is also chemically identical to Dextran 70kDa, only a longer chain of the same molecule. I will quantify CV along with structural parameters typically associated with cable theory (C43 expression, interstitial volume and resistance) or ephaptic theory (Wp), and aim to definitively answer which mechanism is better able to modulate cardiac conduction.

INTRODUCTION

Cardiac electrophysiology has been well-understood to follow a cable-like model of electrical conduction through connexin gap junctions (GJs) [1-4]. However, experimental evidence and mathematical models have demonstrated contradictory results, indicating cable-like GJ coupling may not be the only mechanism of electrical cellular communication [2, 5-10]. The thorough understanding of cardiac conduction is critical in the diagnosis, treatment and prevention of arrhythmogenic diseases due to their high mortality rates and financial cost. In fact, in the United States, approximately 350,000 people die each year from sudden cardiac death [11] and Americans spend roughly $6 billion on treatment for atrial fibrillation (AF) [12]. It is therefore our goal to better understand mechanisms of conduction and conduction failure in order to open new therapeutic avenues for the treatment of cardiac arrhythmias. The specific regions of interest are in the interstitial spaces, including the lateral bulk interstitial microdomain along cardiomyocytes and the perinexus nanodomain adjacent to GJs within the intercalated disc (ID) [13]. According to canonical cable theory, bulk interstitium acts as the return pathway closing the electrical circuit of current flow through adjacent myocytes [3, 14]. As such, it is currently understood that modulating the resistance of this region should change overall conduction. A study from Fleischhauer and Kléber in 1995 elegantly demonstrated just such a direct relationship between interstitial space and electrical resistance, with *increased* fiber diameter correlating with *increased* conduction velocity and vice versa [15]. Controversy arose, however, with a recent study from our lab by Veeraraghavan *et al*, which demonstrated precisely the opposite phenomenon: *increased* interstitial volume (VIS) associated with *decreased* conduction velocity and vice versa [16].

The difference in results could be attributed to a number of factors, including different experimental models, interstitial space and conduction quantification techniques and perfusate compositions. We propose that while both studies are scientifically valid, their conclusions are incomplete. By describing the microdomain tissue structure of the heart, both investigators omitted a potentially critical region: the GJ-adjacent cardiac perinexus. This nanodomain has been identified as a candidate cardiac ephapse, a location wherein electric

field coupling could occur, due to its narrow cleft width between adjacent myocytes [5, 13, 17-20] and abundance of sodium channels [21, 22]. Additionally, we have both identified the perinexus in human atrial tissue and observed an inverse relationship between perinexal width (Wp) and chronic atrial fibrillation [23]. This structure could therefore offer insight into the apparently contradictory findings by Fleischhauer and Veeraraghavan. We hypothesize that cardiac conduction will most closely correlate with Wp instead of parameters typically associated with cable theory, including gap junctional protein expression, interstitial volume and interstitial resistance. Specifically, if conduction is driven by a primarily ephaptic mechanism of conduction, mathematical models and previous experiments predict that widening Wp can slow conduction.

METHODS

Guinea Pig Langendorff Preparations

Adult male Hartley guinea pigs were anesthetized by isoflurane inhalation and their ventricles isolated and perfused as Langendorff preparations using an oxygenated perfusion solution containing, as previously described [16], (in mMol/L): 1.25 CaCl2, 140 NaCl, 4.5 KCl, 10 Dextrose, 1MgCl2, 10 HEPES, 5.5 mL/L of NaOH and the electro-mechanical uncoupler 2,3-butanedionemonoxime to reduce motion, and was titrated using either HCl or NaOH to a pH of 7.41 at 37.0°C. In all experiments, control solution was perfused for 30 minutes, followed by the same solution with either mannitol (26.1 g/L), albumin (4 g/L), Dextran 70 kDa (40 g/L) or Dextran 2MDa (40 g/L) for 15 minutes. Mannitol, albumin and Dextran 70 kDa were selected for comparisons to previous studies [15, 16] and Dextran 2MDa was selected for its demonstrated tendency to stay primarily confined to vasculature [24]. Preparations were paced epicardially from the left ventricle (LV)-side of the left anterior descending coronary artery (LAD).

Optical Mapping

Conduction velocity (CV) was quantified by optical voltage mapping using di-4 ANEPPS (15μM) as previously described [16]. Briefly, the preparation was stained with di-4 ANEPPS by direct coronary

perfusion for approximately 10 minutes after an initial 15 minute stabilization period following cannulation. Following a 20 minute dye wash-out period, the tissue was excited by 510nm light and the emitted light, filtered by a 610nm filter, was captured by a Micam Ultima L-type CMOS camera.

Optical data were analyzed to quantify transverse (CVT) and longitudinal (CVL) CV, action potential duration (APD) [19, 25, 26]and maximum dispersion of repolarization – the greatest time difference in repolarization between the left, right, base and apex quadrants of the imaging field [18, 27]. APD was quantified as the time between activation and 90% repolarization.

Western Blots

Left ventricular tissue were snap frozen at specific time points in the protocol and western blotting was performed as previously described [28]. Briefly, the samples were homogenized in RIPA lysis buffer (containing 50mM Tris pH 7.4, 150mM NaCl, 1mM EDTA, 1% Triton X-100, 1% sodium deoxycholate, 2mM NaF, 200μM Na2VO34) supplemented with Roche Protease Inhibitor Cocktail (4693159001, Sigma-Aldrich). Protein concentration was determined by a BioRad DC protein assay and concentrations were normalized prior to analysis. Electrophoresis was performed to separate proteins which were then transferred to a PVDF membrane, blocked with 5% bovine serum albumin for 1 hour at room temperature and incubated overnight with a primary antibody against Cx43 phosphorylated at Ser368 (pCx43, 1:1000, #3511, Cell Signaling Technologies), at 4°C. The membranes were then washed and incubated with secondary antibody (1:5000, Goat Anti-Rabbit HRP, abcam) at room temperature for 1 hour. After washing, bound antibody was detected using West Pico Plus chemiluminescent substrate (Thermo Scientific) and imaged using the Licor Odyssey Fc system. Membranes were stripped with ReBlot Plus according to manufacturer's instructions, blocked in Odyssey Blocking Buffer (Licor) at room temperature for 1 hour and incubated with primary anitbodies against Cx43 (1:5000, C2619 rabbit, Sigma Aldrich) and GAPDH (1:5000, 101983-284 mouse, VWR). Membranes were then washed and incubated with secondary antibodies for 1 hour (both 1:10,000, goat anti-rabbit IRDye 800CW and goat anti-mouse IRDye 680RD)

and washed again. Membranes were again imaged using the Licor Odyssey Fc system to determine protein expression. Total Cx43 was normalized to GAPDH and pCx43 was normalized to total Cx43.

Histology

A positive-pixel analysis of hematoxylin and eosin (H&E)-stained LV tissue, which had been fixed in 10% formalin for at least 24 hours, was performed to quantify interstitial volume (VIS), similar to what we have described previously [16]. All measurements were made from the subepicardium, defined as the region from the epicardial surface to a depth of no more than 500 μm. Images of 5 μm-thick slices of stained tissue were analyzed by an Aperio positive-pixel analysis program which quantified interstitial space as a percentage of the entire array which was devoid of stained pixels.

Interstitial Impedance

In a separate group of experiments, hearts were cannulated with the same perfusion solutions described above, but were not perfused with optical dye. Instead, after a similar stabilization period, a four-probe stainless steel electrode array, with the electrodes 2mm apart and extending to a depth of 2mm, was placed on the anterior surface of the LV, approximately parallel to the LAD, and connected to a Gamry Interface 1000 Potentiostat. Using the Gamry Framework electrochemical impedance program, tissue impedance was measured with the following parameters: Frequency sweep: 1-1E10 Hz; points/decade: 10; ACV: 0.2mV; DVC: 0; Area: 1cm^2; Estimated Z: 100 Ω. The data was then fit to an ideal electrical circuit model and a frequency band of 200-2000 Hz identified as corresponding to interstitial resistance, demonstrated in Figure 1, as identified previously [29, 30]. We concluded that low-frequency (0-200 Hz) noise was likely an artifact from the fluid present on the epicardial surface, as the noise was absent from experiments performed on dried tissue (Supplemental Figure 4.S.1).

Electron Microscopy

Anterior epicardial tissue from the base of the LV (n = 8 hearts x 5 interventions) was collected from hearts after the conclusion of the optical mapping experiments. Tissue was cut into $1mm^3$ chunks which were fixed in 2.5% glutaraldehyde for at least 24 hours at 4°C before being washed and stored in phosphate-buffered saline (PBS) at 4°C. Samples were then prepared for TEM as previously described[19] and imaged, as previously described [19], using a JEM JEOL 1400 Electron Microscope at 150,000x magnification. 15 images were analyzed per sample using a previously-described custom Matlab program [31] to quantify Wp. The average intermembrane distance between 30-105nm from the edge of the gap junction plaque [23] is reported as Wp.

Statistical Analysis

Differences between experimental groups was determined through a Student's t-test, with Bonferroni correction applied for multiple comparisons. For the interstitial resistance measurements, a paired t-test was performed. For all other analyses, values are compared to their appropriate time control, with no osmotic agent added. Data are presented as mean ± standard deviation, $p < 0.05$ was considered statistically significant.

RESULTS

Whole-Heart Electrophysiology

We quantified ventricular CV by optical mapping during perfusion with our historic lab standard solution and after 15 minutes perfusion of that same solution with one of the osmotic agents. In Figure 2A, representative optical maps demonstrate that epicardial conduction is similar during the baseline period with all osmotic agents. After 15 minutes, conduction velocity is relatively similar in the time control optical maps, is decreased with mannitol as evidenced by isochrones crowding, is increased by albumin as evidenced by isochrone spread, is unchanged by Dextran 70kda, and increased by Dextran 2MDa . Quantified as a percent change from each heart's baseline, summary data in Figure 2B reveals changes in

CV with each intervention and all changes are compared to the time control group. Importantly, Mannitol significantly decreased CV and albumin significantly increased CV (Figure 2A), preferentially in the transverse direction for both interventions (Figure 2B). Interestingly, Dextran 70kDa did not significantly change conduction (Figure 2) relative to time control. However, Dextran 2MDa preferentially and significantly increased transverse conduction (Figure 2).

To explore whether conduction changes might be attributable to more significant electrophysiologic remodeling, action potential duration (APD) and the maximum dispersion of APD between the left ventricular basal and right ventricular apical quadrants of the imaging field [27]. The osmotic agents did not alter APD or APD dispersion (Figure 3), suggesting that the primary mechanisms governing conduction changes we observed may be primarily due to mechanisms of cell-to-cell electrical communication.

Gap Junctions

Since it is well accepted that gap junctions play an important role in cell-to-cell communication [1, 2, 32], we first quantified total expression of the primary ventricular gap junction protein Connexin 43 (Cx43) and probed phosphorylation at serine 368 (S368), which has been associated with changes in connexin conductivity [33, 34]. Across our conditions, however, we saw no significant differences in Cx43 expression or phosphorylation at S368 (Figure 4) as quantified by Western immunoblotting. While protein expression does not necessarily correlate with protein function, these results combined with the rapid changes in conduction suggest that CV modulation is driven primarily by a mechanism other than gap junctional coupling.

Bulk Interstitium

According to canonical cable theory, it is possible to alter CV even without changing gap junctional resistance by modulating the resistance of the extracellular space. By increasing the volume of bulk

interstitium – the percentage of tissue unoccupied by cardiac cells – we should see a decrease in interstitial resistance and therefore an increase in CV.

We quantified interstitial volume (VIS) with a positive-pixel analysis of H&E stained tissue and found no significant differences between tissue subjected to 15 minutes of perfusion with any osmotic agent (Figure 5). It is possible that the histologic method is simply unable to detect statistically significant differences between osmotic agents, so we quantified tissue impedance at baseline and 20 minutes with the different interventions. Summary data in Figure 6 reveals that neither mannitol nor albumin significantly affect impedance, while Dextran 70kDa and 2MDa increased impedance, relative to baseline. Resistances of solutions containing each osmotic agent were similar (36 Ω for Time Control, 39 Ω for mannitol, 35 Ω for albumin, 39 Ω for Dextran 70kDa and 38 Ω for Dextran 2MDa), indicating the effects of the electrical properties of the osmotic agents were likely not a significant source of error.

By the conventional cable theory model of conduction, cardiac conduction velocity should be directly proportional to extracellular tissue impedance. These data, however, do not consistently support such a model, indicating a different conduction mechanism may better relate changes in extracellular resistance and conduction.

Computational models suggest that conduction is also modulated by the conductivity of extracellular nanodomains in the ID that are rich in sodium channels by a mechanism of ephaptic communication [5, 20, 35, 36]. The mechanism of ephaptic mediated conduction is supported by work from our group that suggests the gap junction adjacent perinexus is a candidate structure for ephaptic coupling, and that significant perinexal expansion by osmotic agents [17, 21] is inversely correlated with cardiac conduction. However, evidence is lacking to directly link perinexal narrowing by osmotic agents to increased conduction velocity. We therefore quantified the width of the cardiac perinexus after perfusion with each of the osmotic agents.

Ventricular Perinexus

Representative perinexi from the left ventricle of hearts are shown in Figure 7A at 150,000x magnification, demonstrating that osmotic agents differentially modulate cell membrane separation immediately adjacent to the gap junction plaque. Importantly, perinexal quantification reveals an inverse correlation between Wp and conduction. Specifically, mannitol increases Wp (Figure 7), as previously reported, along with the observed conduction slowing. On the other hand, albumin narrows the perinexus, as does Dextran 2MDa, which were both associated with increased CV. Furthermore, Dextran 70kDa, which did not change CV relative to time control, does not alter Wp. Therefore, the inverse relationship between Wp and CV supports a primarily ephaptic mechanism of osmotically regulated cardiac conduction.

DISCUSSION

Osmotic Agents, Structural Changes and Conduction

In the present study, we present two primary observations: that the cardiac Wp can be osmotically regulated acutely, and that the regulation of Wp has an inverse relationship with conduction velocity. Relative to time control, mannitol addition to the perfusate was associated with slowed conduction within 15 minutes, while albumin and Dextran 2MDa increased CV. Dextran 70kDa, however, did not significantly change CV. We saw no significant changes to overall Cx43 expression or phosphorylation at S368 between conditions. We also quantified both interstitial space and interstitial resistance via an electrochemical impedance measurement and found no changes that could explain the conduction behavior associated with each osmotic agent. Wp, however, did change significantly with osmotic agents. Mannitol, which slowed CV, widened the perinexus relative to time control, while albumin and Dextran 2MDa, which both increased CV, narrowed the perinexus. Dextran 70kDa did not significantly change the perinexus or CV. Our interpretation of these data is that conduction changes with osmotic agents follow a primarily ephaptic mechanism and cannot be explained by structural changes associated with cable theory.

Comparison of Results to Previous Studies with Osmotic Agents

In this study, CV measurements for both mannitol and albumin were similar to those described earlier [16]. Mannitol also expanded Wp as we reported earlier [21, 37]. Obtaining similar measurements under nearly identical experimental conditions indicates a consistently-observable effect that is not particular to a single experimentalist. In contrast, Fleischhauer and Kléber reported a significant decrease in CV upon Dextran 70kDa wash-in [15], which we did not observe. This difference in results may be explained by key experimental differences. First, the previous study was conducted in rabbit papillary muscle and subjected to an electrical cable analysis. Such an experimental approach could have been more sensitive to interstitial changes, while our experiments were performed in a whole-heart with transmural rotational anisotropy [8, 16, 25, 26, 38] and epicardially mapped. More specifically, the papillary muscle preparation, with a more homogenous cellular orientation structure provides for a less complex measurement of CV, while epicardial optical mapping reports the fastest and slowest axes of propagation. Estimating longitudinal conduction from optical maps is further complicated by source-sink issues due to wavefront curvature [39-42] that the papillary muscle may not exhibit. Still, we did not observe transverse changes in conduction velocity where the wavefront is more linear and conduction is more dependent on the number of cell-to-cell junctions encountered per unit length than in the longitudinal direction. Secondly, the papillary muscle experiments contained albumin throughout the duration of the experiment and, as we demonstrated, albumin alone decreased perinexal width and increased CV. The addition of Dextran 70 to albumin could further decrease perinexal width, though the effects on conduction are difficult to anticipate, as computational models predict diminishing returns of conduction gain progressing to conduction slowing as perinexal width decreases and self-attenuation increases. Self-attenuation is predicted to occur when sodium channels decrease extracellular potential or deplete sufficient extracellular sodium from the shared cleft to reduce sodium driving force in those nanodomains. Thus, additional experiments are still necessary to determine why Dextran 70 could decrease conduction in the study by Dr. Fleischhauer and colleagues.

Structural Changes Associated with Cable Theory do not Predict CV Changes

The most likely relevant components to affect cardiac conduction, via a cable-like conduction mechanism are the connexin gap junctions and the interstitial space. As the half-life of gap junctions on the cell membrane is on the scale of 60-90 minutes [43] and we observed CV changes at 15 minutes, it may not be surprising that we do not see any significant changes in overall connexin expression or phosphorylation. We chose S368 as a possible phosphorylation site due to its association with changing gap junction conductivity [34, 44]. Though we cannot definitively rule out changes to gap junction assembly or post-translational modification at other sites, our data combined with the short time scale of conduction changes suggest that the primary mechanism for those changes lies beyond the gap junctions.

Therefore, we next turned our attention to the interstitial space, which acts as the return pathway closing the electrical circuit formed by coupled adjacent cardiomyocytes. First, we measured VIS, the area unoccupied by cells and therefore filled with more highly-conductive fluid. We saw no changes, though acknowledged it is possible our experimental design was insufficiently sensitive to detect any possible differences. We then executed a series of electrochemical impedance experiments in order to more directly quantify interstitial resistance. However, our results were also inconsistent with cable theory, as impedance changes did not correlate consistently with conduction. Specifically, the two dextrans, 70kda and 2MDA, both increased impedance but the 2MDa dextran increased CV and the 70kDa dextran did not change CV. Importantly, Dextran 70 increased bulk extracellular impedance in whole-heart (by 18.5%), similar to what was reported by Dr. Fleischhauer *et al* (a change of roughly 35%) in papillary muscle even as the change in CV is not consistent between studies.

Interestingly, impedance was not significantly affected by mannitol or albumin, which decreased and increased CV, respectively. By a purely cable-like mechanism of conduction, our CV results do not correlate with the impedance data, once again suggesting a different conduction mechanism whose modulation would predominate over any changes associated with altered bulk interstitial resistance.

The Wp-GJ Relationship

While experimental evidence suggests gap junctions are necessary for conduction and may play an even more critical role in the formation of the ID, our data supports the idea that the mechanisms of gap junctional and ephaptic coupling may complement each other. Previously, Wp expansion has been and mathematically shown to first increase and then decrease CV at intercellular junctions exceeding 20 nm [5, 6, 10, 36]. Furthermore, each model also predicts reduced CV sensitivity to altered GJ coupling when intercellular separation is below approximately 20 nm, and significantly enhanced conduction sensitivity to altered GJ coupling at much wider distances. These predictions have since been validated in mice and guinea pigs [19, 21, 38]. Additionally, expansion of the perinexus has been associated with chronic atrial fibrillation in humans [23].

Although we have previously observed an inverse relationship between Wp and chronic atrial fibrillation [45], and mathematical models have suggested narrowing the perinexus could improve conduction, this is the first study to demonstrate that narrowing the perinexus increases CV. Since albumin is a negatively-charged globular protein that binds to the endothelial glicocalax and therefore could be associated with unknown offtarget effects we have not quantified, we used a second osmotic agent, Dextran 2MDa, to support the albumin result. Together, the albumin and Dextran 2MDa data suggest that osmotic agents which are thought to be primarily confined to vasculature, by either binding affinity or size, can osmotically regulate cardiac nanostructures.

Osmotic Agent Effects

As alluded to with albumin, the osmotic agents employed in this study have other effects in addition to changing oncotic pressure, and some are used clinically for these other effects. For example, albumin, a negatively charged plasma protein in solution at a pH of 7.4 [46, 47], has been used to regulate blood pressure due to its binding affinity to the endothelium in blood vessels, only leaving vasculature at a rate of

approximately 5% per hour [48]. Albumin furthermore regulates vascular function and can bind to a number of cations, fatty acids and hormones, in addition to acting as an antioxidant [49].

Mannitol, a sugar alcohol, has been used as a hyperosmotic agent to treat high intracranial pressure [50, 51]. With appropriate dosing and time courses of treatment, mannitol will decrease interstitial edema by drawing fluid out of cerebral parenchyma, though at higher doses and for long time courses, mannitol will also cross the blood-brain barrier [52]. Once across the blood-brain barrier, mannitol will then have the opposite intended effect, more similar to what we have observed in cardiac tissue: drawing fluid into tissue and exacerbating edema [53] . Furthermore, there is evidence that mannitol acts as an antioxidant and can attenuate ischemia-reperfusion injury [54-56], though the acute antioxidant effects on an otherwise healthy heart are also unknown.

Dextrans of various sizes have been used, like albumin, as a blood volume expander [57-59], with larger dextrans having a more pronounced effect on blood viscosity [59]. Dextran 70kDa has antithrombotic properties and reduces the inflammatory response and troponin-I release after cardiac surgery [60, 61]. It remains unknown, however, whether the other non-osmotic properties affected our results over the much more acute time frame of 20 minutes studied here.

Despite our efforts to select osmotic agents without binding or metabolic effects which could alter the function of cardiac cells, we cannot definitively exclude any such effects and advise the reader to interpret our results with caution and without direct application to any clinical treatment.

Limitations

These experiments were conducted in excised, isolated guinea pig ventricles which were perfused with Di-4 ANEPPS and preserved for H&E analysis and electron microscopy with formalin and glutaraldehyde, respectively. As such, all values of structural dimensions presented –Wp and VIS in particular – should be

interpreted cautiously and without implication of physiologic values. Additionally, while our CV results are similar to those published previously [16], we saw no significant differences in interstitial volumes between interventions, though all of our values were similar to the controls reported previously. It is worth noting that the reported interstitial volume differences may be attributed to a shorter protocol (15 minutes vs 60 minutes), different fixatives (formalin vs glutaraldehyde) and different analysis programs (positive-pixel vs color deconvolution). Interestingly, the study by Fleischhauer suggests that 30 minutes were required to reach steady state extracellular resistance changes. To determine whether time could be a critical factor in the structural changes associated with albumin and mannitol, we performed additional experiments including 40 minutes of osmotic agent perfusion. The data can be seen in supplemental figure 4.S.2, where CV stays virtually constant after approximately 15 minutes, but VIS results are closer to what was reported previously. Although there is no significant difference between time control and the osmotic agents, it is also important to note that arm of our study is slightly underpowered compared to the Veeraraghavan study, as we used 4 and 5 hearts, respectively, per condition. Albumin is furthermore difficult to work with in an optical mapping experiment because signal quality degrades quickly, as is demonstrated in supplemental figure 4.S.3, and the reasons for this are not entirely understood since the absorption peak of albumin is approximately 280 nm [62, 63] and di-4-ANNEPS' peak excitation is near 480 nm.

CONCLUSIONS

In this study, we demonstrated it is possible to osmotically regulate the perinexus and that this perinexal regulation has an inverse relationship with cardiac conduction. While we cannot definitively exclude the effects of other structural changes, namely expression, phosphorylation, or assembly of gap junction proteins or interstitial volume or resistance, the data suggest that perinexal modulation is a stronger determinant of cardiac conduction. The perinexus therefore continues to emerge as a therapeutic target for preventing cardiac arrhythmias and further research is crucial to better understanding under what conditions

perinexal expansion is beneficial adaptation or pathologic remodeling and how such targeting could be accomplished clinically.

REFERENCES

1. Nadim, F. and J. Golowasch, *Signal transmission between gap-junctionally coupled passive cables is most effective at an optimal diameter.* J Neurophysiol, 2006. **95**(6): p. 3831-43.
2. Keener, J.P., *The effects of gap junctions on propagation in myocardium: a modified cable theory.* Ann N Y Acad Sci, 1990. **591**: p. 257-77.
3. Henriquez, C.S., *Simulating the electrical behavior of cardiac tissue using the bidomain model.* Crit Rev Biomed Eng, 1993. **21**(1): p. 1-77.
4. Johnston, B.M., et al., *Quantifying the effect of uncertainty in input parameters in a simplified bidomain model of partial thickness ischaemia.* Med Biol Eng Comput, 2018. **56**(5): p. 761-780.
5. Lin, J. and J.P. Keener, *Ephaptic coupling in cardiac myocytes.* IEEE Trans Biomed Eng, 2013. **60**(2): p. 576-82.
6. Lin, J. and J.P. Keener, *Microdomain effects on transverse cardiac propagation.* Biophys J, 2014. **106**(4): p. 925-31.
7. Lin, J. and J.P. Keener, *Modeling electrical activity of myocardial cells incorporating the effects of ephaptic coupling.* Proc Natl Acad Sci U S A, 2010. **107**(49): p. 20935-40.
8. George, S.A., et al., *Extracellular sodium and potassium levels modulate cardiac conduction in mice heterozygous null for the Connexin43 gene.* Pflugers Archiv: European Journal of Physiology, 2015.
9. Weinberg, S.H., *Ephaptic coupling rescues conduction failure in weakly coupled cardiac tissue with voltage-gated gap junctions.* Chaos, 2017. **27**(9): p. 093908.
10. Kucera, J.P., S. Rohr, and Y. Rudy, *Localization of sodium channels in intercalated disks modulates cardiac conduction.* Circ Res, 2002. **91**(12): p. 1176-82.
11. Benjamin, E.J., et al., *Heart Disease and Stroke Statistics-2017 Update: A Report From the American Heart Association.* Circulation, 2017. **135**(10): p. e146-e603.
12. January, C.T., et al., *2014 AHA/ACC/HRS guideline for the management of patients with atrial fibrillation: a report of the American College of Cardiology/American Heart Association Task Force on Practice Guidelines and the Heart Rhythm Society.* J Am Coll Cardiol, 2014. **64**(21): p. e1-76.
13. Rhett, J.M. and R.G. Gourdie, *The perinexus: a new feature of Cx43 gap junction organization.* Heart Rhythm, 2012. **9**(4): p. 619-23.
14. Kleber, A.G. and C.B. Riegger, *Electrical constants of arterially perfused rabbit papillary muscle.* J Physiol, 1987. **385**: p. 307-24.
15. Fleischhauer, J., L. Lehmann, and A.G. Kleber, *Electrical resistances of interstitial and microvascular space as determinants of the extracellular electrical field and velocity of propagation in ventricular myocardium.* Circulation, 1995. **92**(3): p. 587-94.
16. Veeraraghavan, R., M.E. Salama, and S. Poelzing, *Interstitial volume modulates the conduction velocity-gap junction relationship.* Am J Physiol Heart Circ Physiol, 2012. **302**(1): p. H278-86.
17. Rhett, J.M., et al., *The perinexus: Sign-post on the path to a new model of cardiac conduction?* Trends in Cardiovascular Medicine, 2013.
18. Veeraraghavan, R., et al., *Potassium channels in the Cx43 gap junction perinexus modulate ephaptic coupling: an experimental and modeling study.* Pflugers Archiv: European Journal of Physiology, 2016.
19. George, S.A., et al., *Extracellular Sodium Dependence of the Conduction Velocity-Calcium Relationship: Evidence of Ephaptic Self-Attenuation.* Am J Physiol Heart Circ Physiol, 2016: p. ajpheart 00857 2015.
20. Mori, Y., G.I. Fishman, and C.S. Peskin, *Ephaptic conduction in a cardiac strand model with 3D electrodiffusion.* Proc Natl Acad Sci U S A, 2008. **105**(17): p. 6463-8.
21. Veeraraghavan, R., et al., *Sodium channels in the Cx43 gap junction perinexus may constitute a cardiac ephapse: an experimental and modeling study.* Pflugers Archiv: European Journal of Physiology, 2015.

22. Veeraraghavan, R. and R. Gourdie, *Stochastic Optical Reconstruction Microscopy-based Relative Localization Analysis (STORM-RLA) for Quantitative Nanoscale Assessment of Spatial Protein Organization.* Mol Biol Cell, 2016.
23. Raisch, T.B., et al., *Intercalated Disk Extracellular Nanodomain Expansion in Patients With Atrial Fibrillation.* Front Physiol, 2018. **9**: p. 398.
24. Dreher, M.R., et al., *Tumor vascular permeability, accumulation, and penetration of macromolecular drug carriers.* J Natl Cancer Inst, 2006. **98**(5): p. 335-44.
25. George, S.A. and S. Poelzing, *Cardiac conduction in isolated hearts of genetically modified mice - Connexin43 and salts.* Prog Biophys Mol Biol, 2015.
26. Entz, M., 2nd, et al., *Heart Rate and Extracellular Sodium and Potassium Modulation of Gap Junction Mediated Conduction in Guinea Pigs.* Frontiers in Physiology, 2016. **7**: p. 16.
27. Burton, F.L. and S.M. Cobbe, *Dispersion of ventricular repolarization and refractory period.* Cardiovasc Res, 2001. **50**(1): p. 10-23.
28. Smyth, J.W., et al., *Limited forward trafficking of connexin 43 reduces cell-cell coupling in stressed human and mouse myocardium.* J Clin Invest, 2010. **120**(1): p. 266-79.
29. Zhao, Y., et al., *Ablation outcome of irreversible electroporation on potato monitored by impedance spectrum under multi-electrode system.* Biomed Eng Online, 2018. **17**(1): p. 126.
30. Bonakdar, M., et al., *The Feasibility of a Smart Surgical Probe for Verification of IRE Treatments Using Electrical Impedance Spectroscopy.* IEEE Trans Biomed Eng, 2015. **62**(11): p. 2674-84.
31. Raisch, T., M. Khan, and S. Poelzing, *Quantifying Intermembrane Distances with Serial Image Dilations.* J Vis Exp, 2018(139).
32. Joyner, R.W., et al., *Propagation through electrically coupled cells. Effects of a resistive barrier.* Biophys J, 1984. **45**(5): p. 1017-25.
33. Ek-Vitorin, J.F., et al., *Selectivity of connexin 43 channels is regulated through protein kinase C-dependent phosphorylation.* Circ Res, 2006. **98**(12): p. 1498-505.
34. Lampe, P.D., et al., *Phosphorylation of connexin43 on serine368 by protein kinase C regulates gap junctional communication.* J Cell Biol, 2000. **149**(7): p. 1503-12.
35. Rudy, Y. and W.L. Quan, *A model study of the effects of the discrete cellular structure on electrical propagation in cardiac tissue.* Circ Res, 1987. **61**(6): p. 815-23.
36. Hichri, E., H. Abriel, and J.P. Kucera, *Distribution of cardiac sodium channels in clusters potentiates ephaptic interactions in the intercalated disc.* J Physiol, 2018. **596**(4): p. 563-589.
37. Greer-Short, A., et al., *Revealing the Concealed Nature of Long-QT Type 3 Syndrome.* Circ Arrhythm Electrophysiol, 2017. **10**(2): p. e004400.
38. George, S.A., et al., *TNFalpha Modulates Cardiac Conduction by Altering Electrical Coupling between Myocytes.* Front Physiol, 2017. **8**: p. 334.
39. Rohr, S., et al., *Paradoxical improvement of impulse conduction in cardiac tissue by partial cellular uncoupling.* Science, 1997. **275**(5301): p. 841-4.
40. Fast, V.G. and A.G. Kleber, *Role of wavefront curvature in propagation of cardiac impulse.* Cardiovasc Res, 1997. **33**(2): p. 258-71.
41. Xie, Y., et al., *So little source, so much sink: requirements for afterdepolarizations to propagate in tissue.* Biophys J, 2010. **99**(5): p. 1408-15.
42. Ciaccio, E.J., et al., *Source-Sink Mismatch Causing Functional Conduction Block in Re-Entrant Ventricular Tachycardia.* JACC Clin Electrophysiol, 2018. **4**(1): p. 1-16.
43. Smyth, J.W. and R.M. Shaw, *The gap junction life cycle.* Heart Rhythm, 2012. **9**(1): p. 151-3.
44. Solan, J.L. and P.D. Lampe, *Connexin43 phosphorylation: structural changes and biological effects.* Biochem J, 2009. **419**(2): p. 261-72.
45. Raisch, T.B., et al., *Intercalated Disc Extracellular Nanodomain Expansion in Patients with Atrial Fibrillation.* Frontiers in Physiology, 2018.
46. Fogh-Andersen, N., P.J. Bjerrum, and O. Siggaard-Andersen, *Ionic binding, net charge, and Donnan effect of human serum albumin as a function of pH.* Clin Chem, 1993. **39**(1): p. 48-52.

47. Bernabeu, P. and A. Caprani, *Influence of surface charge on adsorption of fibrinogen and/or albumin on a rotating disc electrode of platinum and carbon.* Biomaterials, 1990. **11**(4): p. 258-64.
48. Chien, S.C., et al., *Critical appraisal of the role of serum albumin in cardiovascular disease.* Biomark Res, 2017. **5**: p. 31.
49. Quinlan, G.J., G.S. Martin, and T.W. Evans, *Albumin: biochemical properties and therapeutic potential.* Hepatology, 2005. **41**(6): p. 1211-9.
50. Muizelaar, J.P., H.A. Lutz, 3rd, and D.P. Becker, *Effect of mannitol on ICP and CBF and correlation with pressure autoregulation in severely head-injured patients.* J Neurosurg, 1984. **61**(4): p. 700-6.
51. Knapp, J.M., *Hyperosmolar therapy in the treatment of severe head injury in children: mannitol and hypertonic saline.* AACN Clin Issues, 2005. **16**(2): p. 199-211.
52. Cosolo, W.C., et al., *Blood-brain barrier disruption using mannitol: time course and electron microscopy studies.* Am J Physiol, 1989. **256**(2 Pt 2): p. R443-7.
53. Rangel-Castilla, L., S. Gopinath, and C.S. Robertson, *Management of intracranial hypertension.* Neurol Clin, 2008. **26**(2): p. 521-41, x.
54. Willerson, J.T., J.T. Watson, and M.R. Platt, *Effect of hypertonic mannitol and intraaortic counterpulsation on regional myocardial blood flow and ventricular performance in dogs during myocardial ischemia.* Am J Cardiol, 1976. **37**(4): p. 514-9.
55. Larsen, M., et al., *Mannitol in cardioplegia as an oxygen free radical scavenger measured by malondialdehyde.* Perfusion, 2002. **17**(1): p. 51-5.
56. Ouriel, K., et al., *Preservation of myocardial function with mannitol reperfusate.* Circulation, 1985. **72**(3 Pt 2): p. II254-8.
57. Lamke, L.O. and S.O. Liljedahl, *Plasma volume changes after infusion of various plasma expanders.* Resuscitation, 1976. **5**(2): p. 93-102.
58. Moon, P.F., et al., *Effects of a highly concentrated hypertonic saline-dextran volume expander on cardiopulmonary function in anesthetized normovolemic horses.* Am J Vet Res, 1991. **52**(10): p. 1611-8.
59. Roberts, J.S. and S.L. Bratton, *Colloid volume expanders. Problems, pitfalls and possibilities.* Drugs, 1998. **55**(5): p. 621-30.
60. Gombocz, K., et al., *Influence of dextran-70 on systemic inflammatory response and myocardial ischaemia-reperfusion following cardiac operations.* Crit Care, 2007. **11**(4): p. R87.
61. Zhang, B. and J.B. Wieslander, *Dextran's antithrombotic properties in small arteries are not altered by low-molecular-weight heparin or the fibrinolytic inhibitor tranexamic acid: an experimental study.* Microsurgery, 1993. **14**(4): p. 289-95.
62. Togashi, D.M., Ryder, A.G., Mahon, D.M., Dunne, P., McManus, J., *Fluorescence study of Bovine Serum Albumin and Ti and Sn Oxide Nanoparticles Interactions.* Biomedical Optics, 2007. **6628**.
63. Gautam, A., *Solid state fluorescence of proteins in high throughput mode and its applications.* F1000 Research, 2013. **2**.

FIGURES

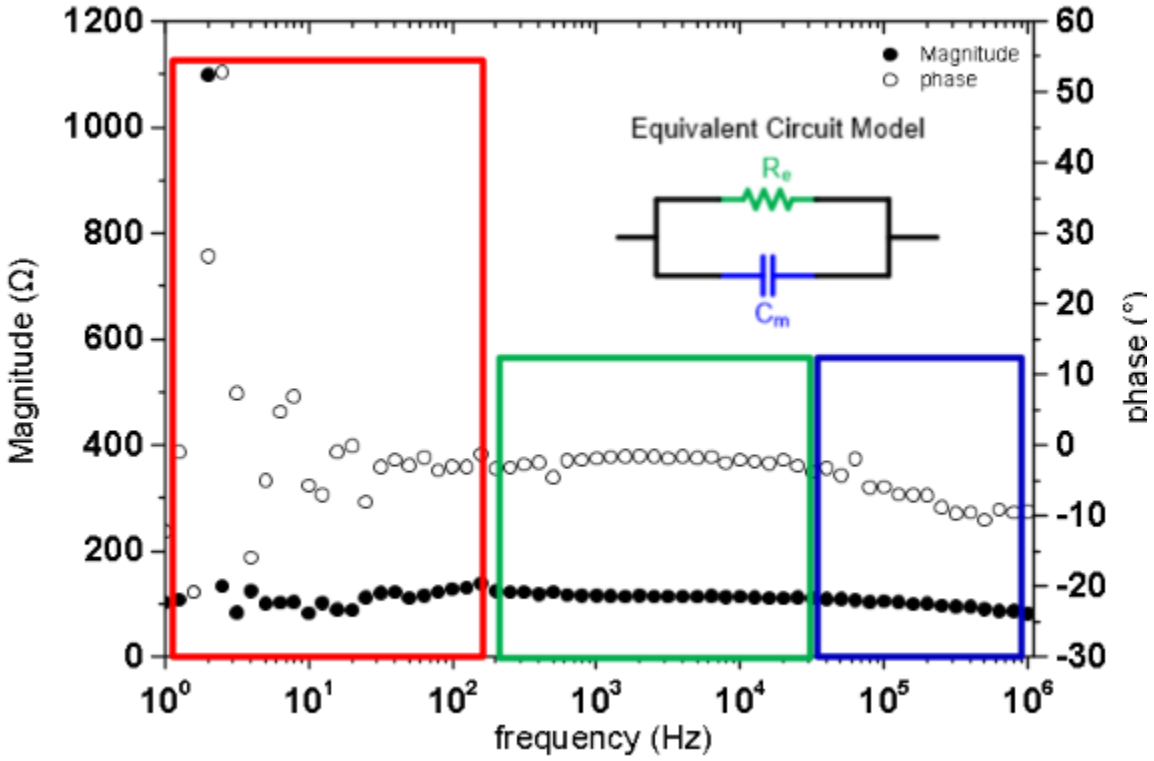

Figure 4.1 Modeling interstitial resistance from electrochemical impedance spectroscopy. We performed a series of impedance measurements and modeled the data as a resistor (green box) and capacitor (blue box) in parallel, corresponding to extracellular resistance and membrane capacitance, respectively. The low frequency noise observed (red box) was likely due to the fluid around the heart during the recording, as demonstrated by dried tissue (Supplemental Data).

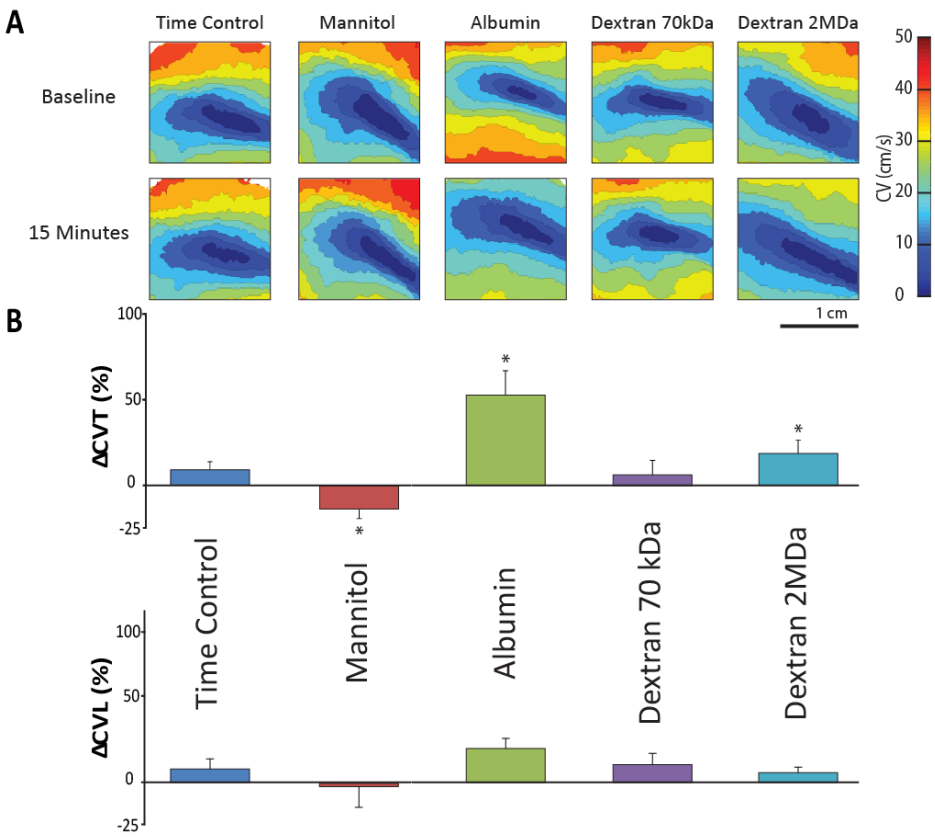

Figure 4.2 Osmotic agents modulate transverse conduction velocity. 3ms optical mapping isochrones (A) show conduction effects with various osmotic agents. Mannitol slows CV while Albumin and Dextran 2MDa increase CV. Dextran 70kDa does not significantly change CV relative to time control. Quantification of CV (B) confirms preferential changes in the transverse direction. (n=10 for Time Control, n= 8 all other conditions, unpaired Student's t-test *p<0.0125 relative to Time Control)

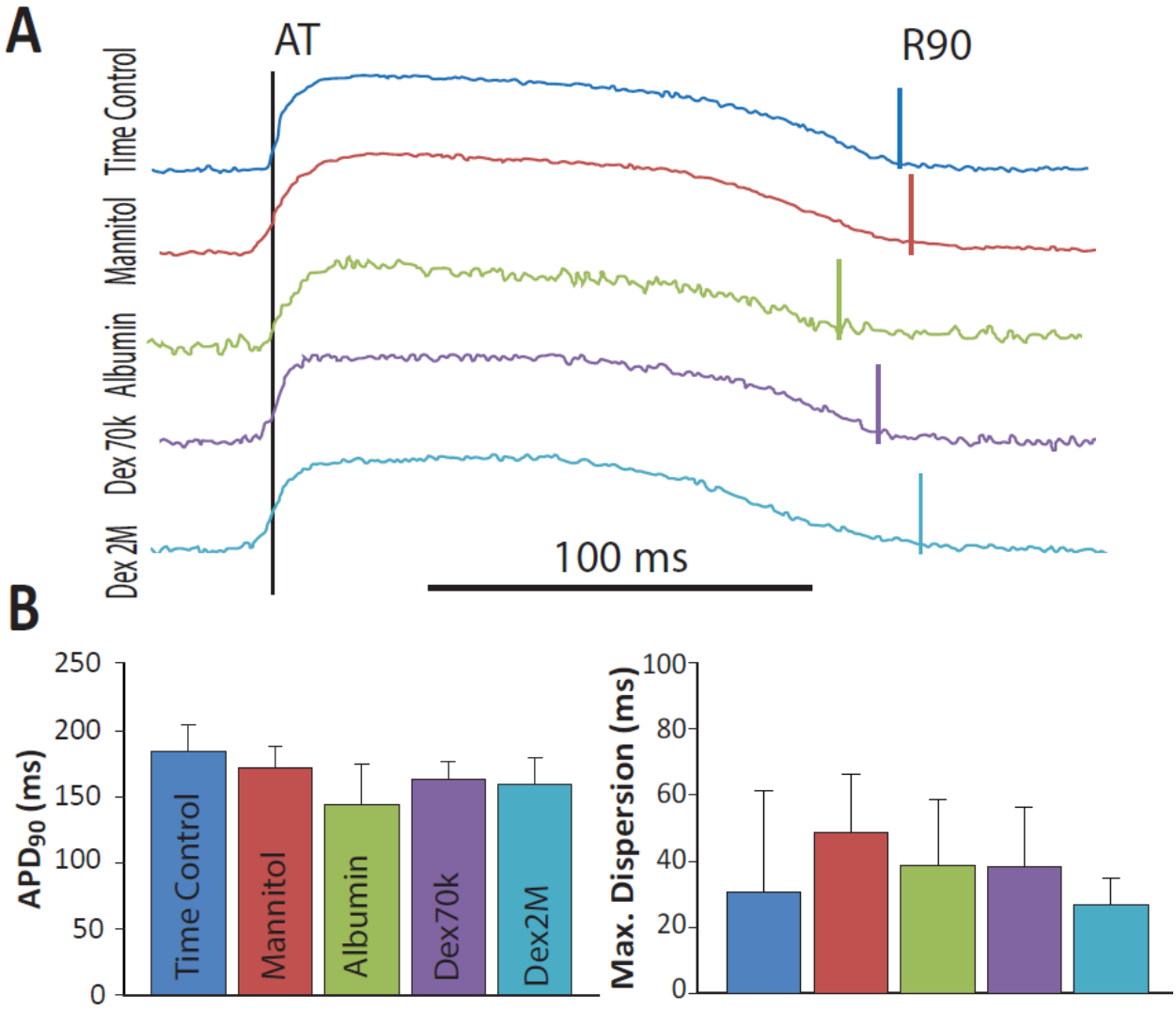

Figure 4.3 Osmotic agents do not change APD. Representative action potentials (A) show no changes to APD90, quantified below (B, left). Furthermore, maximum dispersion (B, right), the maximum APD difference between quadrants of the imaging field, are not significantly different between conditions. (n=6 for Mannitol and Albumin, n=8 for Time Control, Dextran 70kDa and Dextran 2MDa, unpaired Student's t-test p = n.s. relative to Time Control)

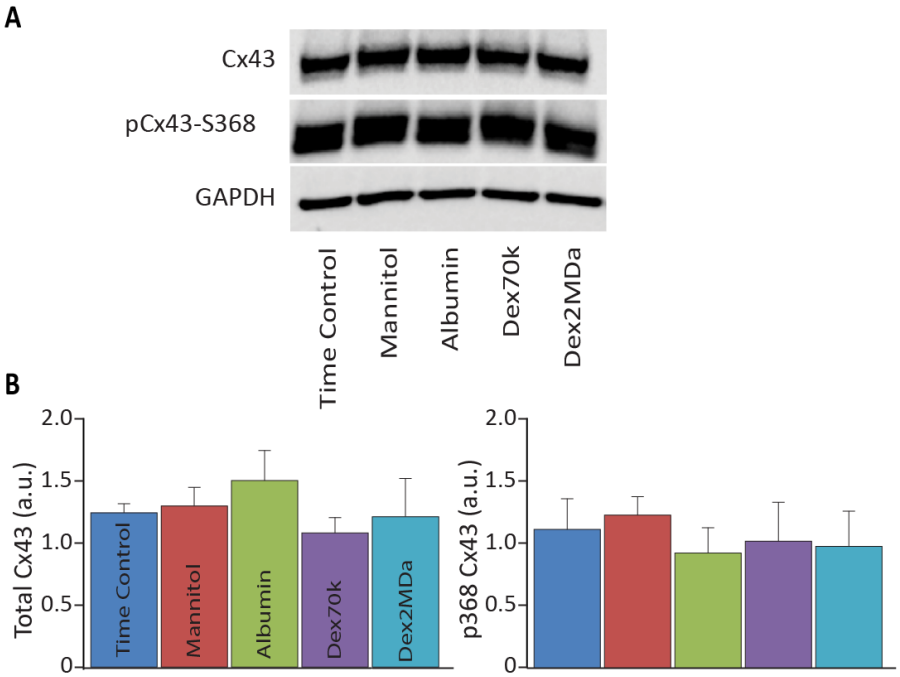

Figure 4.4 Osmotic agents do not significantly alter Cx43 expression or phosphorylation at Serine 368. Western Blot analysis shows no significant changes in Cx43 expression or phosphorylation. These results suggest that conduction changes associated with osmotic agents are not primarily driven by connexin changes. (n=3 per condition, 3 replicates per heart, Student's t-test p=n.s. relative to Time Control)

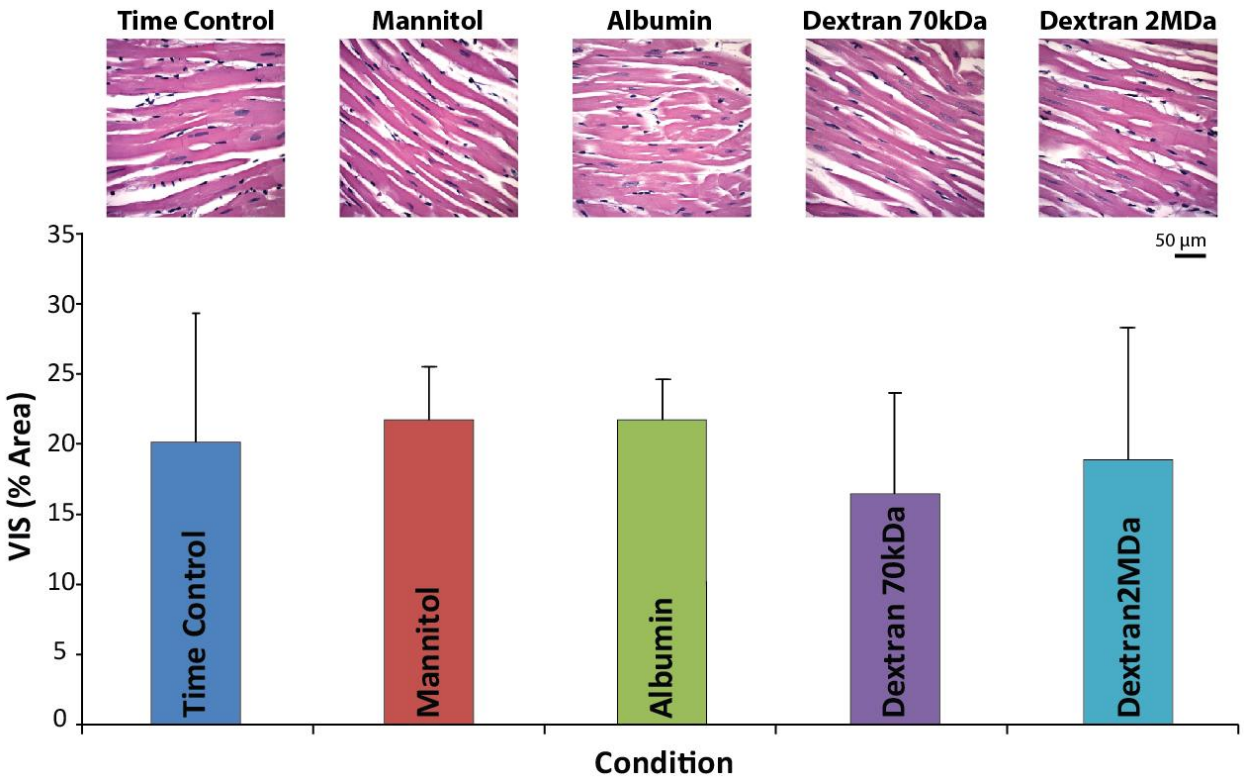

Figure 4.5 Analysis of H&E-stained ventricular tissue reveals no significant differences in interstitial space. The structure of bulk interstitium does not explain observed conduction changes via a cable-like mechanism (n=3 hearts per condition, 10 images per heart, unpaired Student's t-test p=n.s. relative to Time Control).

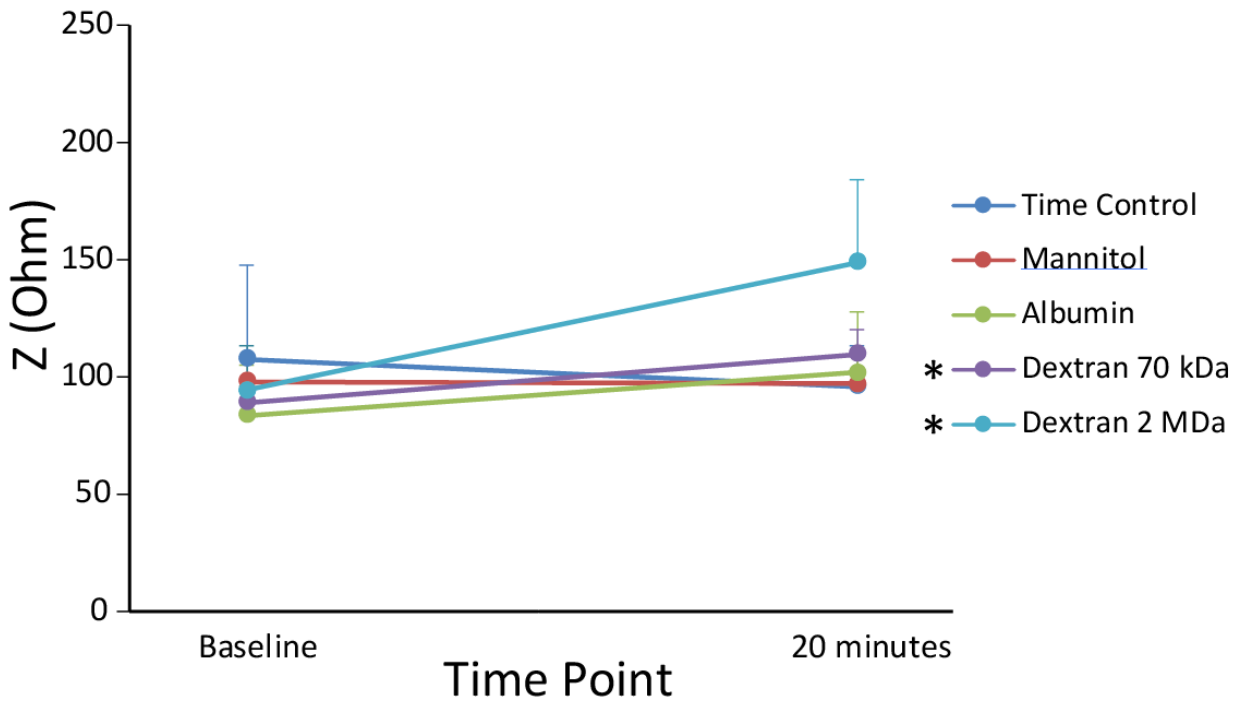

Figure 4.6 Interstitial resistance modulation cannot explain conduction changes. Paired baseline and intervention recordings show no significant change with time control, mannitol or Albumin, but significant increases in interstitial resistance for both Dextran 70kDa and Dextran 2MDa (paired Student's t-test, *$p<0.05$ relative to Baseline).

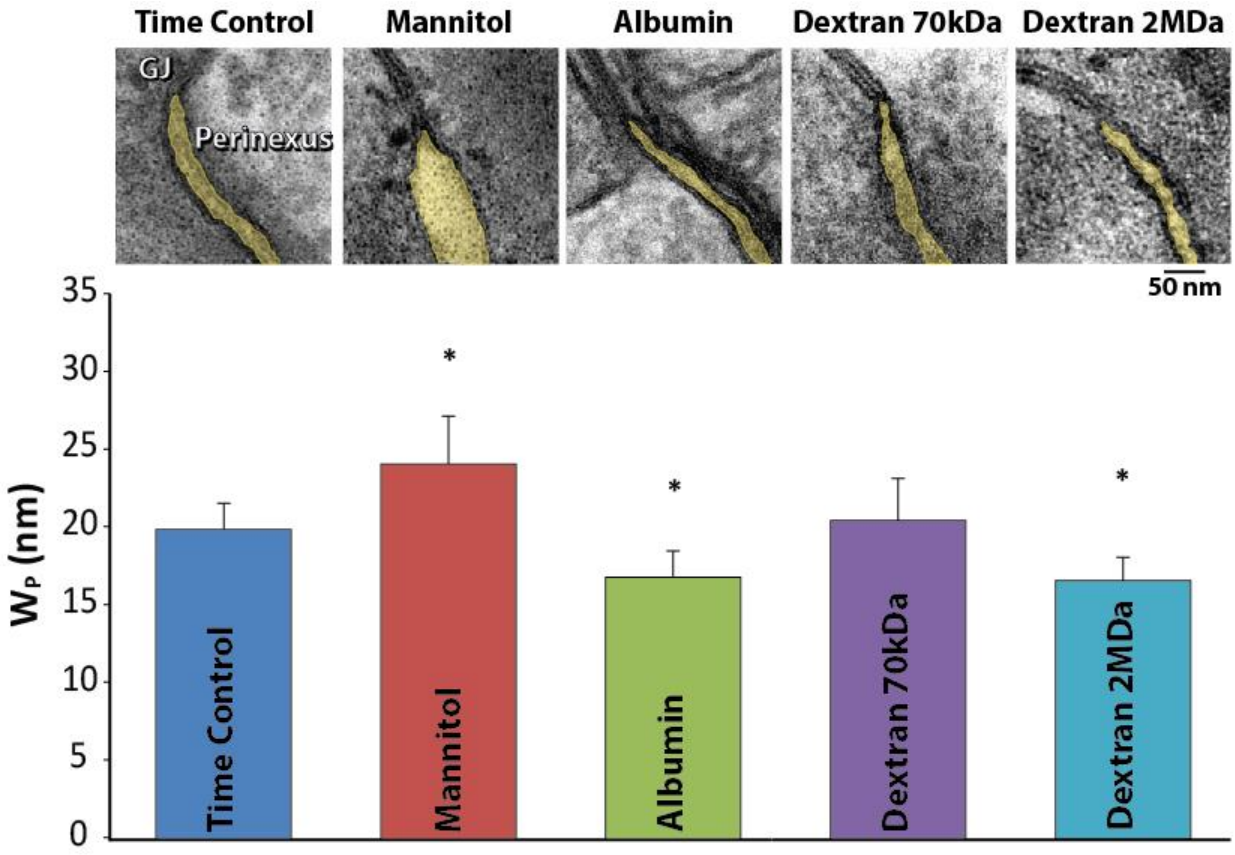

Figure 4.7 The cardiac perinexus inversely correlates with CV. Analysis of TEM imaged perinexi (shaded yellow) from ventricular myocardium demonstrates that modulating this cardiac nanodomain inversely correlates with conduction. Data consistent with a primarily ephaptic mechanism of conduction. (Student's t-test correcting for multiple comparisons, n=3 hearts per condition, 15 images per heart. *, $p<0.0125$)

APPENDIX: SUPPLEMENTAL DATA

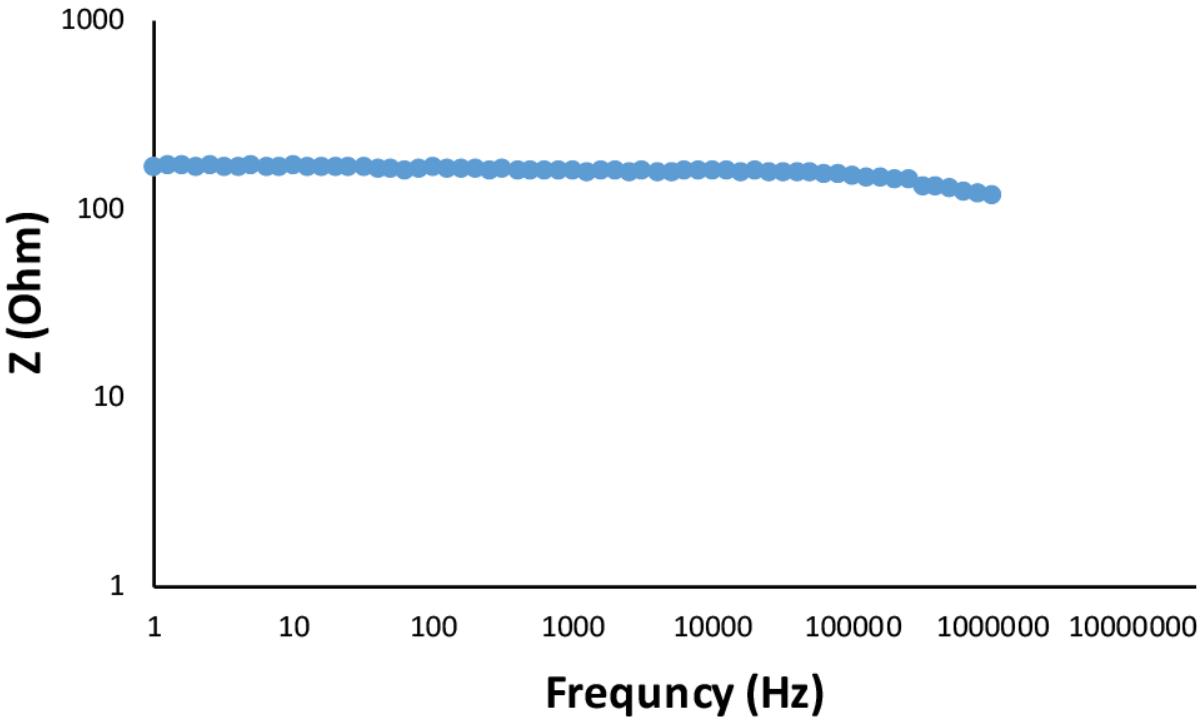

Figure 4.S.1 Low-frequency noise is absent from dried tissue. By performing a similar impedance spectroscopy protocol as described above on isolated right ventricular tissue that had been gently blotted dry, we notice an absence of low-frequency noise. This result leads us to conclude that the fluid on and around the measurement site of our previous impedance experiments is likely responsible for the low-frequency noise observed in those data.

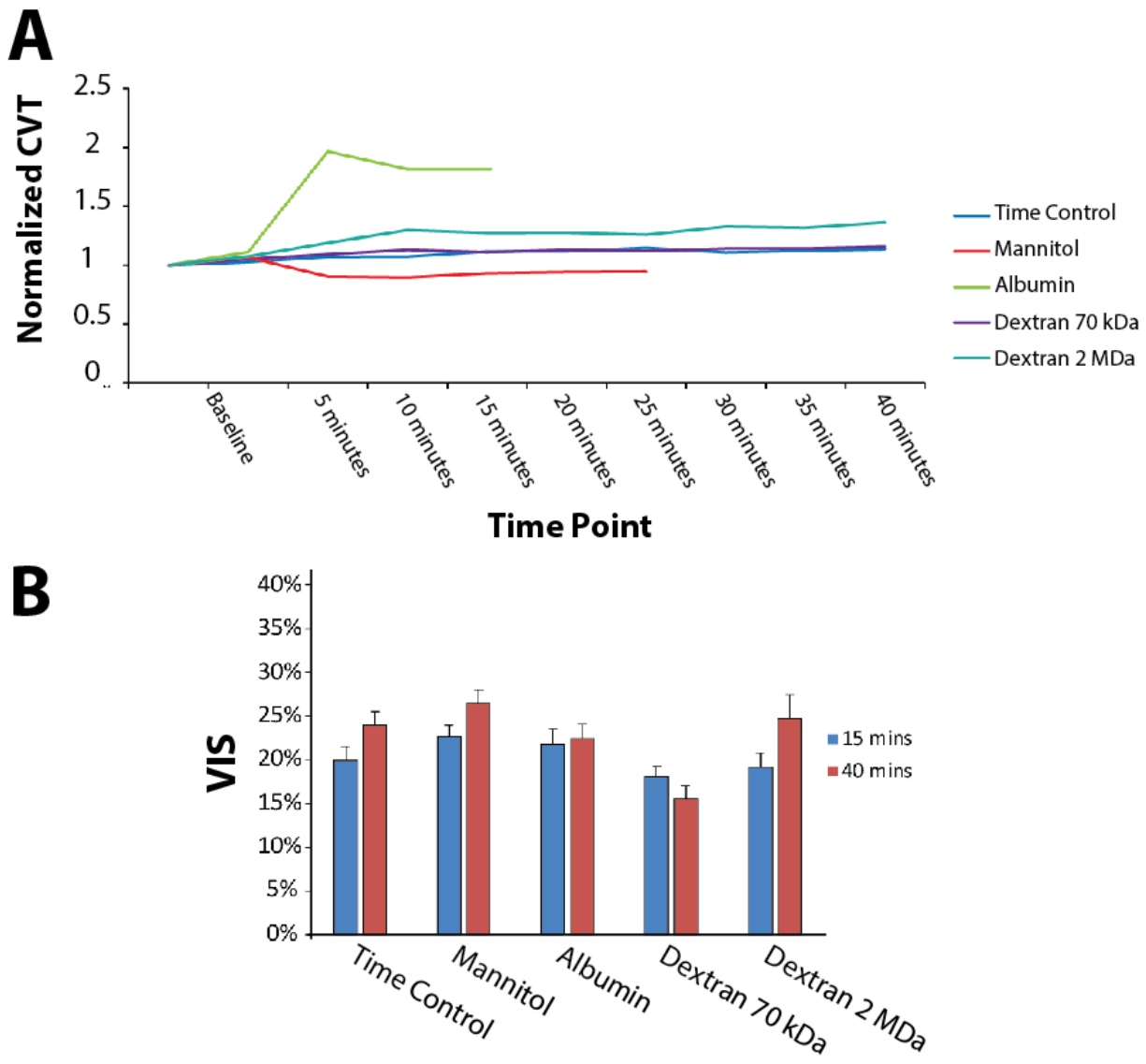

Figure 4.S.2 Extended time course of CV and VIS. Consistent with previous reports, CV reaches a steady-state within approximately 15 minutes (A) of osmotic agent perfusion. Data presented as mean (n=3 per condition) at each time point, no error bars displayed for clarity. With a longer time course, VIS data (B) for mannitol, albumin and dextran 70 kDa also more closely approaches previously-reported data. Data reported as mean ± SE, n = n.s. relative to Time Control.

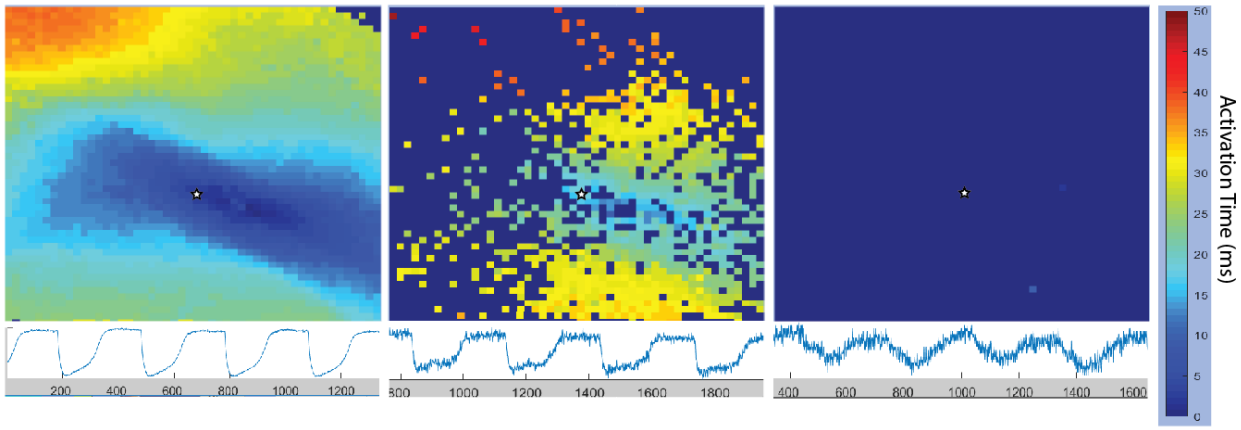

Figure 4.S.3 Albumin degrades optical signals. Optical maps (top) and single-channel recordings (bottom) from hearts at baseline (left) and after 15 minutes (middle) and 40 minutes (right) of albumin perfusion. White stars indicate the channel displayed.

CHAPTER 5: SUMMARY AND FUTURE DIRECTIONS

Summary

Throughout decades of research, scientists have largely been able to model and explain conduction behaviors in cardiac tissue, though clinical application of those concepts has been underwhelming, leaving the developed world with a high prevalence of chronic cardiac diseases and sudden cardiac death. It is therefore of critical importance that we explore additional targetable mechanisms of conduction disruptions. In this thesis, I have provided evidence that the cardiac perinexus could be such a therapeutic target.

Atrial Fibrillation and the Cardiac Perinexus

A primary goal of this dissertation was to identify the cardiac perinexus in human cardiac tissue, as it had previously been observed only in rodents, and determine whether its structure could have implications for human disease. The study in Chapter 2 aimed at achieving those goals through a study of 39 patients enrolled in elective open-heart surgery. We found that not only is the perinexus present in human atrial tissue, but it appears to be similarly rich in sodium channels as was previously determined in rodents and its width had a direct relationship with the incidence of pre-operative chronic atrial fibrillation. In other words, patients with chronic pre-operative atrial fibrillation had wider perinexi than those who did not. Perinexal width could not predict post-operative atrial fibrillation, which remains a major concern in the field of cardiac surgery, but since our samples were taken at the beginning of the procedure, we could not ascertain direct effects of the surgery itself on the perinexus. Still, we were able to identify a potential factor in the onset or continuation of atrial fibrillation, a condition for which it has been notoriously difficult to identify clear triggers or mechanisms. In the course of this study, we also identified the need for an advancement in our perinexus quantification methodology. The manuscript describing the study, with authors spanning the translational spectrum, was accepted into Frontiers in Physiology and published in May of 2018.

Using Serial Image Dilations to Quantify Perinexal Width

In processing the large data sets in the study described in Chapter 2, it became clear that our current manual segmentation process, while scientifically valid, was slow and prone to under-sampling. I therefore developed a Matlab program to use serial image dilations to count the number of pixels between opposing edges, thereby presenting a high-spatial-resolution measurement, specifically at the resolution of the imaging modality itself, of any 2-dimmensional inter-edge distance. This measurement could also be accomplished roughly 5-10 times faster than our manual process, which would be critical for analyzing the large datasets in Chapter 4. To ensure the program would stand up to future scientific rigor, I submitted the manuscript of the study included in Chapter 3 to the Journal of Visualized Experiments. Through the peer-review process, I was able to further refine the program and improve its versatility, specifically with regards to measurement of structures at varying angles, and the manuscript was accepted and published with a video interview in September of 2018. The final goal of this dissertation was to apply my biological knowledge from the clinical study and my new analysis method to resolve a major controversy in the field.

Osmotic Regulation of the Cardiac Perinexus Inversely Correlates with Conduction

While expanding the perinexus has been demonstrated in both rodents and humans to be associated with either slowed or disrupted cardiac conduction, experimental evidence was still lacking that narrowing the perinexus could improve conduction as has been predicted by mathematical models. Furthermore, there is a controversy in the field concerning the role of the interstitial space in conduction. In chapter 5, I sought to demonstrate osmotic regulation of the perinexus, that this regulation could explain changes in conduction, and provide a possible resolution to a major controversy. Through the perfusion of osmotic agents: mannitol, albumin, Dextran 70 kDa and Dextran 2MDa in a Langendorff preparation of guinea pig ventricles, I was able to observe changes in conduction quantified by optical mapping. In parallel with my conduction experiments, I collected tissue to describe the possible structural effects of the osmotic agents. First, I examined possible changes to the gap junction protein Connexin 43 both in overall expression and phosphorylation at a serine site known for its effects on connexin conductivity, Serine 368 (S368). Thanks to Western blots performed by Chandra Baker, I observed no discernable changes in either Cx43 expression

or S368 expression. This finding was not particularly surprising due to the short time frame of the protocol and the lack of evidence that any of the osmotic agents substantially affect gap junctions directly. Next, I looked at changes in interstitial volume, similar to what Sai Veeraraghavan and Andre Kléber had described earlier. However, again likely in part due to my shorter protocol, I did not observe any significant differences in interstitial space between osmotic agents. Perplexed, I decided, since these interstitial volume experiments might not be sufficiently sensitive to detect relevant changes, to measure interstitial resistance directly with a series of impedance measurements. These impedance measurements more closely matched data from similar experiments performed by Fleischhauer and Kléber, but still could not explain my observed changes in conduction in a manner consistent with canonical cable theory. Thus, I used my new serial image dilation algorithm to quantify perinexi imaged with a transmission electron microscope. Here, I found my most compelling data: the perinexi of hearts perfused with albumin and Dextran 2MDa, agents which had increased CV relative to time control, had narrower perinexi than their time control counterparts. On the other hand, hearts perfused with mannitol, which had slowed CV, had wider perinexi than those of time control hearts. Dextran 70 kDa, which had shown any effect on CV, also did not significantly affect Wp. Therefore, not only have I demonstrated osmotic regulation of the cardiac perinexus, but shown that this regulation has an inverse relationship with conduction. Based on the data from my Cx43 and interstitial experiments, I can also conclude that this inverse relationship can better explain changes in conduction than can parameters associated with cable theory.

Conclusions

In conclusion, the findings described in this dissertation could have a significant impact in our diagnosis, prevention and treatment of arrhythmogenic diseases. I have provided evidence to support the idea that ephaptic coupling plays a substantial role in the electrical behavior of the heart and could offer a therapeutic target of conduction disease. Such a target, combined with novel nanoscale materials and drug delivery mechanisms, could drastically improve patient outcomes and quality of life.

Future Directions

In order to achieve the goal of a world without arrhythmogenic diseases, substantial work remains to be done. First, one of the main limitations of this work is that it has been completed exclusively with 2D perinexal images. Unfortunately, current limitations on the resolution of 3D imaging modalities precludes study on nanometer-scale structural changes. A 3 dimensional view of the perinexus is critical to fully understanding its role in conduction as a clinical target. Furthermore, while I have demonstrated it is likely possible to regulate the perinexus osmotically, we must develop novel methods for targeting the perinexus in a clinical setting. In contrast to our surgical methods of acquiring tissue, the ideal treatment would be minimally invasive and localized. Next, though our imaging techniques took weeks to prepare, image, and quantify, we must find novel methods for nearly-instantaneous quantification of the perinexus. Finally, if we are able to locate and target the perinexus, the final step is to reliably and exclusively target the perinexal structure in order to narrow the intermembrane space to enhance conduction and thereby improve patient outcomes.

APPENDIX A: COPYRIGHTS AND LICENSES

COPYRIGHTS AND LICENSES